DISSERTATION

# SOFT AND SHAPE MORPHING ROBOTS DRIVEN BY TWISTED-AND-COILED ACTUATORS


Submitted by

Jiefeng Sun

Department of Mechanical Engineering


In partial fulfillment of the requirements

For the Degree of Doctor of Philosophy

Colorado State University

Fort Collins, Colorado

Summer 2022

Doctoral Committee:

Advisor: Jianguo Zhao

Anthony Maciejewski
Xinfeng Gao
Mostafa Yourdkhani

ABSTRACT

SOFT AND SHAPE MORPHING ROBOTS DRIVEN BY TWISTED-AND-COILED ACTUATORS

Soft robots are a new type of robot with deformable bodies and muscle-like actuation, which are fundamentally different from traditional robots with rigid links and motor-based actuators. Owing to their elasticity, soft robots outperform rigid ones in safety, maneuverability, and adaptability. With their advantages, many soft robots have been developed for manipulation and locomotion in recent years. To enable their unique capabilities, soft robots require a key component—the actuator. Many different actuators have been used, including the conventional pneumatic-driven and cable-driven methods, as well as several novel approaches proposed recently such as combustion, dielectric elastomers, chemical reactions, liquid–vapor transition, liquid crystal elastomer, and shape memory alloy.

Besides existing actuation approaches, another promising actuator for soft robots is the twisted-and-coiled actuator (TCA). Compared with existing actuation methods, TCAs exhibit several unique characteristics: like large energy density and being directly actuated by electricity with a small voltage. All of these characteristics will potentially enable small-scale and untethered soft robots that in general are difficult to be accomplished by pneumatic and tendon-driven methods. Further, unlike shape memory alloys, TCAs are intrinsically soft, making it possible to embed them in any shape inside a soft body to generate versatile motion.

To better actuate soft robots with TCAs, we introduce a novel fabrication technique of contraction TCAs that will have uniform initial gaps between neighboring coils. In this case, they can contract larger than 48% without a preload, termed free stroke. We also characterize such a TCA and compare it with self-coiled TCAs. Besides the free stroke property, the TCA can also be directly used as a sensor that provides its displacement information. To better design, optimize,

and control TCAs for various applications, we developed a physics-based model based on TCAs' physical parameters as opposed to system identification methods, since such physics-based models are expected to be a general model for different types of TCAs (self-coiled, free-stroke, conical)

We demonstrate soft robots with programmable motions by placing TCAs in different shapes inside a soft body. Specifically, we embed TCAs in a curved U shape, a helical shape, and straight shapes in parallel to enable three different motions: two-dimensional bending, twisting, and three-dimensional bending. We also combine the three motions to demonstrate a completely soft robotic arm that mimics a human forearm. A model is also developed to simulate the TCA-driven soft robots. The framework can model 1) the complicated routes of multiple TCAs in a soft body and 2) the coupling effect between the soft body and the TCAs during their actuation process. When not actuated, a TCA in the soft body is an antagonistic elastic element that restrains the magnitude of the motion and increases the stiffness of the robot. By stacking several modules together, we simulate the sequential motion of a soft robotics arm with three-dimensional bending, twisting, and grasping motion. The presented modeling and simulation approach will facilitate the design, optimization, and control of soft robots driven by TCAs or other types of artificial muscles.

Finally, we design shape morphing robots that can morph the shape of their bodies to adapt to a different environment. These robots can be built with shape-morphing modules. A shape-morphing module has a variable stiffness element that allows it to switch between soft and rigid states. While it is in a soft state, it can morph to different configurations driven by TCAs. We demonstrate robots built with these modules can morph to different shapes that facilitate grasping and locomotion.

# ACKNOWLEDGEMENTS

Before beginning this dissertation, I would like to thank many people that have made it possible by contributing their support in many different ways.

First, my advisor Dr. Jianguo Zhao has invested an enormous amount of time and energy in me. I would have achieved far less during my PhD study without his brilliant, intellectual guidance and support. Dr. Zhao is one of the most hardworking and highly focused people that I have known. I hope that I can follow his model being an excellent researcher and teacher in my future career.

I would like to thank my dissertation committee, Dr. Anthony Maciejewski, Dr. Xinfeng Gao, and Dr. Mostafa Yourdkhani for patiently reading this work and giving me extremely valuable feedback as well as career advice.

I am grateful to many other people from whom I have learned a lot. I have worked with Dr. Wei Wang (now in the University of Tennessee) when he was a postdoc at CSU, and what I have learned from him greatly helped me in my own research. The intellectual discussion with Dr. John Till through emails greatly helped me in understanding Cosserat rod theory, which is used to model TCAs and TCA-driven robots.

I also thank all previous and current members of the Adaptive Robotics Lab (in no particular order): Dr. Haijie Zhang, Brandon Tighe, Ben Pawlowski, Elisha Lerner, Billy Hsiao, Zhe Chen, Ali Abbas, Ajai Singh, and Tony DeMario. You have been creating a great work environment and being great friends. I would like to thank all of the undergraduates and the graduates I have had the privilege to know and work with, on both those on senior design and other projects, and that include: Sydney Spiegel, Jordan Julian, Jeff Larchar, and Long Chen.

Finally, I am especially thankful to my lovely wife Li Yang, who graciously married me after the first year of my PhD study. Many other members of my family, especially my parents, sister, and parents in law have also been a source of much-needed support and understanding. Lastly, and most importantly, my little daughter Amelia has been the light of my life and keeps encouraging me to be a better father and teacher.

DEDICATION

*To my darling wife Li Yang,*

*my parents, and my lovely daughter Amelia*

*who encouraged me throughout the creation of this dissertation.*

TABLE OF CONTENTS

LIST OF TABLES

LIST OF FIGURES

# Chapter 1

# Introduction

Inspired by biological systems (e.g., octopus), soft robots made from soft materials outperform traditional rigid robots in terms of safety and adaptivity owing to their compliant and deformable bodies [11]. To enable their unique capabilities, soft robots require a key component – the actuator. Many different actuators have been used, including the conventional pneumatic-driven [12] and cable-driven methods [13], as well as several novel approaches proposed recently such as combustion [14], dielectric elastomers [15] with variations [16], chemical reactions [17], liquid-vapor transition [18], liquid crystal elastomer [19], and shape memory alloy [20, 21].

## 1.1 TCAs for Actuating Robots

(a) (b) (c)

**Figure 1.1:** Photos of different TCAs. (a) Helical TCAs made of fishing line [1]. (b) Helical TCA painted with silver [2]. (c) Conical TCA made of fishing lines [3].

Besides existing actuation approaches, another promising actuator for soft robots is the twisted-and-coiled actuator (TCA), which can be conveniently fabricated by continuously twisting polymer fibers into coiled spring-like shape [1] as shown in Fig. 1.1a and b, or a conical shape in Fig. 1.1c.

Compared with existing actuation methods, TCAs exhibit several unique characteristics: 1) they are low-cost since the polymer fibers used to fabricate them can be commonly used household fibers (e.g., sewing threads or fishing line); 2) they have a large work density (27.1 kW/kg) [1], meaning a TCA can deliver a force much larger than its own weight (generally more than 100 times) [22]; 3) they can be directly driven by electricity with a small voltage (a few volts) buy using silvered-painted threads as shown in Fig. 1.1b [2]; 4) they can sense their own deformation through the change of electrical properties (e.g., resistance) [23, 24]. All of these characteristics will potentially enable small-scale and untethered soft robots that in general are difficult to be accomplished by pneumatic and tendon-driven methods [25, 26]. Further, unlike shape memory alloys, TCAs are intrinsically soft, making it possible to embed them in any shape inside a soft body to generate versatile motion.

While rigid robots driven by TCAs can have good performance due to the promising characteristics of TCAs (Fig. 1.2) [4–6], TCA-driven soft robots presented in recent years only can perform rudimentary crawling and bending [7–10] (Fig. 1.3). The main reason is that traditional contraction TCAs' large stroke is generally obtained under a preload (e.g., a hanging weight). Without a preload, those TCAs will have negligible strokes because all the coils almost contact with each other. Such preloads will cause problems when TCAs are used to actuate soft robots since a preload will easily deform the soft body due to the low force bearing capability of soft materials (Young's modulus $10^4$ $10^9$Pa) [11]. For example, if we first preload a TCA by applying a stretching force before embedding it into a soft body, the tension force of the TCA will deform the soft body after removing the force. To address this problem, we can use an antagonistic configuration by using two TCAs in parallel, but it will require a larger force to bend, resulting in a small bending range [6]. Note that TCAs that can extend generally do not need a preload, but they can only deliver much smaller forces compared with contraction ones [27, 28].

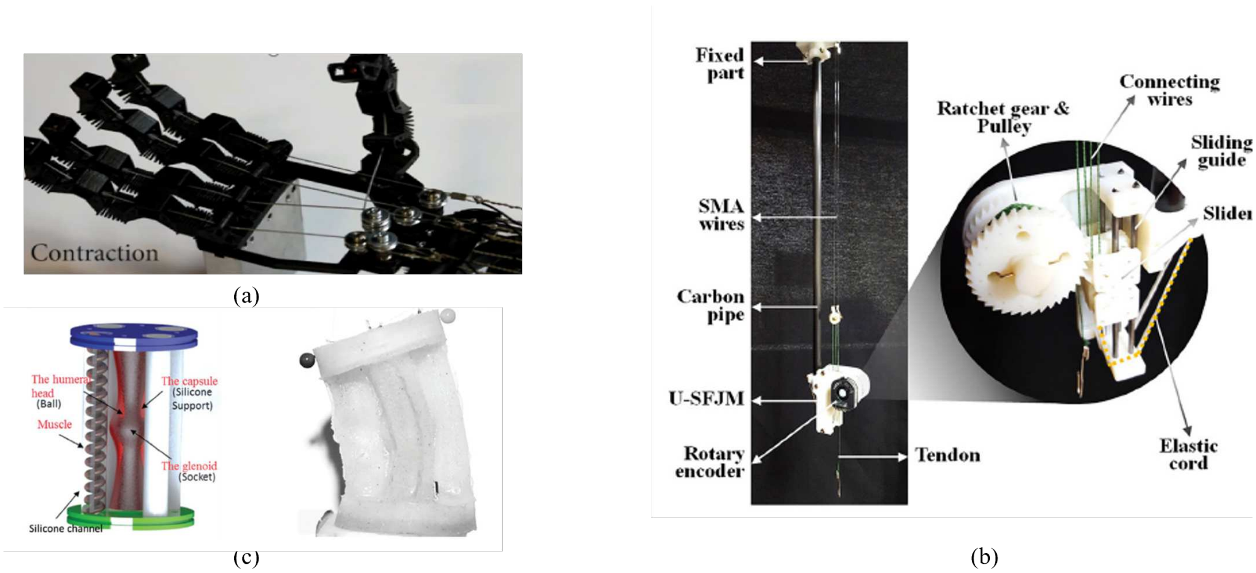


**Figure 1.2:** TCA-driven rigid robots. (a) Robotic hands [4]. (b) A joint mechanism [5]. (c) A musculoskeletal system [6].

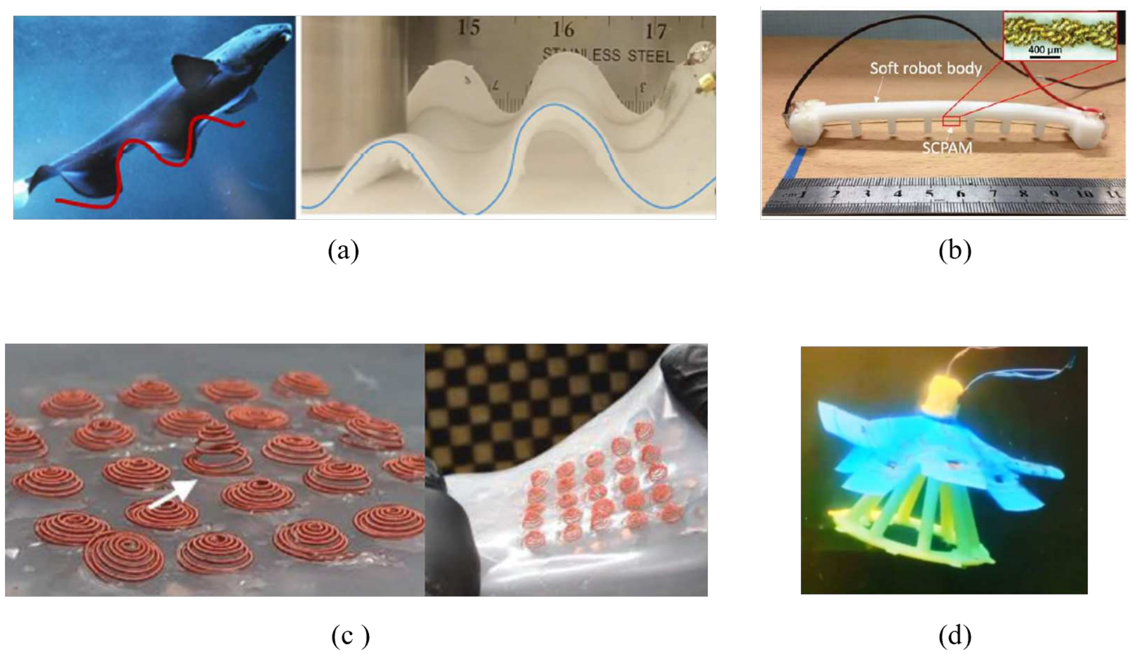


**Figure 1.3:** TCA-driven soft robots. (a) A soft skins [7]. (b) A crawling robot [8]. (c) A morphing skin driven by many conical TCAs [9]. (d) A jellyfish robots [10]. (a), (b), and (d) are driven by self-coiled TCAs made of conductive threads.

**Table 1.1:** The comparisons between existing models for TCAs

| Reference | TCA type | Twisted Fiber | Thermal Model | Fiber Actuation | Coil Kinematics | Coil Statics | Elastic Moduli |
|---|---|---|---|---|---|---|---|
| Yang [29] | Self-coiled | Fishing line | None | Concentric helical laminate CTE d.n. $T$ | CST | CST | Constant |
| Yip [4], Cho [30], Oiwa [31] | Self-coiled | Sewing thread | Convection | None | Characterized, linear with $T$ | Measured constant | None |
| Luong [32] | Self-coiled | Sewing thread, Spandex yarn | Convection, damping | None | Characterized linear with $T$ | Measured constant | None |
| Masuya [33] | Self-coiled | Sewing thread | Convection, radiation, damping | None | Characterized, linear with $T$ | Measured constant | None |
| Abbas [34] | Self-coiled | Sewing thread | Convection | Single Helix, constant CTE | CST | CST | Calculated, d.n. $T$ |
| Lamuta [35] | Self-coiled | Carbon Fiber/PDMS | Convection | Fiber radius increase | CST | CST | Calculated constant |
| Wu [36] | Mandrel-coiled | Sewing thread | None | Convection | Love's Equation | Calculated Constant (Wahl) | Constant |
| Karami [37] | Self-coiled | Sewing thread | Convection, resistance change | Single Helix, CTE d.n. $T$ | Linear | CST | Calculated d.n. $F_e$ and $T$ |
| Kotak [38] | Conical | Fishing line | Convection | Single Helix, CTE d.n. T | Linear | Calculated Constant (Wahl) | Constant |
| **Our work** | Self-coiled, freek-stroke conical | Sewing thread | Convection, monitored power | Single Helix, CTE d.n. $T$ | Cosserat Rod, Love's Equation, CST | Cosserat Rod Love's Equation, CST | Calculated d.n. strain and $T$ |

CTE: Coefficient of Thermal Expansion; d.n.: depending on; CST: Castigoliano's Second Theorem.

## 1.2 Modeling of Twisted-and-Coiled Actuators

To better design, optimize, and control TCAs for various applications, it is critical to establish precise models for TCAs. A list of existing models are presented in Table 1.1. We are particularly interested in physics-based models based on TCAs' physical parameters as opposed to system identification methods [4], since such physics-based models are expected to be more general. Although some of the existing physics-based models can provide enough accuracy for special types of TCAs (e.g., self-coiled ones), a general model for different types of TCAs (self-coiled, free-stroke, conical) is still missing. In the following, we briefly review pioneering works and discuss their limitations.

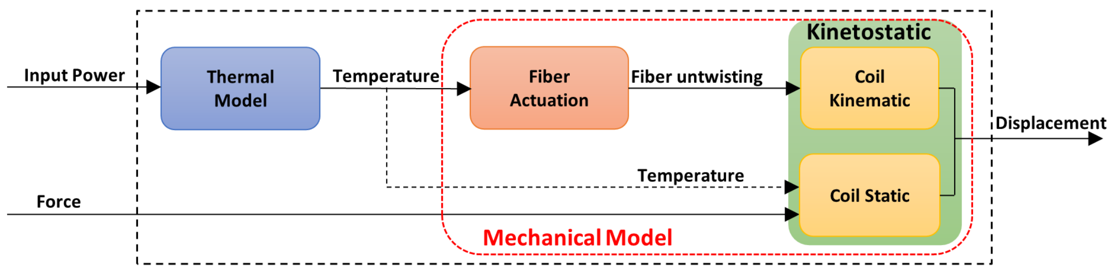


**Figure 1.4:** The schematic for the modeling overview. The input is the input power and the external force, and the output is the TCA's displacement. The whole TCA model is boxed with black dashed lines, and the mechanical model is boxed by red dashed lines. The mechanical model can be a TCA statics or TCA dynamics.

As shown in Fig. 1.4, the existing modeling of TCAs can be divided into two sequential models: a thermal model and a mechanical model. The thermal model first solves a TCA's temperature given the input power, and then the mechanical model takes the temperature and external forces to solve the state of the TCA (displacement, velocity, and acceleration, etc.).

For the thermal model, the most common ones treat a TCA as a single body with a uniform temperature. This model considers the natural convection in the air as only energy dissipation, and the heat source is Joule heating from electricity [4,30–32,34,35]. Besides the common ones, some models consider a more complicated process. Masuya et al. [39] included the radiation and the heat generated from damping to the model. Karami et al. [37, 40] assumed the resistance of TCAs made of conductive sewing thread changed with respect to temperature linearly.

For the mechanical model, we divide it into three sub-models according to the working principle of TCAs (Fig. 1.4). As the temperature increases, the twisted fiber in a TCA will untwist. A *fiber actuation model* predicts the amount of untwisting with the temperature as an input. With the untwisting, a *coil kinematic model* converts the untwisting to a linear displacement along the TCA. Since a TCA has a spring-like helical shape, we need a *coil static model* to predict a TCA's passive deformation under an external load. The coil kinematic and static model, often coupled, together are called a *coil kinetostatic* model.

For the fiber actuation model, there exist extensive works on modeling the untwisting of *monofilament* fibers, such as fishing lines using a single helix model by assuming all the polymer chains in the fiber behave the same like a single helix [41]. However, the actuation of *multifilament* fibers (sewing threads) is underexplored due to the complicated twisting structure inside them. For instance, a conductive sewing thread (e.g., 235/34 4ply, Shieldex Trading) consists of 4 plies of individual yarns twisted together in a 'z' twist (right-hand twist), and each yarn is made by twisting many thin fibers together in 's' twist (left-hand twist).

For the coil kinematic model, there exist three methods. The first method is based on system-identification [4, 30–33]. But instead of measuring how much a TCA contracts after increasing temperature, the contraction force is usually measured. The other two methods are physics-based: Castigliano's Second Theorem (CST) [29, 34] and Love's equation [2, 3, 36, 42]. CST, based on the infinitesimal strain theory, is usually used to calculate the deformation of a structure under an external load. By considering the untwisting torque of a twisted fiber as an external load, CST can relate the untwisting to a TCA's linear displacement. Love's equation is a pure kinematic relationship that relates the untwisting of a twisted fiber to a TCA's pitch angle and thus its displacement. Note that Knot Theory results in the same kinematic relationship as Love's equation as discussed in [3].

For the coil static model, a TCA's passive deformation can be determined from its stiffness if we treat the TCA as a mechanical spring. Researchers have used: 1) a constant stiffness obtained from experiments [4, 30–32, 43]; 2) a constant stiffness calculated using the classical formula [44] for a helical spring as in [36]; 3) stiffness that varies with deformations [29, 34, 37, 40]. Such nonlinear stiffness has been modeled using CST, but no work uses Love's equation.

Although various models have been proposed recently, they are limited in two aspects. First, they are not general enough for different types of TCAs shown in Fig. 1.1 and 3.1. In fact, most of the existing models are only developed for a specific type of TCAs, and there is no existing model that is verified to be able to model different types of TCAs. Second, existing models are not accurate enough due to modeling simplifications. For example, the CST method is based on the infinitesimal strain (small deformation) theory, and Love's method ignores the shear and extension strain for the twisted fiber, making them inaccurate when TCAs undergo large deformations.

## 1.3 Modeling of Soft Robots

The overall goal of modeling and simulating soft robots has been to develop an approach that is both accurate enough for predictions and efficient enough for design and control. Several modeling and simulation approaches have been investigated recently, most of which can be classified into two groups: 1) top-down approaches using discretized segments to approximate the continuous shape of soft robots; 2) bottom-up methods using commercially available software to accurately simulate the deformation. For top-down approaches, the body is assumed to be made of either a single section or multiple sections that have a constant shape, typically a circular arc (constant curvature) [45–51]. These simplify the models of soft robots nicely to generate formulations similar to traditional robots. However, they are generally less accurate under certain conditions like large external loads, out-of-plane deformation, and dynamic motion. For bottom-up approaches, finite element software (e.g., ABAQUS) is directly used to simulate the dynamics with calibrated material properties through experiments [52, 53]. The bottom-up approaches are quite generic, but they are very time-consuming for each simulation, preventing them from being useful for real-time control. Note that there has been recent work on optimizing FEA based approaches using Model order reduction [54, 55], which trades accuracy for more computationally efficient simulations.

Besides these two approaches, another approach based on continuum mechanics has been recently investigated, which is both accurate and computationally tractable. Such an approach represents the mechanics more accurately compared with approaches like constant curvature by modeling various deformations (e.g., bending, torsion, shear, and extension) relevant to soft robots. Typically, the approach takes on the form of rod models like Euler-Bernoulli beams [56,57], Kirchhoff rods [58], and Cosserat rods [59, 60]. Cosserat rod theory can accurately model slender rods, including twisted fibers, by considering four strains (torsion, bending, shear, and extension). As a topic in solid mechanics, it has been recently adapted to the robotics community to accurately model tendon-driven and fluid-driven compliant/soft robots [61, 62]. Besides more accurate, it can also be numerically implemented to achieve real-time simulation. Recently, it is shown that Cosserat rod models can achieve real-time dynamics simulation by using implicit numerical integration schemes together with C++ implementation [63]. Therefore, it is promising to leverage such an approach for both accurate analytical modeling and real-time simulation of soft robots.

## 1.4 Outline and Contribution of this Dissertation

**Ch2: TCAs with Free Strokes**

To better actuate soft robots with TCAs, we introduce a novel fabrication technique of contraction TCAs that will have uniform initial gaps between neighboring coils. In this case, they can contract over 48% without a preload, termed as free stroke. Such free strokes can enable soft robots by directly embedding one or multiple TCAs into a soft body without preloading those TCAs (Fig. 4.1a). With a large free stroke, TCAs can actuate the soft body to achieve a large magnitude of motion. They can also be arranged in different shapes inside a soft body to achieve programmable motions. The contribution of this part is to propose an upgraded fabrication method to generate TCAs with free strokes. Such TCAs can be applied to a wide variety of applications that requires artificial muscles, including robotics, haptics, intelligent structures, smart textiles, etc. [64].

### Ch3: Modeling of TCAs

We present a general physics-based modeling approach to model a TCA's statics and dynamics based on the Cosserat rod theory. Our proposed model based on Cosserat rod theory is both more accurate and more general compared with existing models. It is more accurate because 1) it is geometrically exact: no approximation of small deflection is assumed; 2) it considers all four strains; 3) it can include nonlinearity of material such as temperature and strain dependency. It is also more general because it can model different types of TCAs with different shapes that cannot be modeled using existing models. In fact, we show that existing models using Love's equation and CST are simplified cases of our model. Because of the better generality and accuracy, we expect our model can be widely used for the design and optimization of TCA-actuated devices/systems/robots.

### Ch4: TCA-driven Soft Robots

We demonstrate soft robots with programmable motions by placing TCAs in different shapes inside a soft body. Specifically, we embed TCAs in a curved U shape, a helical shape, and straight shapes in parallel to enable three different motions: two-dimensional bending, twisting, and three-dimensional bending, respectively. We also combine the three motions to demonstrate a completely soft robotic arm that mimics a human forearm. Such demonstrations lay a foundation for achieving more complicated motion or shape morphing by strategically embedding multiple TCAs inside a soft body, similar to recent results using other actuation methods (e.g., pneumatic-driven [65] and liquid crystal elastomers [66, 67]). We envision that this work will inspire a variety of TCA-driven soft/rigid robots or structures to achieve versatile motions or morphologies, especially those in centimeter scales.

### Ch5: Modeling of TCA-driven Robots

We establish a more general modeling framework using Cosserat rod theory. The model will consider the actuation and coupling between multiple TCAs, allow us to simulate complex motion generated from the irregular routes of the TCAs, and realize the combination of motions. Our method is different from some recent research on simulation of shape memory alloy (SMA) driven robot [68] and musculoskeletal systems [69]. Both of them generate actuation by shifting reference states of a rod or directly applying general force and moment on a part of the rod; therefore usually there is no implicit coupling between a robot and the artificial muscle. Unlike these works, our method considers the coupling between an artificial muscle and the soft body, and the implicit artificial muscles' forces needed to be solved during the process. Since these phenomena exist for soft robots driven by other artificial muscles (e.g., dielectric elastomers, liquid crystal elastomers), we expect our method can also be used for modeling and simulating those robots.

**Ch6: Shape-morphing Robots**

A common limitation of current solutions is the inability to withstand large force and needs to keep consuming energy. That is because these robots often need to leverage a soft body or use compliant design to easily change the morphology. A second limitation is that many shape-shifting mechanisms are driven by rigid external components, for example, shape-shifting based on pneumatic or thermal expansion will cause unwanted volume change, and based on magnetic will require an external manipulating station. A third limitation is their inability to reprogram the target geometry. Although there are designs that address one or two of these limitations, soft robots that can simultaneously satisfy all three are rare. We introduce a shape-morphing design approach based on shape-morphing modules that allow for reconfiguration of soft or rigid robots into different body shapes for different functionalities. Shape-morphing modules are modular rods or sheets with variable stiffness and embedded actuation, which may be applied to, removed from, and transferred between different robots to realize reconfigurable shapes for various tasks. The modules are driven by embedded artificial muscles: twisted-and-coiled actuators (TCAs) that do not rely on external or internal rigid components (pump, motor, and magnet coils). We characterized the module and implement the module into an adaptive gripper and a tetrapod robot.

# Chapter 2

# TCA with Free Stokes: Fabrication, Characterization, and Self-sensing

Various actuators (e.g., pneumatics, cables, dielectric elastomers, etc.) have been utilized to actuate soft robots. Besides widely used actuators, a relatively new artificial muscle — twisted-and-coiled actuators (TCAs) — is promising for actuating centimeter-scale soft robots because they are low-cost, have a large work density, and can be driven by electricity. However, existing works on TCA-actuated soft robots in general can only generate simple bending motion. The reason is that TCAs fabricated with conventional methods have to be preloaded to generate a large contraction, and thus cannot actuate soft robots properly. In this chapter, an upgraded technique is presented to fabricate TCAs that can deliver 48% free strokes (contraction without preloading) and 55% stroke with a weight. We compare the static performance of TCAs with free strokes to conventional TCAs, and characterize how will the fabrication parameters influence the TCAs' stroke and force capability.

## 2.1 Principle to Fabricate TCAs with Free Strokes

The fabrication process for TCAs with free strokes is built on the original mandrel coiling process [1] with a key difference: we coil a twisted thread on a special mandrel with a helical groove, generating a coiled shape with uniform initial gaps between neighboring coils.

The principle to fabricate a TCA with free strokes are illustrated in Fig. 2.1 and more details can also be found in Fig. 2.2 using our customized machine. First, a conductive sewing thread is twisted to generate a twisted thread with the fiber pitch $\alpha_f$ angle and length $l_0$. Then, the twisted thread is coiled in the same direction as twisting on the special mandrel with a helical groove that has a coil pitch angle $\alpha_m$ (Fig. 2.1b). The groove is formed by uniformly wrapping a copper wire around a mandrel core (a cylindrical rod). With the groove, the twisted thread will be guided into

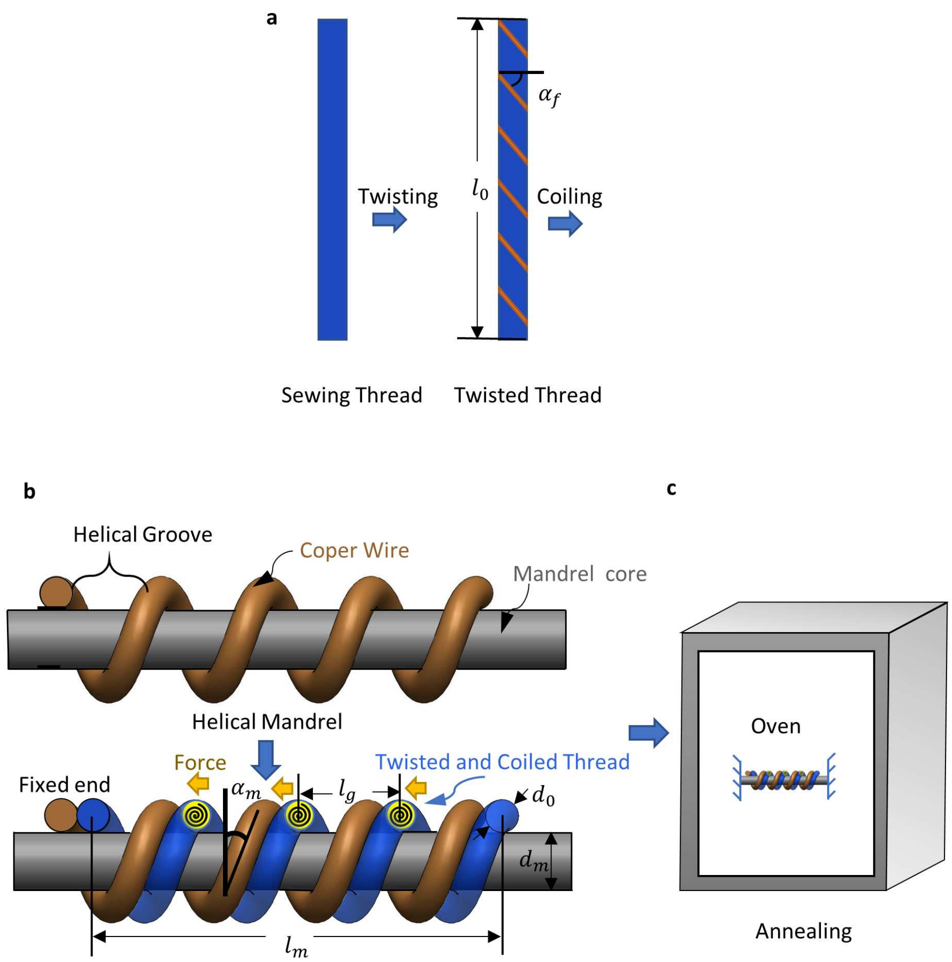


**Figure 2.1:** The schematic showing the fabrication process of TCAs with free strokes. (a) Twist a sewing thread to generate a twisted thread. (b) Coil the twisted thread on a helical mandrel with a cylindrical mandrel core and helical grooves formed by a copper wire to generate coiled and twisted thread. (c) Anneal the coiled and twisted thread in an oven to generate the final Twisted-and-Coiled Actuator (TCA).

a helical shape with gaps between coils. Without the helical groove, the twisted thread will not have gaps because the coils will be pulled together by a pulling force generated by the internal untwisting torque in the thread. After the coiling process, the coiled twisted thread is annealed in an oven with the helical mandrel whose two ends are fixed to set this shape as an equilibrium state (Fig. 2.1c). After annealing, the coiled twisted thread can be removed from the helical mandrel to generate a final TCA. A training process (several slow heating cycles) needs to be applied before the first-time use to remove the TCA's internal stress to get consistent performance.

### 2.1.1 Procedures to Fabricate TCAs with Free Strokes

**The customized Machine for Fabricating TCAs with Free Strokes**

We design a customized machine to fabricate TCAs with free strokes as shown in Fig. 2.2a. The machine has two step motors A and B (coiling motors) facing each other in a horizontal line and a traveler controlled by another step motor C (guiding motor) that can travel between the two motors. The two coiling motors are used to hold a mandrel core (a cylindrical rod or wire) and apply a tension to keep the mandrel taut. The traveler is used to guide a copper wire wrapped on the mandrel core to form a helical groove. The main function of the machine is to fabricate a helical mandrel and coil a twisted fiber on the mandrel in the guiding groove. The machine can fabricate a TCA that has a maximum length of 800 mm in 15 mins except for the annealing and training time.

**Fabrication of the Helical Mandrel**

To fabricate the helical mandrel, we first tie the two ends of a rigid carbon fiber rod to the two coiling motors' shafts (Fig. 2.2a). A copper wire travels with the traveler at a constant speed from one end to the other. When the two motors are rotating in the same direction, the copper wire will be wrapped around the carbon rod in a helical shape to form the guiding groove. After that, we fix the two ends of the copper wire on the carbon rod and a firm groove will be formed on the mandrel. The speed ratio between the guiding motor and the coiling motors can be tuned to fabricate a helical mandrel with different coil bias angles.

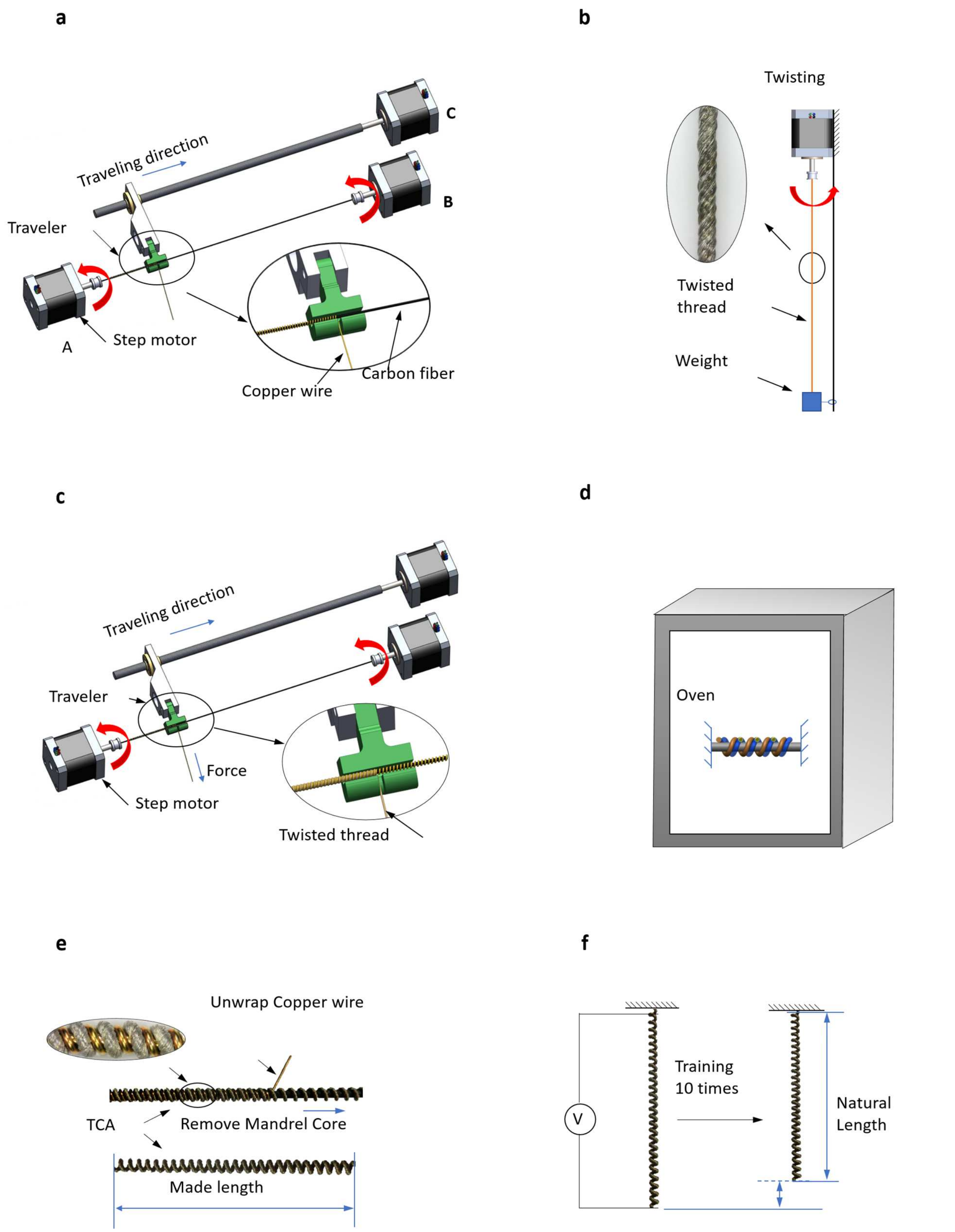


**Figure 2.2:** The fabrication process of TCAs with free strokes. (a) Make the helical mandrel on the machine. (b) Twist a thread. (c) Coil the twisted thread in the groove on the helical mandrel using the machine. (d) Anneal the TCA with the mandrel. (e) Remove the TCA from the mandrel. (f) Train the TCA to get a reversible free stroke.

Then, we fabricate TCAs with free strokes by coiling a twisted fiber on the helical mandrel along the groove. In Fig. 2.2b, We twist 1 thread (Shieldex Trading, 235/36 dtex 4 ply HC+B) with an initial length of 350 mm by hanging a weight of 240 g, and the process ends after inserting N = 287 rotations before auto-coiling starts. A weight heavier than 240 g may easily break the threads and a lighter weight will not allow for enough twisting of the threads. Fig. 2.2c shows that the both motors rotate the helical mandrel to coil the twisted threads on it along the groove in the same direction as twisting. After that, the two ends of the twisted threads are clipped on the mandrel to prevent it from uncoiling. The actuator is then annealed in an oven (Quincy Lab 10GCE, accuracy 0.5°C) for 2.5 hours at a temperature of 180°C or 200°C. Finally, we obtain a stabilized TCA that does not untwist when the copper wire is unwrapped from the carbon fiber rod (Fig. 2.2 d-e).

After the TCA is removed from the mandrel core, a training process in Fig. 2.2f is performed to endow the TCA a reversible stroke. In the process, a weight of 2 g is hanged at the end of the TCA to keep it straight, and we apply electricity to make it fully contracted for 10 times. Finally, the TCA will have a reversible stroke (free stroke) and recover to a certain length even without any external load after cooling. The length of the TCA after training (natural length in main texts) will be shorter than the length when it is with the mandrel (called made length in main texts). We can easily fabricate TCAs with different parameters. For example, we can fabricate TCAs with different inner diameters and coiling angles by changing the diameter of the carbon fiber rod and the traveling speed of the traveler. We totally fabricated 5 types of TCAs using the same twisting fiber and their parameters are summarized in TAB. 2.1.

With the machine, it takes total 8 mins to fabricate the TCA: 3 mins to fabricate one helical mandrel, 3 mins to fabricate a twisting thread and another 2 minutes to coil the twisted threads on the mandrel. To improve efficiency, a long TCA could be fabricated and cut into several pieces for different usages.

**Fabrication Parameters of TCAs used in this Work**

The five TCAs (Type 0, Type 1, and Type 2) have the following same parameters

**Table 2.1:** The fabrication parameter of TCAs

| NO. | $\alpha$m | $\alpha_n$ | $l_m$ | $l_n$ | $S_f$ | $T_a$ |
|---|---|---|---|---|---|---|
| Type 0-180 | 11.53 | 10.8 | 70 | 61 | 5.7% | 180 |
| Type 1-180 | 15.57 | 14.56 | 94 | 88 | 20.4% | 180 |
| Type 2-180 | 22.54 | 18.14 | 133.5 | 109 | 35.7% | 180 |
| Type 1-200 | 15.57 | 15.57 | 96 | 96 | 27.2% | 200 |
| Type 2-200 | 22.54 | 22.54 | 134 | 134 | 48% | 200 |

$d_0$: Diameter of the twisted thread (after twisting), 0.34 mm

$d_m$: The diameter of the mandrel core (equals to the inner diameter of the TCA), 0.405 mm

$D$: Outer Diameter of the TCA, 1.08 mm

$c$: Spring index $c = D/d_0 = 2.17$

$l_0$: Initial twisted thread length, 350 mm

The five TCAs (type 0, type 1, and type 2) have the following parameters with different values listed in TAB. 2.1 ). Note that the pitch angle during coiling for conventional TCA without free strokes (Type 0) cannot be changed.

$\alpha_m$: pitch angle during coiling process, °(Note that this angle is equal to the pitch angle of the helical groove)

$\alpha_n$: pitch angle corresponding to the natural Length, °

$l_m$: Made length, mm

$l_n$: Natural Length, mm

$S_f$: Free stroke, $S_f = (l_n - l_{min})/l_n$

$T_a$: Annealing temperature, °C

Using the proposed procedure, we fabricate five different TCAs according to two important fabrication parameters in TAB. 2.1: pitch angle during coiling ( $\alpha_m$, equals the pitch angle of the helical groove) and annealing temperature ( $T_g$). We choose the pitch angle because it will influence the initial gaps $l_g$ between neighboring coils (Fig. 2.1). In fact, $l_g = 2\tan(\alpha_m)(d_m + d_0)$ , where $d_m$ and $d_0$ are respectively the diameter of the mandrel core, and the twisted thread (Fig. 2.1 b). The annealing temperature will influence the dynamic response of TCAs as will be presented in the next subsection. Note that we choose these two factors because other fabrication parameters are easy to interpret or have been characterized by others (e.g., the number of plys, the number of rotation inserted, the spring index, and different materials [3]). We categorize the four TCAs according to the pitch angle $\alpha_m$ . For Type 1, 15.57°, and Type 2, 22.54°(see Tab.2.1 for detailed fabrication parameters). For each type, we anneal them under two temperatures (180°C and 200°C) and use a number after type number to indicate the temperature. For example, Type 1-180 is annealed at 180 °C, while Type 1-200 is annealed at 200 °C.

Each of the four TCA has initial gaps between adjacent coils (Fig. 2.3a and b) that allow free strokes without preloading. Each TCA exhibits a natural length $l_n$ at room temperature when no load is applied. It can achieve a minimum length $l_{min}$ when heated, which is the length when all coils contact (Fig. 2.3b). Therefore, the TCA can generate a reversible free stroke $S_f = (l_n - l_{min})/l_n$ without a preload.

To demonstrate the free stroke, we actuate our TCAs using electricity to drag a weight placed on a PVC sheet (Fig. 2.3c). The results show that a single TCA (Type 2-200 in Tab. 2.1) that weighs only 0.03 g can overcome a peak friction force of 0.4 N to achieve a free stroke of $S_f = 48\%$ . By using 5 TCAs (weigh only 0.16 g) in parallel, we can drag a coffee kettle of 2 kg to move 60 mm. The maximum force that the TCA can generate before breaking is 0.78 N (stress 8.59 MPa) when the two ends are fixed under the natural length.

Our TCAs can also be used when a preload is applied (Fig. 2.3d) similar to conventional TCAs without free strokes. In this case, the stroke is defined as $S = (l_{load} - l_{min})/l_{load}$, where $l_{load}$ is the TCA's length after a load is applied. Results show that our TCA (Type 2-200) can generate a stroke of 55% under 10 g load (Fig. 2.3d).

We compare our TCAs with several representative works in Tab. 2.2 by categorizing them based on the coiling method: self-coiling (twist-induced coiling) and mandrel coiling. In general, most of the existing TCAs have negligible free strokes because the coils contact with each other after fabrication. For the strokes with preload, the largest stroke using the mandrel-coiling method is 53% [6], and the largest stroke using the self-coiling method is 45% [73]. The stroke marked

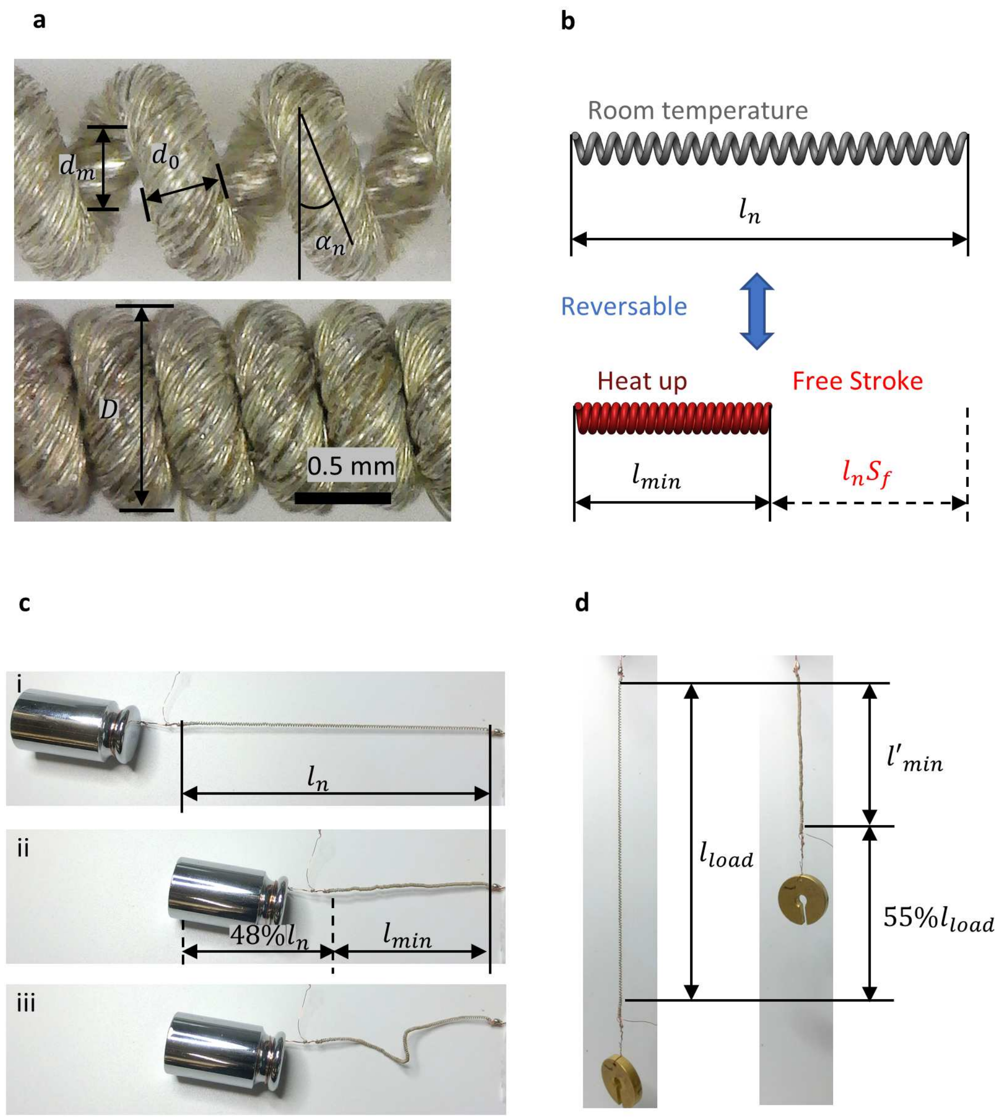


**Figure 2.3:** Our proposed TCAs can contract without preloading (a) Microscopic photos of the TCA in room temperature (top) and after being heated up (bottom). (b) Schematic of the TCA illustrating natural length $l_n$, minimum length lmin, and the free stroke Sf . (c) The TCA pulls a weight against friction of 0.4 N to generate a free stroke of 48%. (d) The TCA lifts a weight of 10 g against gravity to generate a loaded stroke of 55%. $l_{min}$ is the minimum length of the TCA when a load is applied.

**Table 2.2:** Comparison of TCAs' strokes with representative works

| Reference | Precursor Fiber | Coiling | Spring Index | Free Stroke | Stroke | Load for Stroke |
|---|---|---|---|---|---|---|
| Haines [1] | Fishing Line | Mandrel | 5.1 | NA | 49% | 1 Mpa |
| Haines [3] | Fishing Line | Flat Spiral | NA | NA | 46% | NA |
| Wu [6] | Fishing Line | Mandrel | 5.2 | NA | 53% | 100g (1.8 Mpa) |
| Li [70] | Fishing Line | Self-coiling | NA | NA | 18% * | 100 g |
| Yip [4] | Conductive Thread | Self-coiling | NA | NA | 10% | 200 g |
| Cho [71] | Conductive Thread | Self-coiling | NA | NA | 17.8% | 1000 g |
| Almubarak [7] | Conductive Thread | Self-coiling | NA | NA | 22% * | 200 g |
| kim [72] | Spandex & Conductive Thread | Self-coiling | NA | NA | 40.1% | 1.9 N |
| Yang [73] | Spandex | Self-coiling | NA | NA | 45% | 60 g |
| Our Work | Conductive Thread | Helical Mandrel | 3.5 | 48% | 55% | 10 g |

with * indicates that the stroke is normalized by $l_n$ instead of $l_{load}$ and will become smaller when normalized with $l_{load}$.

## 2.2 Characterization of TCAs with Free Strokes

In this section, we experimentally characterize TCAs with free strokes through two steps. First, we obtain the static response with respect to temperature and compare the results with traditional TCAs without free strokes. We also explain the results using a model developed with the system identification method. Second, we experimentally investigate dynamic response with respect to time for the four TCAs with free strokes to choose one that will be suited for actuating soft robots.

### 2.2.1 Static Response with Respect to Temperature

To see why TCAs with free strokes are better than traditional TCAs, we fabricate a traditional TCA using a mandrel without the helical grove: Type 0-180. We compare its static response with

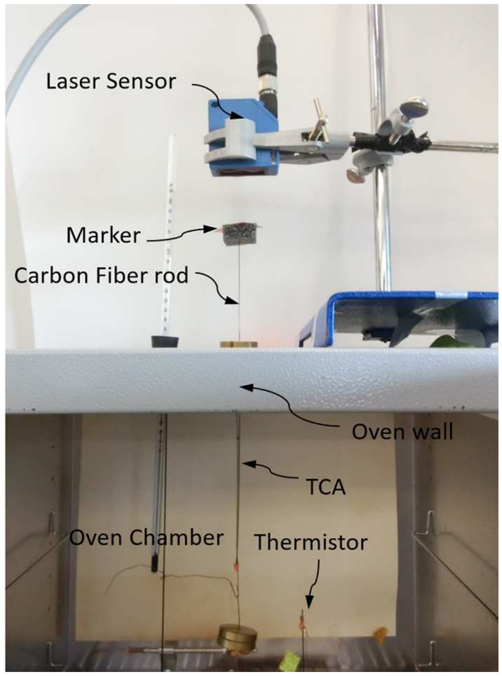


**Figure 2.4:** The experimental setup to obtain the displacement-temperature relationship in the oven. Note that only a small part of the oven is shown in this figure.

the Type 1-180 with free strokes. To make proper comparisons, these two TCAs are made from the same twisted thread with the same parameters (details in Tab. 2.1).

For these two TCAs, we perform static experiments by hanging a weight at the end of each TCA, slowly increasing the TCA's temperature in an oven, and recording the displacement (see Fig. 2.4 for details). Three TCAs that are separately fabricated are tested and their performance is pretty consistent because our TCA is fabricated with the customized, highly automatic machine. Therefore, only one TCA for each type is used throughout the systematic characterization. In the experiments, one experiment is repeated three times. Only the averages of the three experiments are plotted in the following for a clear view and easy comparison, and the maximum standard deviation is 2.14 mm for Fig. 2.5a, b and c.

Experimental results of displacement with respect to temperature are plotted in Fig. 2.5a for three different hanging weights: 0 g, 20 g, and 40 g. From the results, we can observe that all curves almost overlap with each other at the beginning, indicating they can be actuated similarly when the temperature is relatively low ( 70°C) as observed previously by Haines et al [1] and Kianzad et

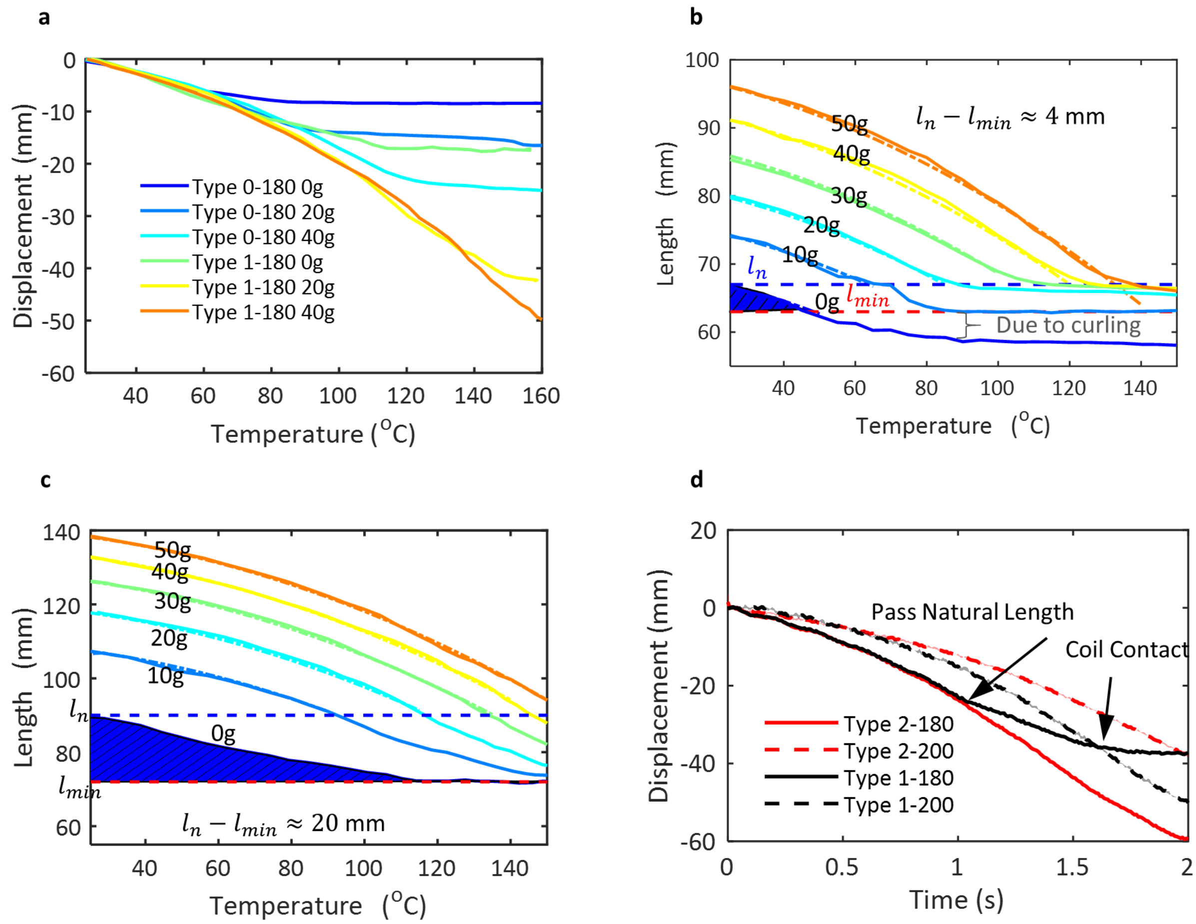


**Figure 2.5:** Characterization of the static response with respect to temperature for a conventional TCA (Type 0) and a TCA with free strokes (Type 1). (a) The displacement with respect to temperature under different weights. (b) The experimental (solid lines) and fitted (dash-doted lines) results of a conventional TCA's (Type 0) length with respect to temperature. (c) The experimental (solid lines) and fitted (dash-doted lines) results of the TCA's (Type 1) length with respect to temperature. (d) The dynamic response with respect to time for four different TCAs with free strokes when actuated by a constant current (1 A) under the same load (20 g). Type 2-180 (red solid line) responds faster with a large displacement. The lines indicate the average and shaded regions indicate the standard deviation. The maximum standard deviation for the four curves is 2.12 mm.

al [74]. However, all curves will flatten out as the temperature becomes high, suggesting the coils in TCAs are contacting each other to prevent further contraction. For different TCAs with the same weight, Type 1 can generate a larger displacement than Type 0, and the difference becomes larger as the weight increases. For instance, under 0 g (from 25 °C to 150°C), Type 0 can contract 4 mm, while Type 1-180 can contract 20 mm. Note that Type 0 seems to contract more than 4 mm because the length of the TCA falls below the minimum length due to curling of its shape. But under 40 g (from 25°C to 150 °C), Type 0 can contract only 24 mm, while Type 1-180 can contract 44 mm. For the same TCA under different weights, the case with the largest weight generates the most contraction since a heavier weight causes more gaps between coils. The To better explain the difference between the traditional TCA and TCAs with free strokes, we can use a mathematical model to describe the relationship between temperature and the displacement [4]:

$$F = k(l - l_n) + c\Delta T \tag{2.1}$$

where $F$ is external load, $k$ is the stiffness coefficient of the TCA, $c$ is the force-temperature coefficient, $l$ is the TCA's length, $\Delta T = T - T_0$ is the increase of temperature with $T$ and $T_0$ the TCA's current and room temperature, respectively.

We can rearrange Eq. (2.1) to get the length in terms of temperature change

$$l = -\lambda \Delta T + l_{n2} (l > l_{min}) \tag{2.2}$$

where $\lambda = c/k$ , and $l_{n2} = F/k + l_n = mg/k + l_n$ . We can use this equation to explain the performance difference for conventional TCAs and TCAs with free strokes in two different cases. First, when $F = 0$ , the convention TCA almost cannot contract anymore since $l_{n2} = l_n \approx l_{min}$ . But for TCAs with free strokes, $l_{n2} = l_n > l_{min}$, there will be a free stroke, and it will contract to $l_{min}$ at a higher temperature. To see this, we plot the length with respect to temperature for the two TCAs in Fig. 2.5b and c. We also label the $l_n$ and $l_{min}$ in the figure. In these two figures, the blue shaded area indicates the amount of the free stroke, and the TCA with free strokes can access a larger shaded area compared with the conventional TCA. Second, for a fixed weight (i.e., $F \neq 0$ ), $l_{n2} = F/k + l_n$ will be larger for a TCA with free strokes since its will be smaller under the same fabrication conditions. In this case, TCAs with free strokes can also generate larger displacements as can be seen from the five curves corresponding to 10, 20, 30, 40, and 50 g in Fig. 2.5 b and c. We also approximate $\lambda$ using a polynomial $\lambda = a\Delta T + b$ in terms of temperature, and plot the fit results as dash-dotted lines, which match well with experimental results. However, the model does not capture the plateau part of the experimental data; therefore it can only be used to predict the first part of the actuation. A more sophisticated model could be developed by considering the contact of coils.

### 2.2.2 Dynamic Response with Respect to Time

The static response for TCAs with free strokes indicates that the displacement largely depends on the pitch angle during coiling ($\alpha_m$). Besides static response, we also characterize how the annealing temperature will influence TCAs' dynamic performance, which is critical if we want to rapidly actuate soft robots, as most current TCA-driven soft robots are in general relatively slow. For example, a soft bending module can only bend 60° after 10 s actuation and a crawling robot can only move 1.2% of its body length per second [75] while the crawler actuated by shape memory alloy wire can move over 200% of its body length per second with a rolling gait [76]. For a given length of twisted thread $l_0$ in Fig. 2.1a and b, a TCA's length after removing from the mandrel after annealing is around $l_m = l_0 \sin \alpha_m$. We call $l_m$ the made length. But in general the natural length $l < l_m$ depending on the annealing temperature ($T_a$).

When nylon is heated Brill transition (160 °C), a crystalline phase transition occurs from a triclinic structure at room temperature to a pseudohexagonal structure above that temperature . This phase transition is known as the Brill transition [77]. If $T_a$ is below the Brill transition temperature of Nylon 6,6 [78], the TCAs, after removing from the mandrel, will automatically reduce its length until all gaps disappear to a minimum length given a sufficiently long time (several days) or subjected to a few heating cycles – a process called creep, which has also been observed by others.

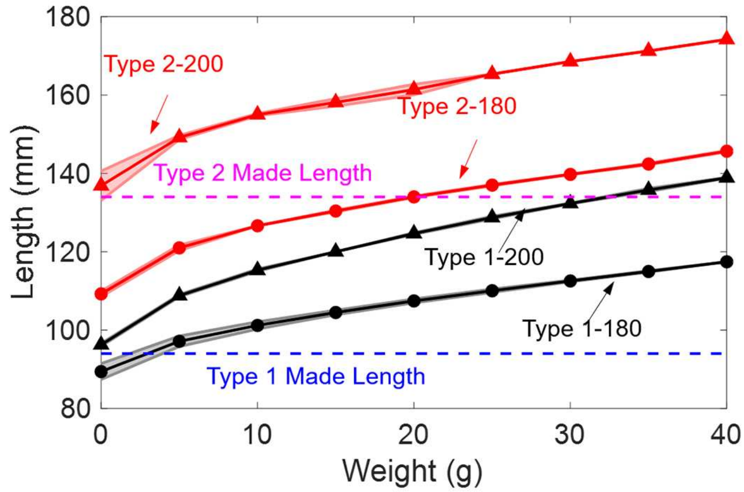


**Figure 2.6:** he steady-state length of the two types of TCAs corresponding to different weights after the creeping process.

When the annealing temperature is higher than 160°C and below 200°C, the TCA will automatically creep to a natural length that is longer than its minimum length but shorter than the made length. For example, the natural lengths of Type 1-180 and Type 2-180 TCA are 92.5% and 80.5% of their made lengths. The reason is that when the annealing temperature is low (e.g., less than 200°C), the annealing process cannot fully remove the stress in the twisted thread. However, the TCAs annealed at 200 °C can almost maintain the made length (Fig. 2.6, Weight = 0). Therefore, the TCA's natural length will not only depend on the pitch angle during coiling, but also on the annealing temperature that determines the extent to which the TCA can hold the designed shape.

With the four TCAs with free strokes, we experimentally characterize their dynamic response under a constant weight (20 g) by applying a constant current (1 A) for 2 s to determine which one is better for actuating soft robots. Since these TCAs are fabricated with precursor threads of the same length, and thus resistance, they almost have the same temperature at the same time in the experiment. Fig. 4d plots the displacement with respect to time and the maximum standard deviation for the four curves is 2.12 mm, less than 4% of the TCA's maximum displacement (60 mm). The results suggest that a TCA with $T_a$ = 200 °C (dash lines) can have a larger natural length, thereby a longer displacement upon actuation, but it has a slower time response compared

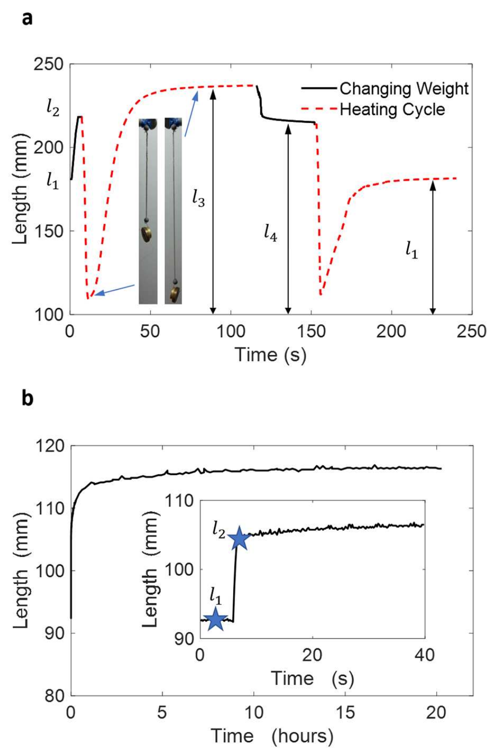


**Figure 2.7:** Temporary length (a) An experiment demonstrating the temporary length with a weight hanging at a TCA's end. (b) A creeping process that lasts for 20 hours.)

with TCAs fabricated with $T_a$ = 180 °C (solid lines). In other words, TCAs annealed at 180 °C (solid lines) can generate faster motion under the same actuation power compared with the TCA annealed in 200 °C (dash lines). That's probably because higher temperature can better fix the shape in the helical shape that has larger gaps between coils. When we focus on the TCA annealed at 180 °C (the solid lines), we observe that Type 1-180 TCA's (black solid line) contraction speed drops at a certain point, and its final displacement after 2 s is less than Type 2-180 TCA (red solid line). The reason is that it passes the natural length since Type 1-180 TCA (black solid line) has a shorter natural length than Type 2-180 TCA (red solid line). Among the four types of TCAs, Type 2-180 TCA (red solid line), which is annealed at a lower temperature but with a longer made length, is a better candidate for actuating soft robots since it actuates faster with a large displacement.

### Temporary Length and Aging Test

We also observe a temporary natural length due to the creep (viscoelasticity) of Nylon 66, the material of the threads used for fabricating TCAs with free strokes. Such a phenomenon is also mentioned in Ref [79, 80] for TCAs made of fishing lines. When a load is hanged at the end of a TCA, the length of TCA will first instantly increase due to the elastic stiffness of the spring structure and then gradually increase over time (Fig. 2.7b). After a TCA creeps to one length induced by a load, due to its actuation capability, it can return to its natural length after the load is removed (but usually takes a pretty long time in room temperature). If TCAs are embedded into a soft body in these temporary natural lengths after the fabrication process, the TCA will eventually recover to its natural length, which will cause undesired initial deformation of the soft body. Therefore, we first conduct one heating cycle (in addition to the training process) before embedding the TCA into a soft body to prevent the undesired deformation. Also, we tested the "aging" of the TCA (Type 1-180) by actuating it for 10,000 cycles (0.25 Hz) at 2 MPa load, and the results show that the stroke changes little (2%). The viscoelasticity might be also the reason for the hysteresis during actuation and more sophisticated treatment can be found in other references [81, 82].

Our TCAs with free strokes exhibit a temporary length right after fabrication or subject to an external load due to the creep of polymer materials. After the annealing process and removing from the mandrel, it will slowly (around one day) creep to its natural length from a *temporary natural length* (slightly shorter than the made length). Such a creeping process can be sped up by several heating cycles. Therefore, we apply 10 heating cycles before we embed a TCA into a soft body when fabricating soft robots to make sure the TCA has a natural length instead of a temporary natural length.

When subject to an external load, the TCA also exhibits a temporary length. We conduct an experiment to demonstrate the temporary length. In the experiment, a Type 1-180 TCA is hanged and a motion tracking system (OptiTrack, V120:Trio) is used to track the length change of the TCA by sticking two markers at its two ends (see inset in Fig. 2.7a). Fig. 2.7a shows the TCA's

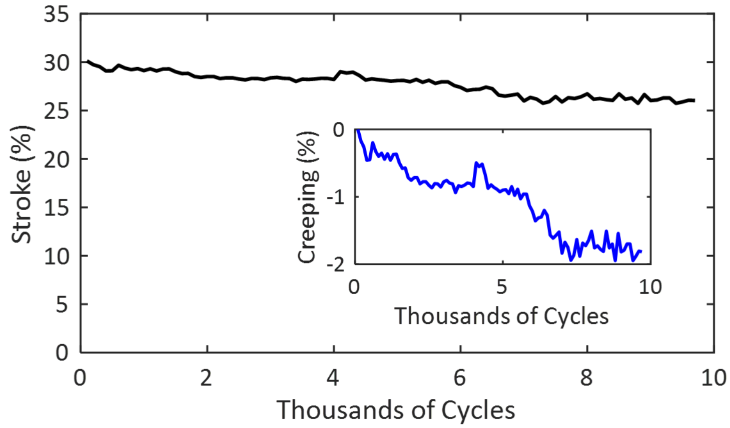


**Figure 2.8:** Tensile stroke versus actuation cycle for a Type 1-180 TCA that is driven electrothermally at 0.25 Hz under a 2-MPa load (each point averages 100 cycles). The inset provides creep (decrease of the stroke) as a function of cycle.

length with respect to time. At the beginning, the TCA is at its natural length $l_1 = l_n$ with no load at the end. Then a weight m = 20 g is hanged at its end, and the length becomes $l_2$ due to the instant elastic deformation. After a heating cycle is applied, the length starts to creep to $l_3$ after the TCA cools down for about 100 s. Also, when we remove the weight, the TCA's length (becomes $l_4$) will not able to immediately recover to the natural length $l_1$. The creeping effect will temporally keep the TCA's length, which is a *temporary length*. Finally, the length recovers to $l_1$ after we apply another heating cycle. We find $l_1 < l_2 < l_4 < l_3$, and the difference between $l_2$ and $l_3$ is not only due to instant elastic deformation but due to creep, which is accelerated by the heating process. In another experiment, we first hold a weight of 20 g with hands when the TCA is at its natural length $l_1$. Then, we suddenly release the weight, the length will first instantly increase to a length $l_2$, and finally creep to a steady-state length after tracking the length of the TCA for 20 hours as in Fig. 2.7b. When we remove the weight, it takes also the same amount of time to recover to the natural length.

The setup that is used for measuring the temporary length is used again in this test. We hang a weight of 20g (2 MPa) at the end of the TCA (Type 1-180) and actuate it at 0.25 Hz for 10,000 cycles. Fig. 2.8 provides the stroke as a function of cycle (each point averages 100 cycles). The results show that the long-time creeping of the stroke is around 2% after 10,000 cycles.

## 2.3 Self-sensing and Closed-loop Control

Remarkably, besides actuation, it is recently found that TCAs also have self-sensing capabilities: its electrical property (e.g., resistance or inductance) will change when subject to external stimuli (temperature or force) [23, 24, 83]. For TCA made of conductive sewing threads, we explored the change of electrical resistance when the TCA is not actuated [23]. The dependence of TCA's resistance on temperature, external load, and displacement has also been investigated [84].

Despite recent investigations, existing works [23] largely only explore the sensing aspect when the TCA is not actuated, i.e., only using them as sensors. The only exception is the work by Weijde et.al. using TCAs made of a fishing line with heating wires. They realized closed-loop control of such TCAs using inductance and resistance as feedback by establishing a relationship among the TCA's force, displacement, input power, and inductance [24]. However, they only demonstrated closed-loop control for a single TCA instead of using it to accurately actuate robots and it requires extra devices to sense both inductance and resistance.

In this section, we aim to accomplish an integrated actuation and sensing scheme for TCAs made from conductive sewing threads [2]. There are two key points for the scheme: 1) the TCA can sense environmental stimuli and simple works as a sensor (nerve) when it is not actuated. 2). The TCA can work as a sensor and actuator (nerve and muscle) when it is actuated. By integrating the two functions, we can achieve innervated TCA

However, it is challenging to realize such a function because of the main difficulty arising from the fabrication. Some fabrication methods will result in random resistance while a TCA is actuated because the coils in it will randomly contact each other when the TCA contracts. For example, the bundled TCAs have coils touching each other all the time [4, 85], and TCAs fabricated using conventional methods (self-coiling or mandrel coiling) will have coils contacting each other soon after it is actuated due to the limited stroke.

To address the problem, we the TCA with a free stroke as introduced in the previous section that can generate sufficient stroke before coil contact [86]. The displacement of the TCA can be reflected by its resistance change during the actuation, and thus the closed-loop control of the

**Table 2.3:** Main parameter for the TCA in the sexperiments

| Definition | Unit | Value |
|---|---|---|
| Twisted fiber length | mm | 350 |
| Twisted fiber diameter | mm | 0.34 |
| Outer diameter | mm | 1.08 |
| Natural length | mm | 110 |
| Made length | mm | 133.5 |
| Unit resistance | ohms/dm | 6.7 |
| Stroke with no weight | / | 35.7% |

displacement could be realized taking resistance as feedback. The TCA used in section is the type 1-180 TCA, and its main parameters are shown in the Tab 2.3.

### 2.3.1 Characterization of the Self-sensing Capability

First, we discuss the variables on which the resistance depends on when the TCA is actuated. We treat the temperature as an intermediate variable to characterize how the resistance depends on the displacement and the load. After that, we obtain the resistance change after a load is applied when the TCA is not actuated, which can serve as a signal to trigger TCA's motion.

#### Dependence of the Resistance on State Variables

The conductive sewing thread is conductive due to the silver traces painted on the yarns. Before the resistance characterization, we need to determine the variables on which the resistance may depend on when the TCA is actuated by Joule heating. According to existing modeling work of TCAs [4, 27, 33], the thermal-mechanical relationship can be expressed as a nonlinear function

$$f(\Delta T, \Delta x, F, \dot{x}) = 0 \tag{2.3}$$

where $\Delta T$ is the temperature change, $\Delta x$ is the displacement, $F$ is the external load, and $\dot{x}$ is the velocity of the actuation. For example, a first-order function is $k\Delta x + b\dot{x} + c\Delta T - F = 0$, where $k$, $b$ and $c$ are respectively the TCA's stiffness, damping coefficient, and temperature contribution coefficient (N/°C).

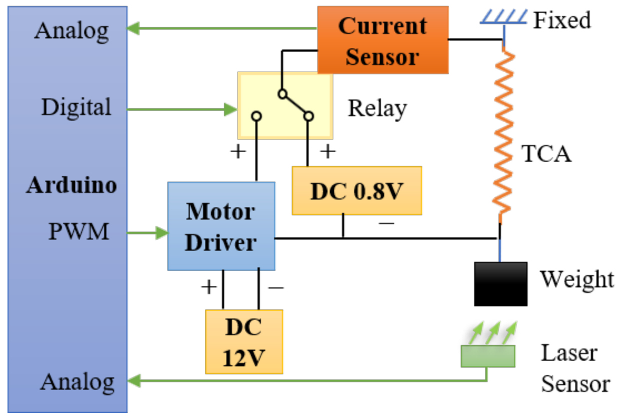


**Figure 2.9:** The setup used to measure the resistance-length relationship and control the TCA

The TCA's resistance $R$ can also be expressed as a nonlinear function in terms of the variables $(\Delta T, \Delta x, F)$ [84].

$$R = g(\Delta T(\Delta x, F), \Delta x, F) = h(\Delta x, F) \tag{2.4}$$

In Eq. (2.4), the viscous effect is ignored due to its small quantify. We express temperature as a function depending on $\Delta x$ and $F$, and thus $\Delta T$ be treated as an intermediate variable, so that $R$ can be fully determined by $\Delta x$ and $F$.

When a TCA is not actuated and works as a sensor, the equation Eq. (2.4) can be further simplified because $\Delta x$ will then merely depend on $F$. So we can easily find the relationship between either two of the three variables ($R, \Delta x$ and $F$) by experiments.

### Resistance - length Relationship of an Actuated TCA

In this work, we first try to characterize how the resistance changes with respect to the length (R-L) and the displacement (R-D) of the TCA when the applied force $F$ is known. The most common case is using the TCA to lift a weight hanged at the end of the TCA against gravity. For such a case, we can assume the load $F$ is equal to the gravity of the weight because the maximum acceleration of the weight is 0.2 m/s$^2$ in our experiments, which is negligible ($<3\%$) compared to the gravity.

We build a driving-sensing module (DSM) shown in Fig. 2.9 that can be used to 1) characterize the TCA; 2) conduct the feedback control experiments. The DSM can switch between two separate circuit loops using a relay module. The first loop that can conduct the feedback control comprises a motor driver (Pololu MC33923) and a high side voltage-current sensor (Adfruit INA 219, accuracy 1%, resolution 0.8 mA) and the second loop that is only for sensing when TCA is not actuated includes the same current sensor but a smaller DC power source (a step-down buck converter). Although the motor driver can generate a lower voltage, it is in a PWM (Pulse-width modulation) form that introduces noise since a filter has to be used to get an equivalent averaged value of the voltage. Our motor driver, like most motor drivers, has an integrated current sense, but their accuracy can be especially poor at low currents and vary from unit to unit. Therefore, we use an extra current sensor to add more consistent and accurate current sensing to our system.

In the experiments, a TCA that has a natural length of 110 mm is hanged with a weight at its bottom end and a laser displacement sensor (OPT2006, Wenglor sensoric GmbH) is mounted at the bottom of the weight to measure its displacement. The motor driver, the current sensor and the laser sensor connect to an Arduino Uno board to make sure all the signals are synchronized.

There are two variables in the experiments: the weights and the actuation velocity. So for each weight (10 g, 20 g, 30 g, 40 g, and 50 g), we actuate the TCA with different velocity using constant voltages (12 V and 10 V). Note that, after a weight is hanged at the end of our TCA, it takes a long time (around 24 hours from our experimental results) for the TCA to reach its equilibrium length due to viscoelasticity of the Nylon material, which is known as creeping. However, the creeping process can be significantly accelerated by increasing temperature. We apply a heating cycle when using a new weight to make sure that every experiment starts from the equilibrium state.

For each case, we repeat experiments three times and plot their average and error bound. Figure 2.10(a) and (b) show the resistance-length and resistance-displacement relationship when the TCA is actuated using $U = 12$ V. It is obvious that the resistance gradually increases when the TCA contracts and the R-L relationship is continuous and monotonic. These two properties lays the foundation for using resistance as feedback to control a TCA's length. Also, we find that the R-

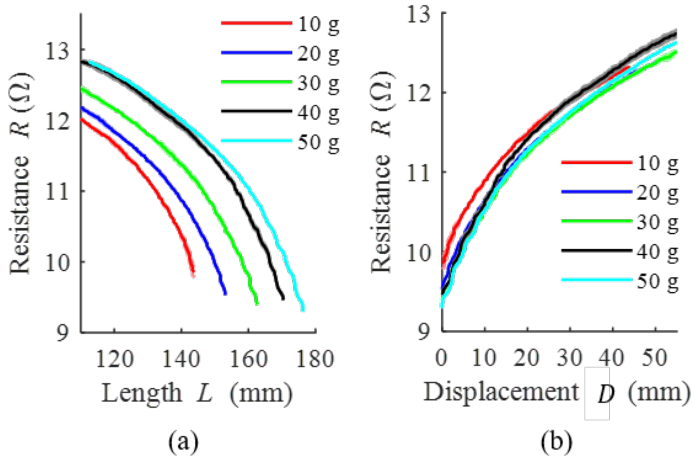


**Figure 2.10:** (a) The resistance-length relationship for different weights. (b) The resistance-displacement relationship for different weights.

L relationships when the TCA is actuated with 10 V (Not shown in the figure) are almost the same with the results when the TCA is actuated with 12 V for the same weight. It implies that a smaller actuation velocity will not influence the D-R relationship, so we can use this relationship even when the contraction velocity reaches 0, which corresponds to a holding function that will be discussed in Sec 2.3.2.

Furthermore, the R-D curves corresponding to different weights almost overlap with each other, as shown in Fig. 2.10 (b), and it implies that the R-D relationship is not sensitive to the weight when the stress corresponding to the weight is less than 70% of is the breaking stress of the TCA (the TCA breaks at when the external force reaches around 0.7 N). This further implies that we can use the same D-R curve to control the displacement of the TCA even when the weight is unknown.

### Unactuated TCA as a Sensor

When the TCA is not actuated, it can be used as a displacement or load sensor [23]. We experimentally measure a TCA's resistance and reaction force by pulling the TCA longer. In the experiment, a force stand (ESM 303 with M5-12 force gauge, Mark-10 Inc.) is used to drag the TCA with a constant speed. The displacement and force are sampled using the force stand's displacement sensor and the force gauge. At the same time, the TCA's resistance is also measured

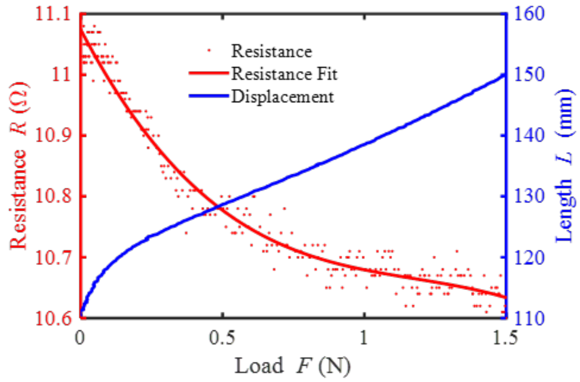


(a)

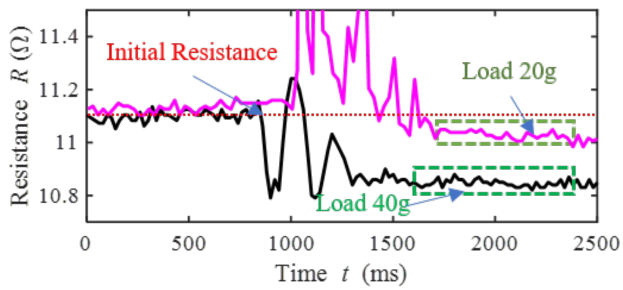


(b)

**Figure 2.11:** (a) The resistance and the length with respect to the applied force when the TCA is not actuated. (b) The response of the resistance when 20 g or 40 g is applied on the end of the TCA

by applying a 0.8 V voltage on it. The current is only around 80 mA, which will only increase the TCA's temperature 1-2 °C (Obtained using FLIR E8 Infrared Camera), and won't actuate it at all.

Figure. 2.11(a) shows that the resistance and the length of the TCA change with respect to the applied force. Since the current is low, there is noise during the measuring of the resistance, but the trend is still obvious: the resistance decreases when the force increases as suggested by our previous work [23]. However, the relatively larger spring constant (2.2) compared to the TCA in our previous work (1.8) results in a smaller rate change of the resistance – the previous one is 1.8 ohms and this one is 0.55 ohms both for 50% unit strain (displacement).

Based on this principle, a TCA can detect how much load is applied by monitoring its resistance, though reliable measurement may require a high sensitive current sensor and active high-order filters to be robust enough. Figure 2.11(b) shows the resistance change with respect to time when a 40 g and a 20 g are instantly applied at the end of the TCA (as in the supporting video). In order to distinguish different loads, we have to logically ignore the vibration process, which means that the action will be confirmed when a lower resistance is continuously sensed as shown in the green boxes of Fig. 2.11 (b). After sensing the different loads, the TCA can respond according to the load, for example, lift 40 mm when a 40 g is applied (see section 2.3.2 and the supporting video).

### 2.3.2 Closed-loop Control using Self-sensing

With the relationship between the resistance and the displacement, we first conduct a closed-loop control of the displacement using a PI controller and then discuss the influence of the PI parameter. Combining the sensing capability when the TCA is and is not actuated, we can demonstrate the innervated TCA that can sense external stimuli and respond to them.

#### Displacement Closed-loop Control of the TCA

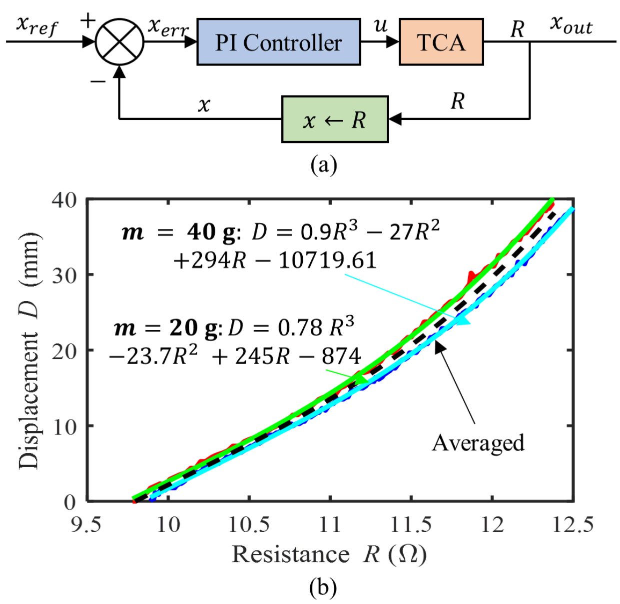


**Figure 2.12:** (a) Schematic of the PD control. (b) The fitted D-R curve used for the feedback control

We demonstrate the closed-loop control of a TCA 's displacement using a PID controller. As shown in Fig. 2.12(a) the closed-loop control is performed by closing the loop on the error between a reference displacement and the displacement calculated from the measured resistance using the D-R relationship from the characterization. For the D-R relationship, we have two choices: the averaged curve or the specific curve corresponding to a weight. Using averaged curve will reduce the accuracy but this method does not require a known load, while using the specific curve will make the control more accurate, but it requires a known weight beforehand. However, it is not difficult to know the weight, because the sensing function described in section 2.3.1C allow us to know the approximate weight (20 g or 40 g).

A three-order polynomial is used to fit the D-R curve when the weight equals 20 g and 40 g, as shown in Fig. 2.12 (b) and the root-mean-square error ( RMSE ) for the two curves are respectively: 0.2184 mm and 0.3486 mm. When the averaged curve is used, there will be a maximum steady-state difference less than $\pm 20\%$ mm for step-response experiments compared with the case using the right curve. The error might be reduced by modeling the resistance to compensate for the error, but it will be our future work and not discussed. The following studies are based on using the specific D-R curve corresponding to the weight.

The experiments are conducted using the driving-sensing module. The output voltage of the motor driver is a PWM wave (4 kHz), and therefore the current in the TCA is also in a PWM form. A digital filter (Modified moving average method) is used to obtain the equivalent moving average of the current to calculate the resistance. Also, the current sensor has an internal ADC based on a delta-sigma ($\Delta\Sigma$) front-end with a 500kHz typical sampling rate that has good inherent noise rejection.

A PI controller is used in this section, and we find that an integral controller is necessary to reduce the steady-state error, since the TCA has to be actuated to maintain the target position. Figure 2.13(b) shows the step response (40 mm) of the TCA lifting 20 g when $K_P = 10$ is used for all cases. When $K_I = 0$, the steady-state error $e_s \approx 30\%$ and when $K_I = 0.01$, the $e_s$ is reduced to around 12%. The optimal $K_I$ that we find is 0.015 that can maintain the $e_s < 5\%$. However, when the $K_I$ is too large, the system starts to oscillate (see the supporting video).

The influence of the $K_P$ is studied using the step response (40 mm) of the TCA lifting 40 g. A larger $K_I = 0.02$ is used to suppress the steady-state error to be less than 5%. When $K_P = 5$, the rising time is longer. When $K_P$ increases, the rising time decreases. But overshoot happens when $K_P = 20$. The rising time is also limited by the maximum voltage 12V (thus maximum power) that we can use. Figure 2.13(d) shows that the applied power spikes and decays to achieve a step response in the output displacement of the TCA. Note that the steady-state of the power is a constant instead of zero to maintain the position of the weight.

The TCA is a thermal-driven actuator, therefore its performance subjects to the influence of the environmental temperature. But a closed-loop control endows a strong rejection to the disturbance from the environment. The black dashed line in Fig. 2.13(a) shows the TCA ($K_P = 10, K_I = 0.015$) can adapt to a disturbance (blowing air). The blowing air will increase the convection heat transfer rate and thus the TCA loses energy more efficiently causing the decrease of the displacement.But the system finds a new balance and more energy is input to the TCA to maintain the displacement as shown in Fig. 2.13(c).

**An Innervated TCA with Integrated Sensing and Actuation**

Combining the sensing capability while a TCA is actuated and not actuated, we further demonstrate a TCA as an innervated actuator. In our experiments, the TCA is hanged at its natural length and will first sense the weight that we manually add and then respond according to the weight. As shown in Fig. 2.14(a) and (b) and the supporting video, when a 20 g is added, the TCA will just lift the weight 20 mm and then hold the position for 2 sec and then lift another 20 mm and hold another 2 more seconds; when a 40 g is applied, the actuator will lift the weight 40 mm and then hold the position (shown in the supporting video). Note that the TCA cannot be always reliably triggered due to the relatively small change when 20g is applied, but that can be solved using a high sensitive current sensor and low pass filters, which will be our future work.

## 2.4 Chapter Summary

This chapter presents the TCAs with free strokes that are suitable for actuating soft robots. The TCA has an initial state with gaps between coils so that it can contract without preloading, generating around 50% free strokes that cannot be generated by traditional TCAs. We characterize its static response with respect to temperature and dynamic response with respect to time. The characterization results suggest that a relatively low annealing temperature and a large pitch angle during coiling can generate TCAs that respond faster with larger strokes. The TCA's self-sensing capability is characterized to realize closed-loop control and innervated actuation.

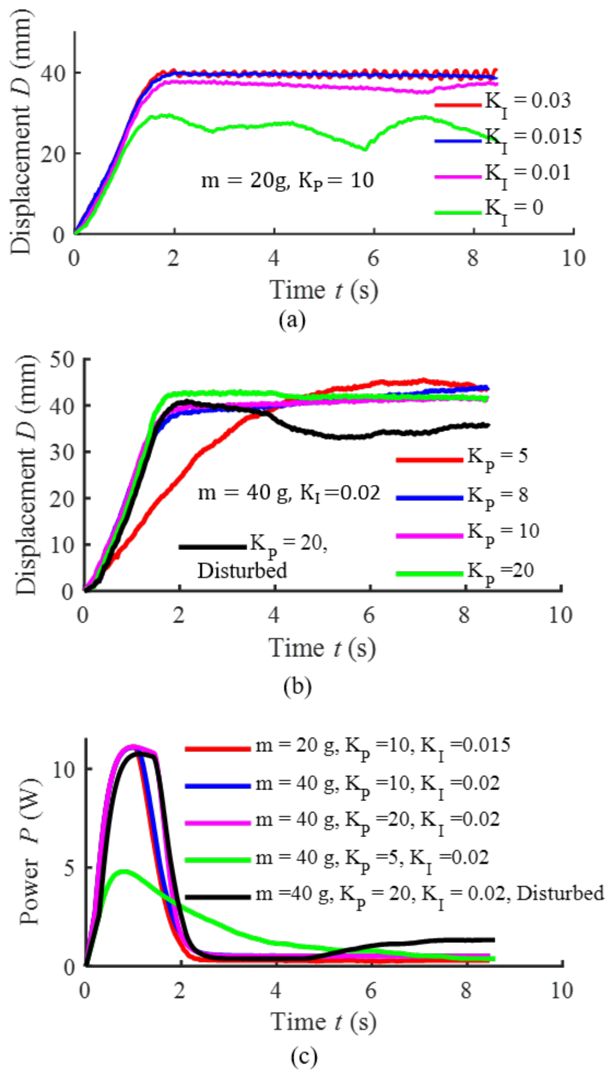


**Figure 2.13:** (a) Step response of the displacement with a wight of 20 g using $K_P = 10$ and different $K_I$. (b) Step response of the displacement with a wight of 40 g using $K_I = 0.02$ and different $K_P$. (c) The input power for the step response experiments.

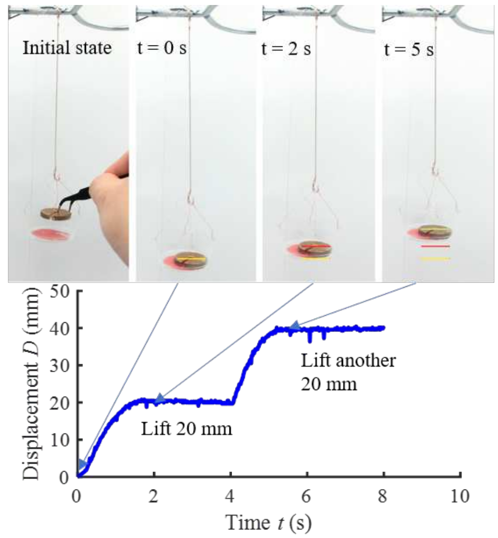


**Figure 2.14:** (a) The sequential snapshots for the TCA to autonomously lift 20g. (b) The displacement of a 20 g weight with respect to time

# Chapter 3

# Physics Based Modeling of TCAs

To better facilitate the applications for TCAs, it is critical to establish general and precise models for different types of TCAs (e.g., self-coiled, free-stroke, conical, etc.). Although several modeling methods have been proposed recently, existing models either fail to capture the nonlinearity during large deformations or cannot model TCAs with non-uniform geometries. In this work, we establish a general framework for modeling TCAs using the Cosserat rod theory that can capture the nonlinearity of large deformations and simulate TCAs with non-uniform geometries. Furthermore, we show existing methods are special cases of our general model. Comprehensive statics and dynamics experiments are conducted to verify the proposed model, and the results demonstrate that the model is more accurate than existing ones, especially when a TCA is subject to large deformations. Given the wide applications of TCAs, our general model can help better design, optimize, and control systems/robots/devices driven by different types of TCAs.

TCAs can be fabricated to have different configurations (Fig. 3.1) such as self-coiled, free-stroke, conical, etc. Generally, TCAs are fabricated through a two-step process. The first step is the same: twisting a polymer fiber to generate a twisted fiber, whereas the second step differs: using the twisted fiber to generate a coiled shape. Self-coiled TCAs (Fig. 3.1a) are fabricated by self-coiling in the second step. Such TCAs can produce large forces but have relatively small strokes (around 10% to 20%) and normally require prestretch before usage [1]. Free-stroke TCAs (Fig. 3.1b) are fabricated by coiling a twisted fiber along a mandrel with helical grooves in the second step. They can provide moderate actuation forces with relatively large strokes ($> 50\%$) without prestretch [86, 87]. Conical TCAs (Fig. 3.1c) are fabricated by coiling a twisted fiber along a conical mandrel. They can generate weak forces but with large, even dual-side strokes when the coils pass each other [3].

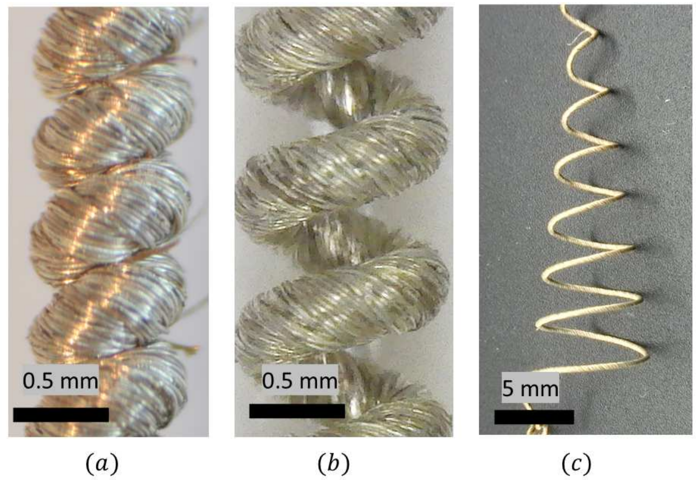


**Figure 3.1:** The photos of three types of TCAs made of conductive sewing threads. (a) Self-coiled TCA. (b) Free-stroke TCA. (c) Conical TCA.

# 3.1 Thermal Model and Fiber Actuation Model

TCAs made of conductive threads are used in this work since they can be directly actuated using electricity and respond much faster than TCAs made of fishing lines wrapped with heating wires. Therefore, our modeling framework starts with a thermal model to obtain a TCA's temperature given input power, and then a fiber actuation model to predict the amount of fiber untwisting from the temperature increase for the twisted fiber in a TCA.

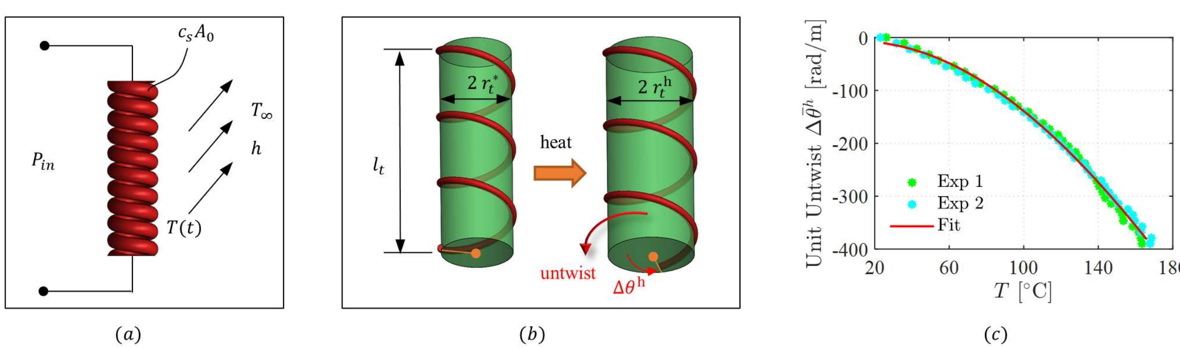


**Figure 3.2:** (a) The schematic for the thermal model. (b) The schematic for the fiber actuation model. The green cylinder represents a twisted fiber. The red helix is a monofiber with a constant length $l_f$. (c) Experimental and fitted results of the unit untwist of the twisted fiber with respect to temperature.

### 3.1.1 Thermal Model with a Time-varying Input

For TCAs made of conductive threads, their electrical resistance strongly depends on the loading condition and changes over the actuation process ($\sim 20\%$) [88]. Therefore, we cannot assume a constant resistance for modeling. In this case, we directly use the time-varying input power as the real-time input of the thermal model to achieve a better accuracy.

As shown in Fig. 3.2(a), the 1D thermal diffusion equation is

$$m_t c_p \dot{T} = -hc_s A_0 (T - T_\infty) + P_{in} \tag{3.1}$$

where $T$ is a TCA's temperature, the $\dot{}$ represents the derivative with respect to time, $m_t$ is the weight of the TCA, $c_p$ is the specific heat, $T_\infty$ is the ambient temperature, $h$ is the natural convection coefficient, and the method to determine $h$ is described in Subsection 3.5.2. $A_0 = 2\pi r_t l_t$ is the surface area of the twisted fiber without considering roughness, with $r_t$ and $l_t$ the diameter and length for the twisted fiber, respectively. $c_s = 2.5$ is used to adjust the surface area due to its roughness (see Fig. 3.1). In fact, a twisted thread is made of infinite many yarns twisted together, each yarn is made of infinite many thin fibers, and each fiber has a circular cross section. In this case, the outer surface area is scaled up twice, and the scaling factor for each scaling is $\pi/2$, which is the ratio between half perimeter of a circle to its diameter. We calculate $h$ from experimental data using the regression method after $c_s$ is determined. $P_{in}$ is the power input into the TCA that is directly monitored in a control circuit using a sensor (details in Section 3.4.4). With the initial condition as $T(0) = T_0 = T_\infty$, Eq. (3.1) can be numerically solved using an ordinary differential equation (ODE) solver in Matlab (e.g., $ode45$).

### 3.1.2 Fiber Actuation Model

After the temperature for a TCA is known, we can solve the amount of untwisting for the twisted fiber in the TCA due to thermal expansion. Such untwisting happens since the twisted fiber expands much more in the radial than the longitudinal direction. Therefore, given a temperature input, we first find the radius of the twisted fiber resulted from radial expansion, and then use the radius to solve the amount of untwisting.

The twisted fiber's radius $r_t^{\mathsf{h}}$ after heating is an integration of the coefficient of thermal expansion (CTE) in radial direction $\alpha_{\perp}$:

$$r_t^{\mathsf{h}} = r_t^{*}(\int_{T_0}^{T} \alpha_{\perp} dT + 1) \tag{3.2}$$

where $r_t^{*}$ and $r_t^{\mathsf{h}}$ are the radius at temperature $T_0$ and $T$, respectively. Denote the ratio between $r_t^{\mathsf{h}}$ and $r_t^{*}$ as $\Gamma(T) = r_t^{\mathsf{h}}/r_t^{*} = \int_{T_0}^{T} \alpha_{\perp} dT + 1$. Note that $\alpha_{\perp}$ is not a constant and strongly depends on the temperature [89]. We will use a superscript * to represent the variable in the original reference state (ORS) when no heat and no load is applied, which are fixed parameters that can be measured; we use a superscript $\mathsf{h}$ to indicate the variables are corresponding to the heated reference state (HRS) when the heat is applied but no load is applied. For example, $r_t^{*}$ and $r_t^{\mathsf{h}}$ are the twisted fiber's diameter at the ORS and HRS, respectively. The variables without the superscript represent a general state when a force is applied and/or when the temperature is increased.

To obtain the amount of untwisting from the fiber's radius expansion, we use a single helix model [90]. The model assumes the monofilaments in a twisted fiber form the same helical shape like one single helix wrapped on a cylinder that will expand in the radial direction as shown in Fig. 3.2(b). The helix satisfies

$$l_f^2 = (r_t^{\mathsf{h}}\theta)^2 + l_t^2 \tag{3.3}$$

where $l_f$ is the length of the original fiber before twisting, $l_t$ is the length of the helix (the twisted fiber), $\theta$ is the total twisting angle: $\theta = 2\pi n_t$ with $n_t$ the number of twists inserted into the twisted fiber.

$l_f$ and $l_t$ can be assumed to be constant since they remain almost the same when the fiber's temperature increases [90]. Therefore, $r_t^{\mathsf{h}}\theta$ will keep constant: $r_t^{\mathsf{h}}\theta = r_t^{*}\theta^{*}$. Denote the amount of untwisting due to heat as $\Delta\theta^{\mathsf{h}}$, we can obtain $\Delta\theta^{\mathsf{h}} = \theta^{\mathsf{h}} - \theta^{*} = \theta^{*}(r_t^{*}/r_t^{\mathsf{h}} - 1)$. Further denote the amount of untwisting per unit length as $\Delta\bar{\theta}^{\mathsf{h}} = \Delta\theta^{\mathsf{h}}/l_t$, we have

$$\Delta\bar{\theta}^{\mathsf{h}} = \frac{\theta^*}{l_t}(\frac{r_t^*}{r_t^{\mathsf{h}}} - 1) = \frac{\theta^*}{l_t}(\frac{1}{\Gamma(T)} - 1) \tag{3.4}$$

From Eq. (3.4), we can obtain $\Delta\bar{\theta}^{\mathsf{h}}$ from the radius ratio $\Gamma(T)$, which is challenging to model. Therefore, we use a second-order polynomial $c_2T^2 + c_1T + c_0$ to approximate $\Gamma(T)$ and experimentally obtain the coefficients $c_i$ ($i = 0, 1, 2$) by directly monitoring the amount of untwisting for a twisted fiber. Specifically, we first anneal the same twisted fiber for fabricating TCAs shown in Fig. 3.1 in a straight shape with two ends fixed in an oven (more details in Sec. 3.4.1). The straight twisted fiber is then hanged in an oven, and a 1 g weight is attached at its end to keep the fiber straight. When the oven is gradually heated, a camera is used to capture the fiber's untwisting through the oven's transparent window and a thermal sensor is used to record the temperature. Fig. 3.2(c) shows the unit untwist with respect to the temperature and the approximation using a second-order polynomial with $c_0 = 3.5 \times 10^{-6}$, $c_1 = -6.7 \times 10^{-5}$, $c_2 = 1$ that provides enough accuracy with an MSRE = 4.1 rad/m, which is 2.3 degrees for a twisted fiber with a length of 1 cm.

With the experimentally obtained $\Gamma(T)$, we can derive the amount of untwisting given a temperature for the twisted fiber using Eq. (3.4). This amount of untwisting is used as an input for the coil kinetostatic model in the next section.

## 3.2 Kinetostatic Model Using Cosserat Rod Theory

The Cosserat rod model can be used to formulate a balance equation between the external wrench (force and moments) and the internal wrench on the twisted fiber in a TCA. In this section, we establish the system of equations of the Cosserat rod model for the kinetostatics of a TCA, derive the moduli of a twisted fiber as a function of temperature and strain, obtain the reference configurations required for numerical implementations, and establish a simplified dynamics equation for TCAs.

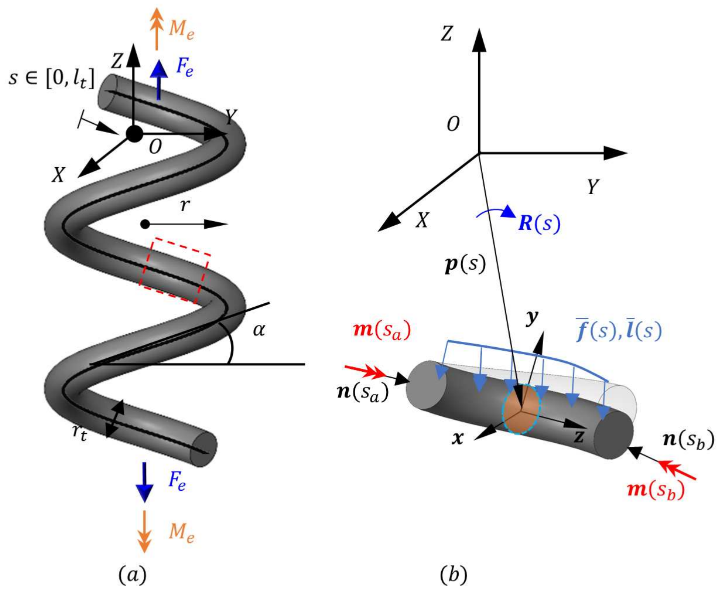


**Figure 3.3:** The schematic for the Cosserat rod model (a) The loading condition of the TCA. The top end is fixed (fixed end), and a force $F_e$ and a moment $M_e$ are applied at the bottom end. (b) An arbitrary section of rod (the red box in (a)) from $s = s_a$ to $s = s_b$ subjects to distributed forces $\bar{f}$ and moments $\bar{l}$. The internal forces $n$ and moments $m$ are also shown.

### 3.2.1 Cosserat Rod Kinetostatic ODEs

The twisted fiber in a TCA can be considered as a slender rod as shown in Fig. 3.3(a), and the Cosserat rod model [60] assumes the rod is composed of infinitely many rigid cross sections along the rod's centerline defined as the curve passing through the centroids of all the cross sections. We use arc length $s \in [0, l_t]$ to denote the location of a cross section along the centerline.

We establish a global (fixed) frame ($OXYZ$) located at the center of the TCA's fixed end. As shown in Fig. 3.3(b), we also establish a body frame ($oxyz$) for a rigid cross section at $s$ with $o$ located at the centroid, $z$ direction along the rod's tangent direction, and $x$, $y$ aligned with the principal axes of the cross section. The orientation of the body frame with respect to the global frame can be represented as a rotational matrix $R(s) \in$SO(3), whereas the position of $o$ in the global frame can be represented as $p(s) \in \mathbb{R}^3$. With $R(s)$ and $p(s)$, we use a homogeneous transformation matrix $g(s) \in SE(3)$

$$g(s) = \begin{bmatrix} R(s) & p(s) \\ 0 & 1 \end{bmatrix} \tag{3.5}$$

to represent the orientation and position of a rigid cross section at $s$ in the global frame.

With the notation in [91], the kinematics of a TCA as a Cosserat rod is $g' = g\widehat{\xi}$, where $'$ is the derivative with respect to $s$, and $\xi = [u^T, v^T]^T \in \mathbb{R}^6$ is the spatial twist (strain) representing the relative configuration change between adjacent cross sections along the centerline, with $u \in \mathbb{R}^3$ and $v \in \mathbb{R}^3$ the angular and linear strain component, respectively. The superscript '$T$' denotes the transpose of a matrix. The 'hat' operator $\widehat{\cdot}$ is a mapping from $\mathbb{R}^3$ to $\mathfrak{so}(3)$ or $\mathbb{R}^6$ to $\mathfrak{se}(3)$, e.g., $\widehat{\xi} = \begin{bmatrix} \widehat{u} & v \\ 0 & 0 \end{bmatrix}$. We decompose $g' = g\widehat{\xi}$ into the angular and linear component to facilitate our numerical simulation using non-unit quaternion (detailed in Section 3.4.2)

$$\begin{aligned} R' &= R\widehat{u} \\ p' &= Rv \end{aligned} \tag{3.6}$$

A complete nomenclature is listed in Tab. 3.3.

The statics equation for an arbitrary cross section of the rod as in Fig. 3.3(b) is

$$\bar{W}_e - ad_{\xi}^T W + W' = 0 \tag{3.7}$$

where $\bar{W}_e = \begin{bmatrix} \bar{l}^T, & \bar{f}^T \end{bmatrix}^T$ is the distributed external wrench with $\bar{l}, \bar{f} \in \mathbb{R}^3$ as the moment, force per unit arclength applied to the centerline in the body frame, $ad_{\xi} = \begin{bmatrix} \widehat{u} & 0 \\ \widehat{v} & \widehat{u} \end{bmatrix}$ is adjoint representation of the spatial twist $\xi$. $W = \begin{bmatrix} m^T, & n^T \end{bmatrix}^T$ is the internal wrench in the body frame with $m, n \in \mathbb{R}^3$ as the internal moment and force in the body frame.

To relate the kinematic equation (3.6) and statics equation (3.7), we can use a constitutive law to relate the internal wrench $W$ and the change of spatial twist $\Delta\xi = \xi - \xi^*$, where $\xi^* = \begin{bmatrix} u^{*T}, & v^{*T} \end{bmatrix}^T$

is the twist in ORS. The change of strains can be caused by the internal forces and moments. For instance, the change of torsional strain $u_z - u_z^*$, where $u_z$ is the third element of $u$, can be caused by the moment about the $z$ axis of body frame. More generally, we have the following constitutive law:

$$W = K\Delta\xi \tag{3.8}$$

where

$$K = \begin{bmatrix} K_{bt} & 0 \\ 0 & K_{se} \end{bmatrix}$$

$K_{bt} = \mathbf{diag}[EI, EI, GJ]$ is the diagonal stiffness matrix for bending and torsion.
$K_{se} = \mathbf{diag}[GA_t, GA_t, EA_t]$ is the diagonal stiffness matrix for shear and extension. $E$ and $G$ are the longitudinal Young's modulus and shear modulus for the twisted fiber, respectively. $A_t$ is the cross section area of the twisted fiber, $I = I_x = I_y = \pi r_t^4/4$ is the second moment of area, and $J = I_x + I_y$ is the polar moment of inertia of the twisted fiber's cross section about its centroid. A detailed derivation for Eq. (3.8) is in Subsection 3.5.1

Eqs. (3.6)-(3.8) establish the kinetostatics of a TCA together with boundary conditions (the external wrench, e.g., a weight hanging at the TCA's end), creating a boundary value problem (BVP) that can be numerically solved. The actuation of the TCA is realized by replacing $u^*$ in Eq. (3.8) with $u^{\mathsf{h}}$ that can be calculated with the increase of the temperature $T$ (Sec. 3.2.3). Detailed numerical implementations will be presented in Sec. 3.4.2. An animation of TCA simulation can be found in our supporting video. The detailed derivation, source code, and supporting video are summarized online at https://jiefengsun.github.io/tca-tro.html

### 3.2.2 Temperature and Strain Dependent Moduli

The moduli ($E$ and $G$) of a twisted fiber vary with the temperature and external loads. If such variations are not modeled, we cannot simulate a TCA's response accurately, especially when external loads are large and the temperature is high. To model such variations, we first calculate the moduli at room temperature based on yarn mechanics, and then incorporate the influence of temperature and load.

Moduli of a twisted fiber depend on three parameters of the twisted fiber: the pitch angle $\alpha_t$, the volume friction $V_f$, the yarn's (monofilament fiber's) tensile modulus $E_f$ [92]:

$$E = \frac{3V_f E_f}{4} \frac{(1+\cos^2\alpha_t)}{1+\cos\alpha_t+\cos^2\alpha_t} \tag{3.9}$$

$$\begin{aligned} G =& E_f V_f / \bigg( \frac{\pi(1-\cos\alpha_t)\sin\alpha_t^3}{6(\alpha_t/2-1/4\sin(2\alpha_t))^2} \\ &+ \frac{8\sin^3\alpha_t}{3\pi(1-\cos\alpha_t)(\cos\alpha_t+1)^2} + \frac{\pi(4-3\cos\alpha_t-\cos^3\alpha_t)}{6(\alpha_t/2-1/4\sin(2\alpha_t))(\cos\alpha_t+1)} \bigg) \end{aligned} \tag{3.10}$$

Among these three parameters, $\alpha_t$ and $V_f$ can be considered as constants after the annealing process, and they can be experimentally obtained. For $\alpha_t$, we can directly obtain it from microscopic photos. For $V_f$, we obtain it indirectly by using Eq. (3.9) with the values of $E$ and $E_f$ at room temperature. $E$ at room temperature is measured to be 1.2 GPa by stretching an annealed twisted fiber. $E_f$ at room temperature is directly chosen to be $E_{f0} = 3.9$ GPa, which is the Young's modulus of Nylon 6,6. With $E$ and $E_f$ at room temperature, we solve $V_f = 0.35$ using Eq. (3.9).

$E_f$ varies with both external loads and temperature, especially when the load and temperature are large [37,93]. In our previous work [34], we have considered how $E_f$ will vary with temperature alone: $E_f$ decreases by 0.0011 GPa per Celsius degree. In this work, we also consider the influence of the external load by using a second-order polynomial ($\lambda = \mu_2\tau^2 + \mu_1\tau + \mu_0$). Therefore, we have

$$E_f = E_{f0} - 0.0011\Delta T(\mu_2\tau^2 + \mu_1\tau + \mu_0) \tag{3.11}$$

where $\Delta T = T - T_0$ is the change of temperature, $\tau = \frac{F_e r}{GJ}$ is the torsional strain caused by an external force $F_e$ along the TCA as shown in Fig. 3.3(a). Since we don't know the exact $G$ before we calculate $\tau$, we take the value of $G$ at room temperature $G_0 = 0.22$ GPa to calculate $\tau$ for a specific load. The coefficients for $\lambda$, $\mu_2 = 3.24 \times 10^{-4}, \mu_1 = -0.027$, and $\mu_0 = 1$, are fitted using the displacement-force relationship at high temperature and high load condition (see Subsection 3.5.2 for more details).

With Eqs. (3.9)-(3.11), $E$ and $G$ can be expressed in terms of the temperature and an external force. $G$ is used as an example to illustrate how the modulus will change. We consider the case when we hang a weight at the end of a TCA. We can plot $G$ with respect to temperature and the weight in Fig. 3.4. $G$ will decrease more than 13% when the temperature and weight both reach a large magnitude. Although we plot $G$ with respect to weights for more intuitive illustrations, it is more general for the moduli to depend on the torsional strain ($\tau$) than the external force produced by hanging weights, since even the same hanging weight at the ends of two TCAs made of the same twisted fiber will cause different torsional strains on the twisted fiber if the two TCAs have different outside diameters.

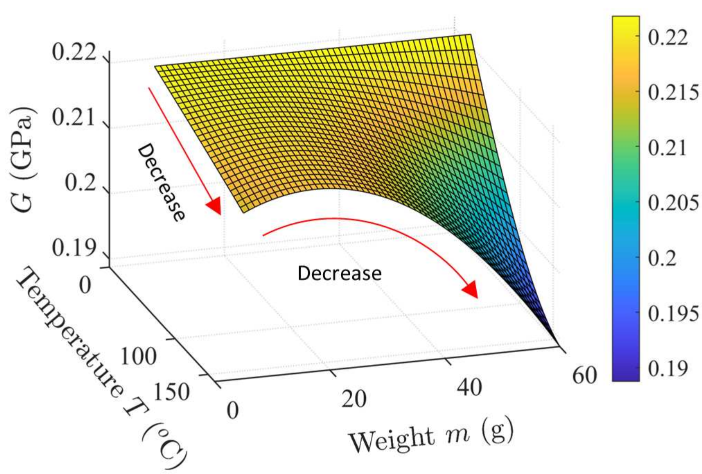


**Figure 3.4:** The change of the shear modulus $G$ with respect to the temperature and hanging weight for a free-stroke TCA fabricated as in Sec. 3.4.1.

### 3.2.3 Reference Strain and Boundary Conditions

To numerically implement the model, we need to obtain the reference strains and the boundary conditions for the two ends. Recall that we define two types of reference states: 1) a TCA's original reference state (ORS) when no load and no heat is applied; 2) a heated reference state (HRS) when the heat is applied but no load is applied. We use a superscript $*$ and $\mathsf{h}$ to represent ORS and HRS, respectively. For instance, a TCA may initially have an ORS strain $\xi^*$ when no load and heat is applied, but when the heat is applied, $\xi^*$ will be shifted to an HRS strain $\xi^{\mathsf{h}}$.

Here we use a right-handed TCA as an example to obtain the references, and the derivation for a conical TCA is discussed in Subsection 3.5.3. The derivations are also implemented using Malab Symbolic Toolbox, and the source code can be found at https://github.com/jiefengsun/TCA-TRO. The TCA is hanged by fixing its top, and the global frame's origin $O$ is established at the top of the TCA as shown in Fig. 3.3(a). $Z$ direction is along the axis of the TCA. In the following, we will obtain the relative position and orientation for a cross section in the twisted fiber with respect to the global frame (i.e., frame $oxyz$ with respect to frame $OXYZ$ in Fig. 3.3(b)).

The position vector $p^*(s)$ in ORS can be parameterized using arc-length as

$$p^*(s) = \left[ r^* \cos\phi, r^* \sin\phi, s\sin(\alpha^*) \right]^T \tag{3.12}$$

where $\phi = 2\pi n = s\cos\alpha^*/r^*$ is the coiling angle, $n$ the number of coils, $r^*$ the radius of the coil, and $\alpha^*$ the pitch angle in ORS.

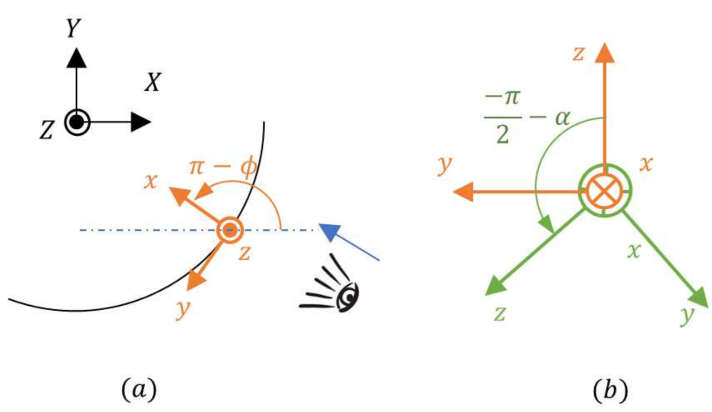


**Figure 3.5:** Steps to obtain the rotational matrix $R^*(s)$. (a) The top view for the first step rotating around $z$ for $\pi - \phi$. (b) The view for the second step looked from the arrow direction in (a). Rotate around $x$ for $-\frac{\pi}{2} - \alpha^*$ with respect to the body frame. Signs of the rotation angles are determined using the right hand rule.

The rotation matrix $R^*(s)$ in ORS can be also parameterized using $s$ through consecutive frame transformations as shown in Fig. 3.5.

$$R^*(s) = R_z(\pi - \phi) R_x(-\frac{\pi}{2} - \alpha^*) \tag{3.13}$$

where $R_x, R_z$ are respectively basic rotation matrices that rotate frames about the $x$, $z$ axis by an angle using the right-hand rule. The colored item in Eq. (3.13) is corresponding to the body frame in the same color after rotation in Fig. 3.5. Note that post multiplication is used (rotation with respect to the current body frame) and the final $z$ orientation of the body frame is always along the tangent direction of the twisted fiber. A 3D animation of the body frame moving along a helix is shown in the supporting video.

With $p^*(s)$ and $R^*(s)$, we can then obtain the ORS strain $u^*$ and $v^*$ from Eq. (3.6)

$$\begin{aligned} u^*(s) &= (R^{*T} R^{*\prime})^\vee = \left[0, \kappa^*, \tau^*\right]^T \\ v^* &= R^{*T} p^{*\prime} = [0, 0, 1]^T \end{aligned} \tag{3.14}$$

where $\kappa^* = \cos^2 \alpha^* / r^*$, $\tau^* = \sin \alpha^* \cos \alpha^* / r^*$ are the geometric curvature and torsion of the helix. Note that $v^*$ does not vary with geometry parameters.

When heated, the twisted fiber untwists, the ORS strain is shifted to the HRS strain by adding the influence of untwisting to the geometric torsion

$$u^{\mathsf{h}}(s) = \left[0, \kappa^*, \tau^* + \Delta\bar{\theta}^{\mathsf{h}}\right]^T, \ v^{\mathsf{h}} = v^* \tag{3.15}$$

Note that $\Delta\bar{\theta}^{\mathsf{h}}$ changes with respect to temperature $T$; therefore, $u^{\mathsf{h}}$ is a function of $T$. In the simulation, $u^{\mathsf{h}}$ is iteratively updated based on $T$ to incorporate the thermal actuation.

After solving the reference strains, we can solve the boundary conditions. We first derive the boundary condition for the fixed end of a TCA, whose centerline is along the global $Z$ axis. We will then discuss the boundary conditions for the free end with an external load applied to it.

The boundary condition for the fixed end ($s = 0$) can be solved from Eqs. (3.12) and (3.13)

$$
\begin{aligned}
p_0 &= p^*(0) = [r^*, 0, 0]^T \\
R_0 &= R^*(0) = \begin{bmatrix} -1 & 0 & 0 \\ 0 & \sin(\alpha^*) & -\cos(\alpha^*) \\ 0 & -\cos(\alpha^*) & -\sin(\alpha^*) \end{bmatrix}
\end{aligned}
\tag{3.16}
$$

The boundary condition for the free end with an external wrench $W_e^g$ (superscript '$g$' means it is in the global frame) at $s = l_t$ is

$$W(l_t) = Ad_{g(l_t)}^T W_e^g \tag{3.17}$$

where

$$Ad_g = \begin{bmatrix} R & 0 \\ \widehat{p}R & R \end{bmatrix}$$

is the adjoint representation for the Lie group element $g$, $Ad_g^T$ will transform $W_e^g$ to the body frame. When a weight $m$ is hanged at the TCA's end, $W_e^g = [0, 0, 0, 0, 0, -mg_r]^T$ with $g_r = 9.81$ m/s$^2$ the gravitational constant.

### 3.2.4 Modeling TCA Dynamics using Cosserat Rod Kinetostatic Model

TCAs are generally used for actuation (e.g., lifting weights). In this case, we can simplify its dynamics model by ignoring the inertial force of a TCA since the hanging weight is usually over 1000 times heavier than a TCA's weight. In other words, we can establish a simplified dynamics model based on the Cosserat rod kinetostatics. Such a simplification can reduce the Cosserat rod dynamics, which is a system of partial differential equations (PDEs) with respect to time and space, to an ODE with respect only to time:

$$m\ddot{x} + b_t\dot{x} + f_{rod}(x, T(t)) = 0 \tag{3.18}$$

where $x$ is the displacement of the weight $m$ from the loaded equilibrium, the $\dot{}$ is the derivative with respect to time, $b_t$ is the damping coefficient of the TCA, $f_{rod}(x, T(t))$ is the TCA's internal force calculated from the Cosserat rod model for a displacement $x$ and temperature $T(t)$.

## 3.3 Simplification and Special Cases

In this section, we show that existing models (e.g., Love's equation and CST) for the kinetostatics of TCAs can be considered as special cases of the more general Cosserat rod model.

### 3.3.1 TCA Kinetostatic Modeling with Love's Equation

Love's equation [42] establishes the kinematic relationship between a helix's pitch angle and its precursor fiber's torsion change, which has been proposed for modeling TCAs [3, 36]. But the equation is a special case of Cosserat rod model in terms of a helix. In fact, a Cosserat rod model can be reduced to a Kirchhoff rod model by ignoring the shear and extension strains, and then the Kirchhoff rod model can be further reduced to Love's equation. Without shear and extension, a helical TCA will have constant geometric curvature and torsion anywhere along the centerline (i.e., $u$ does not depend on $s$) if the external force is along the centerline. Therefore, if we denote the third element of $u^{\mathsf{h}}(s)$ in Eq. (3.15) as $\tau^{\mathsf{h}}$, then we have $\tau^{\mathsf{h}} = \tau^* + \Delta\bar{\theta}^{\mathsf{h}}$ for any point of the helix. This can be rearranged to

$$\Delta\bar{\theta}^{\mathsf{h}} = \tau^{\mathsf{h}} - \tau^* = \frac{\sin\alpha^{\mathsf{h}}\cos\alpha^{\mathsf{h}}}{r^{\mathsf{h}}} - \frac{\sin\alpha^*\cos\alpha^*}{r^*} \tag{3.19}$$

which is the same form of Love's equation as in Ref. [1, 3, 36].

Previous works only use Love's equation for the coil kinematic model and need to rely on other coil static models (e.g., CST or a constant stiffness coefficient) [3, 36] to complete a TCA model (Table 1.1). Here, we will directly use Love's equation to establish the statics model for TCAs.

When an external wrench $W_e^g$ in the global frame is applied to a TCA and the wrench's axis coincides with the TCA's axis as shown in Fig. 3.3(a), the corresponding internal wrench $W$ in the body frame will not vary with respect to $s$ due to the symmetry of the geometry around the axis of $W_e^g$. Therefore, $W$ at any $s$ is equal to the value at boundary, which can be calculated using the boundary condition Eq. (3.17)

$$W = W(0) = Ad_{g_0}^T W_e^g \tag{3.20}$$

where

$$Ad_{g_0} = \begin{bmatrix} R_0 & 0 \\ \widehat{p}_0 R_0 & R_0 \end{bmatrix} \tag{3.21}$$

$R_0$ and $p_0$ are from Eq. (3.16), $W_e^g = [M_e^T, F_e^T]^T$, $F_e$ and $M_e$ are respectively the external force and moment vectors, $F_e = [0,0,F_e]^T$, $M_e = [0,0,M_e]^T$ with $F_e$ and $M_e$ respectively the force and moment applied at the free end. For a hanging weight, $F_e = -mg_r$ and $M_e = 0$. Note that there is no need to distinguish the boundaries at the two ends, i.e., $Ad_{g_0} = Ad_{g(l_t)}$.

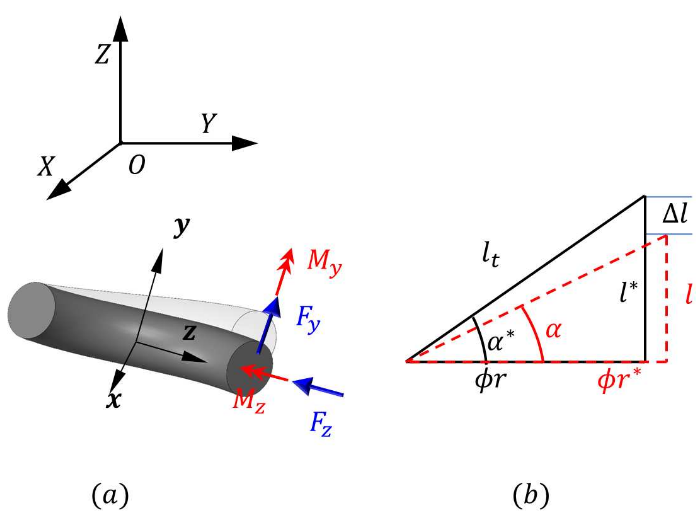


**Figure 3.6:** (a) The wrench in the body frame ($F_x$ and $M_x$ are not shown since they are zero). (b) The geometric relation of a helical TCA before and after deformation.

Therefore, $W = \left[m^T, n^T\right]^T$ with $m = [M_x, M_y, M_z]^T$ and $n = [F_x, F_y, F_z]^T$ as shown in Fig. 3.6(a) can be expressed as:

$$\begin{aligned}
&M_x = 0 \\
&M_y = F_e r \sin\alpha - M_e \cos\alpha \\
&M_z = -F_e r \cos\alpha - M_e \sin\alpha \\
&F_x = 0,\, F_y = -F_e \cos\alpha,\, F_z = -F_e \sin\alpha
\end{aligned} \tag{3.22}$$

After ignoring shear and extension, the constitutive law of the Cosserat rod Eq. (3.8) can be reduced as $m = K_{bt}(u - u^{\mathsf{h}})$, which can be decomposed to

$$\Delta\kappa = \frac{M_y}{EI},\, \Delta\tau = \frac{M_z}{GJ} \tag{3.23}$$

where $\Delta\kappa = \kappa - \kappa^{\mathsf{h}} = \cos^2\alpha/r - \cos^2\alpha^{\mathsf{h}}/r^{\mathsf{h}}$, and $\Delta\tau = \tau - \tau^{\mathsf{h}} = \sin\alpha\cos\alpha/r - \sin\alpha^{\mathsf{h}}\cos\alpha^{\mathsf{h}}/r^{\mathsf{h}}$

Since a TCA's unwinding at the end is negligible, the total coiling angle is a constant ($\phi$ does not change as in Fig. 3.6(b)):

$$\frac{\phi}{l_t} = \frac{\cos\alpha}{r} = \frac{\cos\alpha^{\mathsf{h}}}{r^{\mathsf{h}}} = \frac{\cos\alpha^*}{r^*} \tag{3.24}$$

Substituting $M_z$ and $M_y$ from Eq. (3.22) into Eq. (3.23) and using Eq. (3.24), we have

$$\begin{aligned}
&F_e + \frac{GJ\cos^2\alpha^*}{r^{*2}}\left(\sin\alpha - \sin\alpha^{\mathsf{h}}\right) \\
&-\frac{EI\tan\alpha\cos^2\alpha^*}{r^{*2}}\left(\cos\alpha - \cos\alpha^{\mathsf{h}}\right) = 0
\end{aligned} \tag{3.25}$$

We also have the following relationship for a TCA's length as shown in Fig. 3.6(b)

$$l = l_t \sin\alpha \tag{3.26}$$

Using Eqs. (3.19), (3.25), (3.26) and simplifying, we can get the displacement $\Delta l = l^* - l$ shown in Fig. 3.6(b) as a function of external force $F_e$ and the unit untwist $\Delta\bar{\theta}^{\mathrm{h}}$ due to heat

$$\Delta l = \frac{1}{K_{lv}} F_e - A_{lv} \Delta\bar{\theta}^{\mathrm{h}} \tag{3.27}$$

where

$$\begin{aligned}
\frac{1}{K_{lv}} &= \frac{l_t (r^{\mathrm{h}})^2}{GJ\cos^2\alpha^{\mathrm{h}} + EI\tan\alpha \frac{\cos\alpha^{\mathrm{h}} - \cos\alpha}{\sin\alpha - \sin\alpha^{\mathrm{h}}}} \\
A_{lv} &= \frac{l_t r^*}{\cos\alpha^*}
\end{aligned}$$

### 3.3.2 TCA Kinetostatic Modeling with Infinitesimal Strain Theory

CST has been widely used to model a TCA's kinetostatics [29, 34, 35, 37], but the results from CST can be considered as a linearized case of the Cosserat rod model by loosening the geometry exactness using 'small deformation' approximation (Infinitesimal strain theory) – assuming the deformed shape is close to the initial shape.

The actuation is considered as an external force, $M_a = \Delta\bar{\theta}^{\mathrm{h}} GJ$ applied along $z$ axis; therefore, $M_z = -F_e r\cos\alpha - M_e \sin\alpha + M_a$ in $W$ (Eq. (3.22)). Inverse the constitutive law Eq. (3.8) to get $\Delta\xi = K^{-1}W$, which is the strain in the body frame, and it can be transformed to the global frame due to the small deformation assumption.

$$\Delta\xi^g = Ad_{g_0}\Delta\xi \tag{3.28}$$

The sixth element of $\Delta\xi^g$ is $\Delta\xi^g_6$, which represents the TCA's linear strain along the global $Z$ axis. Integrating the strain over the arc-length results in the TCA's linear displacement. Since $\Delta\xi^g_6$ is independent of the arc-length $s$, we have a form similar to Eq. (3.27) but with different coefficients

$$\Delta l = l_t \Delta\xi^g_6 = \frac{1}{K_{cst}} F_e - A_{cst} \Delta\bar{\theta}^{\mathrm{h}} \tag{3.29}$$

where

$$\frac{1}{K_{cst}} = l_t \left( \frac{r^2 \cos^2 \alpha}{GJ} + \frac{r^2 \sin^2 \alpha}{EI} + \frac{\cos^2 \alpha}{GA_t} + \frac{\sin^2 \alpha}{EA_t} \right)$$
$$A_{cst} = l_t r \cos \alpha$$

Note that based on the small deformation assumption, all the variables are close to their values of the reference states, for example, $\alpha \approx \alpha^* \approx \alpha^{\mathsf{h}}$. Although we don't distinguish them in Eq. (3.29), the results' accuracy could be improved by iteratively updating the variables based on the previous step or using an implicit solver, which can be observed in our supporting code.

Eq. (3.29) is the same as the results from CST, which is discussed in Subsection 3.5.3, and it can be used to calculate a TCA's deformation when $F_e$ and $\Delta\bar{\theta}^{\mathsf{h}}$ are known. From Eqs. (3.27) and (3.29), it is clear that a TCA's deformation comes from two sources: the external load $F_e$ and unit untwist $\Delta\bar{\theta}^{\mathsf{h}}$ resulted from thermal expansion.

### 3.3.3 Dynamics for Love's and CST Methods

Although Eqs. (3.27) and (3.29) are convenient for calculating the static deformation, we rearrange them to an equilibrium of forces to facilitate the extension to dynamics

$$F_e - K_c(\Delta l + A\Delta\bar{\theta}^{\mathsf{h}}) = 0 \tag{3.30}$$

where $K_c$ can be $K_{lv}$ or $K_{cst}$, and $A$ can be $A_{lv}$ or $A_{cst}$. We call $A$ the coil kinematic coefficient and $K_c$ the coil stiffness coefficient.

For the most common scenario when a weight is hanged at the end of a TCA, the dynamics model can be easily extended from a statics model by including damping force and inertial force ($F_e = -(m\ddot{x} + b_t\dot{x} + mg_r)$)

$$m\ddot{x} + b_t\dot{x} + K_cA\Delta\bar{\theta}^{\mathsf{h}} = 0 \tag{3.31}$$

Note that $x$ is the displacement of the weight from the loaded equilibrium, and we use $\Delta l K_c = -mg_r$, when $\Delta l$ is the displacement from the natural equilibrium (no load) to the loaded equilibrium.

## 3.4 Simulation and Experimental Results

In this section, we experimentally validate our model and compare its accuracy with existing models under different loading scenarios for the self-coiled and free-stroke TCAs. We also demonstrate our model can model conical TCAs.

### 3.4.1 Fabrication of TCAs

We fabricate three types of TCAs: a self-coiled TCA, a free-stroke TCA, and a conical TCA. In the following, we briefly describe the fabrication process.

The three types of TCAs have the same twisted fibers. Since it is made from threads, we will use twisted threads in the rest of this section. To fabricate the twisted thread, we hang a weight of 240 g at the end of a sewing thread (Shieldex Trading, 235/36 dtex 4 ply HC+B) and twist it until reaching the verge of self-coiling by inserting unit twist 4.71 rad/mm. A weight heavier than 240 g may easily break the threads, and a lighter weight will not allow for enough twisting of the threads. The unit twist in the twisted threads for the three TCAs are the same, and the parameters of the twisted threads are listed in Table 3.1.

The self-coiled TCA is fabricated by continuously inserting twisting to the twisted thread. To make sure the prescribed amount of twist is inserted in the twisted thread, we manually trigger the self-coiling process by reducing the hanging weight from 240 g to 210 g and manually disturbing the thread. After the first coil is triggered, we continuously insert twisting to the thread to finish the coiling process.

The free-stroke TCA Type 2-180 is fabricated by coiling the twisted thread in the groove of a helical mandrel. The helical mandrel is fabricated by wrapping a thin copper wire on a mandrel core (thick copper wire) in a helical shape with a pitch angle of 22.42° as shown in Fig. 3.7(a). A

**Table 3.1:** The parameters of the twister fiber for all the TCAs.

| Item | Unit | Value |
|---|---|---|
| Inserted torsion for annealing $\theta^*$ | rad/mm | 4.71 |
| Twisted fiber radius $r_t^*$ | mm | 0.21 |
| Twisted fiber pitch angle $\alpha_t$ | $\circ$ | 40 |
| Volume Friction | | 0.35 |
| Specific heat $c_p$ | J/(Kg K) | 1267 |
| Density $\rho$ | kg/m$^3$ | 1300 |
| Convection Coefficient $h$ | W/(m$^2$ K) | 23 |
| Ambient Temperature $T_\infty = T_0$ | $^\circ$ C | 25 |
| Longitudinal Young's modulus $E$ | GPa | Eq. (3.9) |
| Longitudinal shear modulus $G$ | GPa | Eq. (3.10) |
| Thermal actuation | rad/mm | Eq. (3.4) |

**Table 3.2:** The parameters of the self-coiled, free-stroke, and conical TCA.

| Item | Unit | Self-coiled | Free-stroke | Conical |
|---|---|---|---|---|
| Precursor fiber length | mm | 218 | 218 | 181 |
| Twisted fiber length $l_t$ | mm | 175 | 175 | 145 |
| TCA made length | mm | 56 | 66.75 | 57 |
| TCA natural length $l^*$ | mm | 56 | 45 | 55 |
| Number of coils $n$ | | 120 | 63 | 5.3 |
| Coil radius $r^*$ | mm | 0.227 | 0.408 | NC |
| Pitch angle $\alpha^*$ | $\circ$ | 18.66 | 22.42 | NC |

NC: Non-constant

customized machine is used, and the detailed fabrication process of free-stroke TCAs can be found in Chapter 2 and Ref. [86].

The conical TCA is fabricated by coiling the twisted thread on a conical spiral mandrel (Fig. 3.7(b)) made of heat-resistant material (EpoxAcast 670 HT, Smooth-On, Inc.). The conical mandrel is a copy of our 3D printed conical mandrel (Objet30, Stratasys Ltd.), because the 3D printed part is not heat resistant. The copying procedure is: 1) fabricate a mold using the 3D printed part and silicone rubber (Mold Max 29NV, Smooth-On, Inc.); 2) cast the EpoxAcast 670 HT to the mold; 3) demold the mandrel and perform a heat treatment before use. The conical spiral groove in the conical mandrel has a constant pitch $p_c = 10.6$ mm and a cone angle 12° that results in $a = 2\pi/p_c$ and $b = \tan(12\pi/360)$ for the conical spiral's curve equation Eq. (3.36).

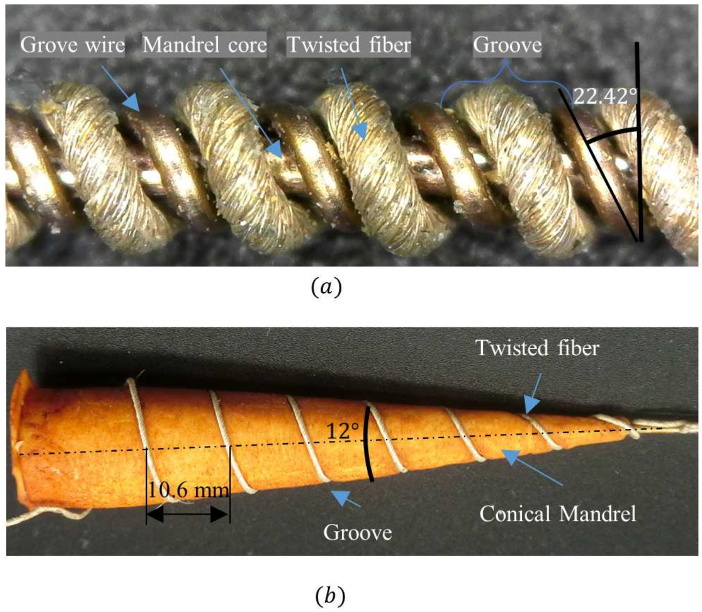


**Figure 3.7:** (a) The helical mandrel with the coiled free-stroke TCA. (b) The conical mandrel with the conical TCA.

The three types of TCAs' ends are constrained and annealed in an oven (10GCE, Quincy Lab, accuracy 0.5°C) for 2.5 hours at a temperature of 185°C, which will stabilize the shapes. Finally, the free-stroke TCA and conical TCA are removed from the mandrels. The parameters of the three TCAs are listed in Table 3.2.

### 3.4.2 Numerical Implementations for the Cosserat Rod Model

#### Quaternions as Rotation

Spatial derivative of rotations ($R'$) is integrated using non-unit quaternions to avoid truncation error and ensure $R \in SO(3)$ [94]. This method allows any high-order integration scheme or general-purpose ODE solver to efficiently integrate rotations over a long spatial range while eliminating singularities and maintaining the structure of SO(3). The basic idea is to represent $R$ using a quaternion $h$, and represent $R'$ using $h'$ and $u$, then the integration of $R'$ can be performed by integrating $h'$.

A quaternion $h = h_0 + h_1 i + h_2 j + h_3 k$, where $i, j$, and $k$ are called quaternionic units. $h$ can be written in a vector form in $\mathbb{R}^4$: $h = [h_0, h_1, h_2, h_3]^T$. Then we can have the derivative of $h$ with respect to $s$ as [94]

$$h' = \frac{1}{2}\begin{bmatrix} 0 & -u_x & -u_y & -u_z \\ u_x & 0 & u_z & -u_y \\ u_y & -u_z & 0 & u_z \\ u_z & u_y & -u_x & 0 \end{bmatrix}\begin{bmatrix} h_0 \\ h_1 \\ h_2 \\ h_3 \end{bmatrix} \tag{3.32}$$

where $u_x, u_y$ and $u_z$ are elements of $u$. We can also calculate rotational matrix $R$ using $h$

$$\begin{aligned} R(h) = I + \\ \frac{2}{h^T h}\begin{bmatrix} -h_2^2 - h_3^2 & h_1 h_2 - h_3 h_0 & h_1 h_3 + h_2 h_0 \\ h_1 h_2 + h_3 h_0 & -h_1^2 - h_3^2 & h_2 h_3 - h_1 h_0 \\ h_1 h_3 - h_2 h_0 & h_2 h_3 + h_1 h_0 & -h_1^2 - h_2^2 \end{bmatrix} \end{aligned} \tag{3.33}$$

It is also useful to calculate $h$ from a rotational matrix $R$ to obtain the initial condition. A robust numerical scheme [95] $quat2rotm$ in Matlab is used to find $h_0 = quat2rotm(R_0)$.

**Finite Difference Solver**

Eqs. (3.6)-(3.8) together with boundary conditions Eqs. (3.16) and (3.17) represent a boundary value problem (BVP) that can be solved by two typical methods: shooting methods or finite difference methods. A shooting method iteratively guesses the unknown boundary values for the fixed end (initial boundary) and evaluates the boundary values at the other end after numerical integration, which is fast for certain problems [63]. However, we found that the shooting method couldn't provide good initial guesses for a complicated shape such as TCAs with many coils. Therefore, we use a finite difference solver in Matlab $bvp5c$ [96].

**Simulation Process of TCA Statics**

For a simple case where a weight is hanged at the end of a TCA and then lifted up, the simulation process is shown in Algorithm 1.

---

**Algorithm 1:** TCA statics with a hanging weight.

---

**Input:** Weight $m$ and maximum temperature $T_{max}$
Initialize geometric parameters and loading;
Setup boundary conditions $R_0, p_0, W(l_t)$;
Solve rod ODEs for loaded equilibrium before heating;
**for** $T = T_0 \rightarrow T_{max}$ **do**
  Obtain unit untwists $\Delta\bar{\theta}^{\mathrm{h}}$ (Eq. (3.4));
  Update the HRS strain $\xi^{\mathrm{h}}$ (Eq. (3.15));
  Update moduli $E$ and $G$ (Eqs. (3.9)-(3.11));
  Solve rod BVP for the actuation;
  Extract the displacement $x$;
  Visualization;
**end**

---

The program has two inputs: the maximum temperature and the weight. It begins with declarations of the various physical parameters. Then, it solves the static equilibrium of the TCA with weight at the end before increasing temperature. In the main loop, each step, it updates the corresponding unit untwist $\Delta\bar{\theta}$ (Eq. (3.4)), the HRS strain (Eq. (3.15)), and material modulus (Eqs. (3.9) - (3.11)) according to the temperature increase. After that, it solves the BVP (Eqs. (3.6) - (3.8), (3.16) and (3.17) ) with visualization of results.

**Simulation Process of TCA Dynamics**

We solve Eq. (3.18) using the finite difference method combined with the shooting method. The shooting method first guesses and then solves the internal force of the rod $f_{rod,i}$ for time step $i$, that minimize the residual $res_i = |f_{rod,i} - m\ddot{x}_i - b\dot{x}_i|$, using central difference schemes [97]

$$\ddot{x}_i = \frac{x_{i+1} - 2x_i + x_{i-1}}{\Delta t^2}, \dot{x}_i = \frac{x_{i+1} - x_{i-1}}{2\Delta t}$$

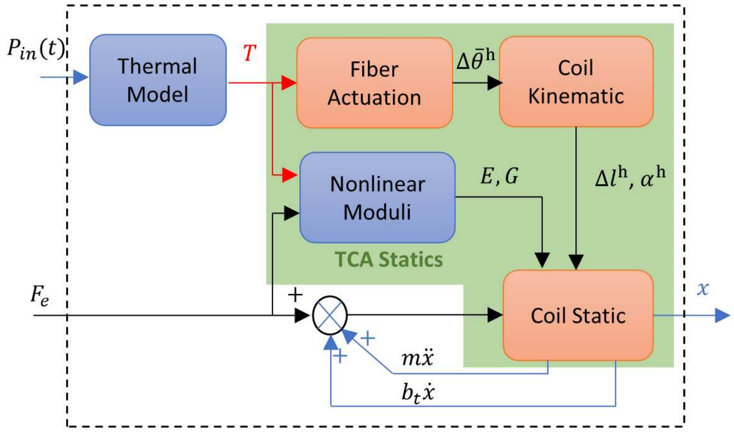


**Figure 3.8:** The schematic of the TCA's dynamics model. The green shaded area is a schematic of the static model with $T$ and $F_e$ as the input, and $\Delta l$ as output.

where $\Delta t$ is the time step size, $i \in \{1, \ldots, N_s\}$ is index of the time step, and $N_s$ is the total number of time steps. The displacement $x_i$ is solved as an intermediate variable.

### 3.4.3 Numerical Schemes for Love's and CST Methods

The numerical scheme for the two methods is the same. A general statics simulation scheme is boxed in the green area in Fig. 3.8. First, a temperature $T$ is input into the fiber actuation model to obtain the unit untwisting $\Delta\bar{\theta}^{\mathrm{h}}$ of the twisted fiber, and then $\Delta\bar{\theta}^{\mathrm{h}}$ is input into the coil kinematic model to obtain the displacement and pitch angle due to actuation. Given an external force $F_e$, the final displacement $\Delta l$ can be calculated from the coil static model by solving the equilibrium equation with the nonlinear moduli ($E$ and $G$) influenced by the temperature.

A general dynamics simulation scheme is shown in Fig. 3.8 as boxed by black dashed lines. The model takes time-varying electric power $P_{in}(t)$ as the input to solve the temperature $T$ using the thermal model. Then $T$ is input into the static model. In addition to a static external force $F_e$, time-varying load such as inertial force ($m\ddot{x}$) and damping force ($b_t\dot{x}$) are implicitly calculated using the same method as the rod dynamics.

## 3.4.4 Kinetostatics and Dynamics of Self-coiled and Free-stroke TCAs

To compare the accuracy of various methods, three cases of simulations and experiments are conducted for the self-coiled TCA and the free-stroke TCA.

### Considerations on the Experiments and Simulation

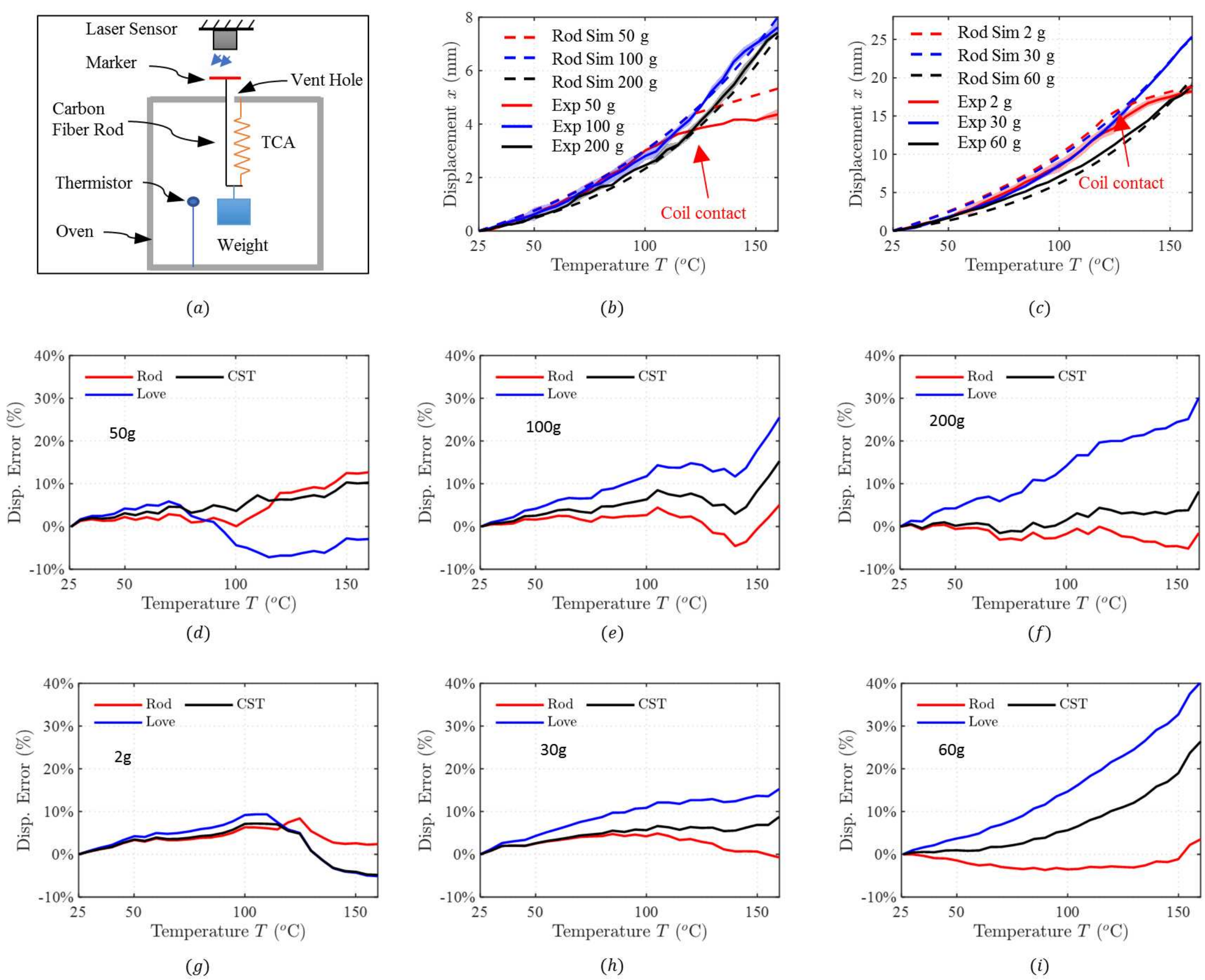


**Figure 3.9:** Case 1: kinetostatics with a hanging weight. (a) Experimental setup. (b) The comparison between simulation results using the rod model and experimental results for the self-coiled TCA. (c) The comparison between simulation results using the rod model and experimental results for free-stroke TCA. (d), (e), and (f): The normalized displacement error of the simulations for the self-coiled TCA using the Cosserat rod model, Love's method and CST method respectively for 50 g, 100 g, and 200 g. (g), (h), and (i): The normalized displacement error of the simulations for the free-stroke TCA using the Cosserat rod model, Love's method and CST method respectively for 2 g, 30 g, and 60 g.

Due to the viscoelastic effect of the nylon 6,6 material, a TCA will gradually elongate to another length corresponding to the load applied to it after a certain time or through a few heating cycles known as creep [74, 98]. 'Lonely stroke' is used to describe the phenomenon that a TCA's displacement will be influenced by its time history of loading [99].

While the equilibrium length at a certain time cannot be predicted without considering viscoelasticity, most applications of TCAs only consider the actuation displacement of the TCAs starting from an equilibrium length, which can be easily measured in applications, especially when closed-loop control is required. In this work, we conduct experiments starting at such an equilibrium state as if the TCA has already crept to the length corresponding to the weight. We also use the reference state corresponding to the length as the reference for simulation.

A helical TCA will stop contraction when neighboring coils contact each other. Therefore, its stroke is mainly limited by coil contact, especially when the load is small. For some applications, prediction of contact is preferred. As a general modeling framework, we consider the coil contact by using a Sigmoid (Logistic) function to reduce $\Delta\bar{\theta}^{\mathsf{h}}$, once $\alpha < \alpha_{min}$, let $\Delta\bar{\theta}^{\mathsf{h}} = \Delta\bar{\theta}^{\mathsf{h}} + 20e^{50(\alpha_{min}-\alpha)}$, where $\alpha_{min}$ is calculated by measuring the minimum length of a TCA.

We study three most common application scenarios for helical TCAs: 1) kinetostatics with a hanging-weight, 2) explicitly known varying load, and 3) dynamics with a hanging-weight. Each type of experiment is repeated three times and the mean value and standard deviation are respectively plotted as a solid line and the corresponding shaded area.

### Case 1: Kinetostatics with a Hanging Weight

We first evaluate the kinetostatics when we hang a weight at the end of a TCA by gradually increasing the TCA's temperature. Such an experiment is a common case for TCAs. In fact, most of references in Table 1.1 use this case to verify their models. Our experimental setup is shown in Fig. 3.9(a). The TCA's top is fixed to the inner roof of an oven, and its bottom is connected to a carbon fiber rod, whose top end comes out from the vent hole of the oven. We place a marker at the top of the carbon fiber rod and use a laser displacement sensor (OPT2006, Wenglor sensoric GmbH) to measure the TCA's contraction. The weight of the carbon fiber rod with the marker is negligible (0.2 g). In an experiment, a weight is hanged at the bottom of a TCA: 2 g, 30 g, and 60 g for the free-stroke TCA; 50 g, 100 g, and 200 g for the self-coiled TCA.

In the experiment, the temperature inside the oven slowly increases to 160°C from the room temperature (25°C) in around 14 mins, and the temperature is recorded with a thermistor (EPCOS Inc., B57540G0503F000). Due to the comparable sizes of the TCA and the thermistor and the slow increasing rate of the temperature, the TCA's temperature is approximately the temperature measured by the thermistor. Before an experiment, we place the corresponding weight and conduct a heating cycle (heat up and cool down) using electricity, and wait 3 mins to start an experiment. This process will allow the TCA to quickly creep to a length close to the equilibrium length corresponding to the weight. Comparing with heating a TCA with electricity and measuring the TCA's temperature, conducting experiments in an oven achieves better accuracy by eliminating environmental influence. The slow heating process also provides enough time for the thermistor to respond, and it also eliminates possible dynamic effects (inertial and damping) for the statics.

Figure 3.9(b) and (c) shows the comparison between experimental and simulation results using the rod model for the self-coiled TCA and the free-stroke TCA, respectively. The shaded area and the solid line are respectively the mean value and the standard deviation of three repeated measurements. The maximum standard deviation of all the static experiments for the two TCAs is 1.24 mm.

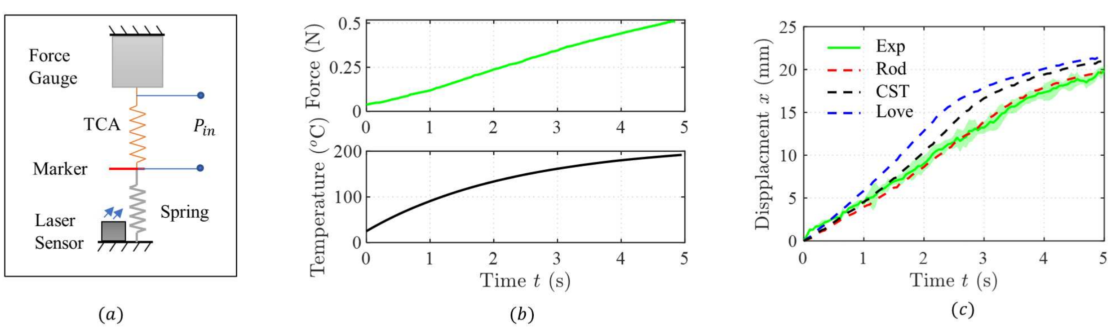


**Figure 3.10:** Case 2: varying load. (a) Experimental setup. (b) The measured force and calculated temperature using the thermal model. (c) The comparison of the experimental results and the simulation results using the three methods.

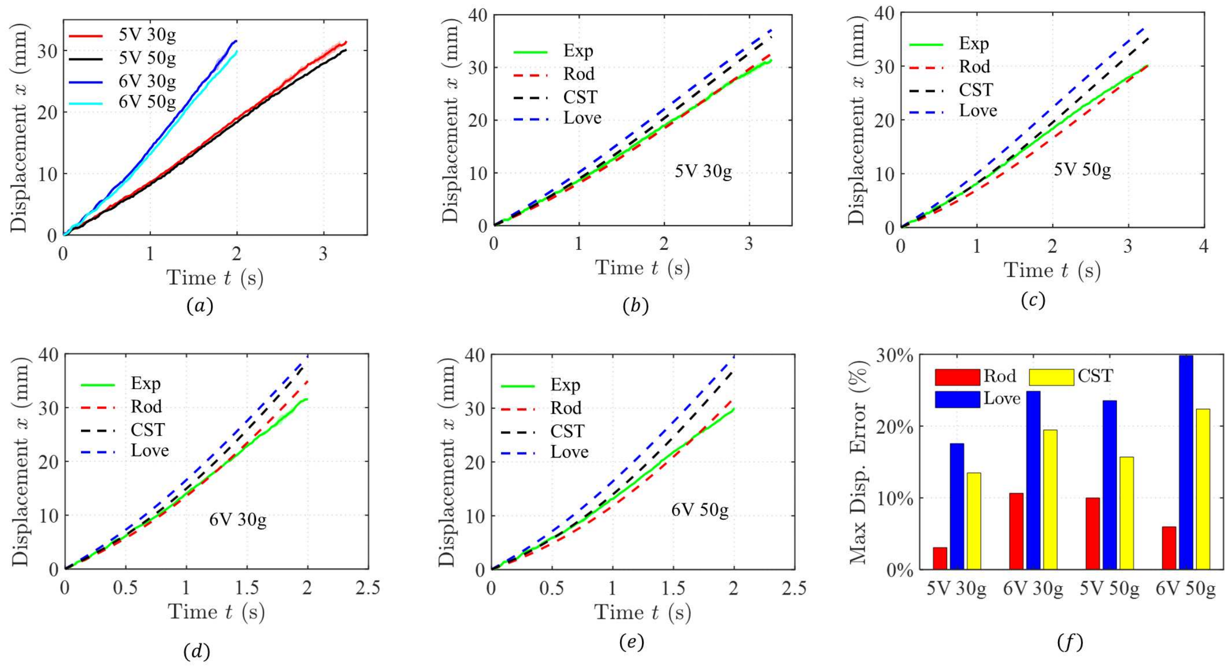

**Figure 3.11:** Case 3: Dynamics with a hanging weight. (a) The experimental results for the four cases. (b)-(e) The experimental and the simulation results for 5V 30g, 5V 50g, 6V 30g, and 6V 50g cases. The shaded area of the green curve represents the standard deviation of three repeated experiments. (f) The maximum displacement error of the four cases for the three methods.

To quantify the accuracy of the three methods, the normalized displacement error (the difference between simulation and experimental results normalized by the maximum displacement of three experiments) for the three methods are calculated and plotted in Fig. 3.9(d), (e), and (f) for the self-coiled TCA with 50 g, 100 g, and 200 g, and in Fig. 3.9(g), (h), and (i) for the free-stroke TCA with 2 g, 30 g, and 60 g. The results indicate that in terms of accuracy: rod model $>$ CST method $>$ Love's method. For all three methods, the errors grow with the increase of the temperature and weight. But the maximum error of the Cosserat rod model is less than 10%, whereas the maximum error for Love's equation can be around 40%. The potential reasons for the better accuracy of CST method than Love's method are 1) the CST method considers all the same four strains (torsion, bending, shear, and extension) as considered in the Cosserat rod model, but Love's methods only consider two strains (torsion and bending). 2) the numerical simulation of the CST method iteratively updates its parameters such as $r$ and $\alpha$. Even though the CST method is based on the infinitesimal strain theory, the numerical iteration improves its accuracy.

**Case 2: Varying Load**

After verifying the accuracy of the kinetostatics modeling, we connect a TCA with a mechanical spring to simulate a varying load when the TCA contracts. The varying load from the spring only depends on the displacement, not on time factors such as velocity or acceleration of the contraction (i.e., no dynamic effects). This case has many applications in TCA-driven robots. A typical case is a soft manipulator driven by embedded TCAs: the force on the TCA increases as the TCA contracts to bend the soft manipulator [27].

As shown in Fig. 3.10(a), one end of the spring is fixed, and its other end is attached to the TCA. The other end of the TCA is connected to a force gauge (M5-12, Mark-10 Inc.) to measure the real-time force during the experiments. To keep the TCA taut, a 0.05 N pretension is applied. The laser displacement sensor is used to record the TCA's displacement by measuring the displacement of a marker placed at the connection point between the TCA and the spring. The TCA is actuated using 5 V voltage, and its power is recorded using a high-side current/voltage sensor (INA 219, Adafruit), which is not a constant due to the change of the TCA's resistance during the actuation. In this experiment, only the free-stroke TCA is used since it can provide a large stroke without significant pretension. The recorded force and the calculated temperature using the thermal model are plotted in Fig. 3.10(b). Using the calculated temperature and the measured force, we solve the TCA's displacement using the three models. The comparison between the simulation and experimental results are shown in Fig. 3.10(c). Each experiment is repeated three times, and the green shaded area represents the standard deviation (maximum std = 1.58 mm). From the comparisons, the Cosserat rod model is still the most accurate modeling method.

**Case 3: Dynamics with a hanging weight**

Our final experiment for helical TCAs is to evaluate the accuracy of dynamics. In the experiments, a weight (30 g or 50 g) is hanged at the end of the free-stroke TCA (60 g is not used to prevent the TCA from breaking). A constant voltage (5 V or 6 V) is applied to the TCA. The power and displacement of the TCA are respectively measured as in previous experiments. Each experiment is repeated three times, and the results are shown in Fig. 3.11 (a). The maximum standard

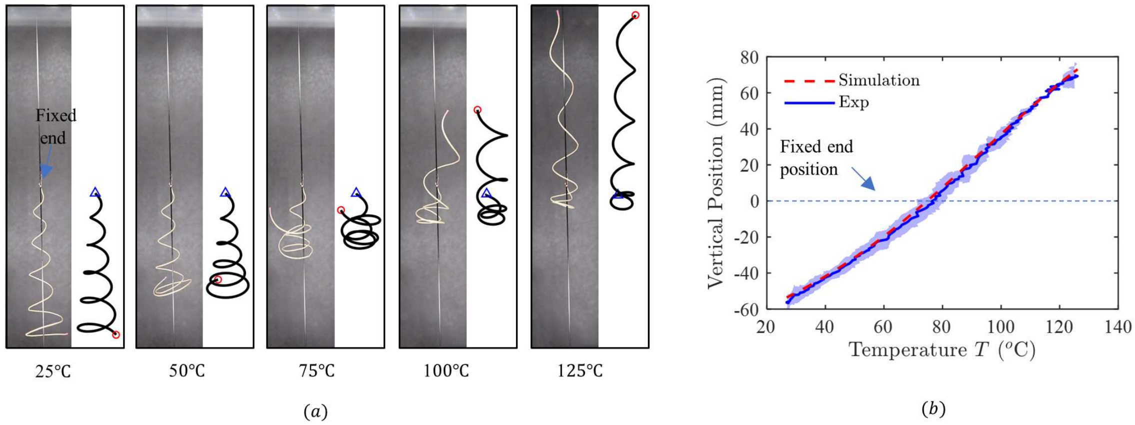


**Figure 3.12:** The experimental and simulation results for the conical TCA. (a) Optical pictures of the conical TCA when heated in an oven compared with simulation results, showing the progression of actuation during heating. The free end is marked with a red circle and the fixed end is marked with a blue triangle. (b) The experimental and simulation results of the conical TCA's end point's vertical position with respect to temperature.

deviation for the four types of experiments is 0.84 mm. The comparison of the experimental and simulation results using the three methods for different combinations of weight and voltages are shown in Fig. 3.11 (b), (c), (d), and (e). With the rod model, the maximum displacement error normalized by the maximum displacement is less than 12% as shown in Fig. 3.11(f), which shows that the Cosserat rod method provides better accuracy compared with the other two methods.

### 3.4.5 Non-uniform Geometry Case: Kinetostatics of a Conical TCA

In this section, we demonstrate the capability of the Cosserat rod model to simulate TCAs of non-uniform geometry (conical TCAs). Conical TCAs can generate dual-side displacement and thus provide stroke over 100%. To make sure the coils can pass each other, the transverse gaps between coils are intentionally designed to be large and thus the load-bearing capability of the conical TCA is small. In our experiment, no load is applied to the end of the conical TCA during the experiments.

The conical TCA is fixed on a vertical carbon fiber rod placed in the oven with a transparent door, and a camera records the actuation of the conical TCA during the heating process. In our simulation, the fixed end is marked with a blue triangle and the free end is marked with a red circle. Figure 3.12(a) shows the optical pictures of the conical TCA and the corresponding simulated shapes for different temperatures (also see our supporting video). The comparison suggests the simulation can well capture the shape of the TCA. The minor error could be caused by the heated air flowing in the oven. The results seem surprising – the bigger coils pass the small coils and it does not exist a moment when all coils coincide on a plane (like a flat spiral). But it is reasonable since larger coils have a larger coil kinematic coefficient $A$ and thus can generate more displacement if no load is applied.

The displacement of the TCA's free endpoint is extracted from the recorded video using Tracker software (https://physlets.org/tracker). Similarly, the temperature is recorded using the thermal sensor used for the helical TCA experiments. Figure 3.12(b) shows the comparison of the simulated and experimental vertical position of the TCA's free end with respect to temperature. The maximum standard deviation for the three repeated experiments is 8.9 mm.

Our proposed model based on the Cosserat rod theory is a general and flexible framework. For generality, besides the three type of TCAs discussed, the Cosserat rod model can be leveraged to model more complicated TCAs (e.g., TCA of ellipse-helical or logarithmic spiral shapes) as long as we can parametrize them along the twisted fiber. The framework can also be extended to model TCA-inspired artificial muscles (e.g., cavatapi [100] and dual-stroke artificial muscles [101] after the untwisting with respect to stimuli is obtained. Similarly, the framework can also be generalized to model stimuli-responsive materials (e.g., shape memory alloy coils) by incorporating memorized shapes and moduli change with respect to the stimuli. For flexibility, this work contains some 'complicated' parts, but the Cosserat rod model can work without considering them for potentially fast computations at the expense of worse accuracy. For example, we considered the dependence of the moduli on temperature and strain, but we can use a constant $E$ and $G$ for the simulation. Note that the main contribution of this work is the general modeling framework for various types of TCAs made from the same twisted fiber. But if a different material or different parameters are used to fabricate the TCA, the properties for the twisted fiber need to be measured to obtain accurate results.

Although Cosserat rod model can provide better accuracy, especially with heavy load and high temperature (Fig. 3.9), the simplified methods (e.g., CST) on average can be computed 10 times faster. For example, the dynamics case using the rod model takes an average of 24 s for a simulation of 1 s while the other methods take around 2 s (all with a step size of 0.05 s running on an Intel Xeon E3-1245 CPU at 3.4GHz). In this case, the simplified models should be used when a TCA is subject to a small payload and low temperature. More generally, based on the discussion in section 3.3, one can customize a simplified model by choosing $A$ and $K_c$ from either the Love's method or the CST method, or even choose to obtain $A$ and $K_c$ through measurement. In the future, however, the computation speed of using Cosserat rod method can be significantly improved by using a discrete elastic rod method [102, 103], implementation in C++, and parallel computing.

Besides the three loading cases, a TCA could subject to more complicated loading cases when used to actuate robots [27]. Our general framework for modeling TCAs can be leveraged for modeling these TCA-driven robots since it allows us to predict the output force and displacement that drive the robot to work. Such a general model even open the possibilities to model the performance of robots driven by TCAs of various shapes, for example robotic morphing skins driven by conical TCAs [9], which is impossible with other TCA modeling methods.

Finally, we focuse on modeling the exact mechanics of a TCA's actuation process without considering the releasing process (i.e., when the temperature decreases). But the releasing can be modeled using the same mechanics model with different temperature profiles as verified by other works [4, 37]. In other words, a TCA's displacement is roughly the same for a specific temperature no matter it is in a releasing or actuation stage. And a TCA's temperature in the releasing stage can be predicted by the same thermal model (Eq. (3.1)) by setting $P_{in} = 0$. For a highly dynamic and cyclic situation, hysteresis and friction effect should be considered for control purposes [81, 104]. In our work, 'lonely stroke' [99] is accounted for by starting the simulation from a crept state, and dynamic hysteresis is described using a damping term that provided a modest approximation for its dynamic behavior. These considerations pave the way for advanced modeling of the nonlinear effects.

## 3.5 Nomenclature and Detailed Derivation

### 3.5.1 Constitutive Law of a General Twisted Yarn

Based on the existing yarn mechanics theory, the twisted fiber is a transversely isotropic material, and its general stress-strain relationships is [92]

$$\begin{bmatrix} \varepsilon_x \\ \varepsilon_y \\ \varepsilon_z \\ \gamma_{xy} \\ \gamma_{yz} \\ \gamma_{xz} \end{bmatrix} = \begin{bmatrix} \frac{1}{E_T} & \frac{-\nu_{TT}}{E_T} & \frac{-\nu_{LT}}{E_L} & 0 & 0 & 0 \\ \frac{-\nu_{TT}}{E_T} & \frac{1}{E_T} & \frac{-\nu_{LT}}{E_L} & 0 & 0 & 0 \\ \frac{-\nu_{TL}}{E_T} & \frac{-\nu_{TL}}{E_T} & \frac{1}{E_L} & 0 & 0 & 0 \\ 0 & 0 & 0 & \frac{1}{G_T} & 0 & 0 \\ 0 & 0 & 0 & 0 & \frac{1}{G_{TL}} & 0 \\ 0 & 0 & 0 & 0 & 0 & \frac{1}{G_{TL}} \end{bmatrix} \begin{bmatrix} \sigma_x \\ \sigma_y \\ \sigma_z \\ \tau_{xy} \\ \tau_{yz} \\ \tau_{xz} \end{bmatrix} \tag{3.34}$$

where the subscripts T and L respectively represent the transverse direction ($x$ or $y$) and longitudinal direction ($z$). $\varepsilon$'s and $\gamma$'s are normal and shear stress, and $\sigma$'s and $\tau$'s are normal and shear strains in mechanics convention. $E_L$ ($E_T$) is the longitudinal (transverse) modulus governing uniaxial loading in the $z$ (transverse) direction , $\nu_{LT}$ ($\nu_{TL}$, $\nu_{TT}$) is the associated Poisson's ratio governing induced transverse (longitudinal, remaining orthogonal transverse) strains. $G_{TL}$ ($G_T$) is the longitudinal (transverse) shear modulus governing shear in the longitudinal direction (transverse plane).

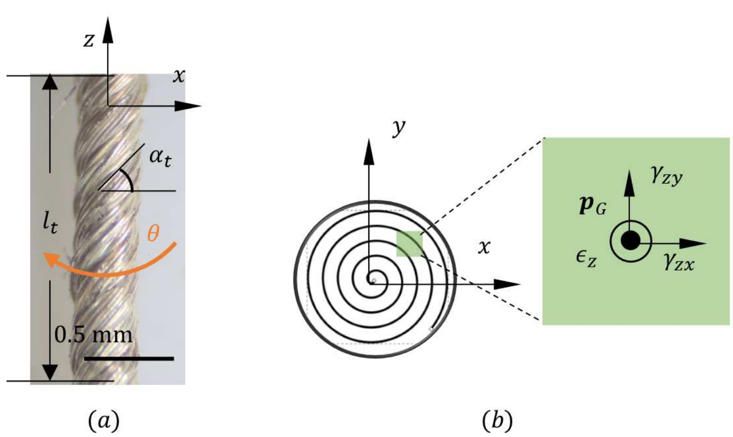


**Figure 3.13:** (a) The microscopic photo of a twisted fiber. (b) Cross section of the twisted fiber taken at the $x-y$ plane of the body frame. Strain quantities on this face of a small volume element at point $p_G$ are shown.

The twisted fiber's mechanical properties depend on its filament direction $\alpha_f$ as shown in Fig. 3.13(a). The Cosserat rod model assumes a rigid cross-section; therefore, $\varepsilon_x, \varepsilon_y$ and $\gamma_{xy}$ do not exist, and the constitutive relation for the transversely isotropic rod reduces to:

$$\sigma_z = E\varepsilon_z,\ \tau_{zx} = G\gamma_{zx},\ \tau_{zy} = G\gamma_{zy} \tag{3.35}$$

where for simplicity, we use $E = E_L$ is the longitudinal Young's modulus, and $G = G_{TL}$ is the longitudinal shear modulus. The strains can be related to the independent variables $v$ and $u$: $[\gamma_{zx}, \gamma_{zy}, \varepsilon_z]^T = \Delta v - p_G \times \Delta u$ where $p_G = [x, y, 0]^T$ is the position of the element within the cross section as shown in Fig. 3.13(b), $\Delta v = v - v^*$ and $\Delta u = u - u^*$, and the values with $*$, $v^*$ and $u^*$, are respectively the values of $v$ and $u$ in the ORS. Manipulating these equations, we can establish a relationship between $\Delta\xi$ and $W$ which simplifies to Eq. (3.8).

### 3.5.2 Identify $h$ and $\lambda$ in

To identify $h$ in Eq. (3.1), we first conduct a statics experiment to infer the actual $T - t$ (temperature-time) relationship of a dynamics experiment, and then use the $T - t$ relationship to identify $h$. For the statics experiment, We slowly heat up a free-stroke TCA with a 60 g at the end in an oven while measuring the $T - x$ (temperature – displacement) relationship. The 60 g (the maximum weight used in our manuscript) will prevent the coils from early contact. After that, we can conduct the dynamics experiment to obtain the $x - t$ relationship of a TCA by applying a constant voltage (5 V). Using the $T - x$ and $x - t$ relationships, we can infer the temperature of the dynamic experiment to obtain the $T - t$ relationship using linear interpolation.

With the $T - t$ relationship, we can perform a linear regression to obtain $h$. Specifically, we formulated an optimization problem: find $h$ that minimizes the root mean square error between the experimental and simulation results $RMSE(h) = \sqrt{\Sigma_{i=1}^{n}(T_{exp,i} - T_{sim,i}(h))/n}$.

$\lambda = \mu_2\tau^2 + \mu_1\tau + \mu_0$ in Eq. (3.11) determines how the strain moduli will change due to large external load under high temperature. The coefficients $\mu_0, \mu_1, \mu_2$ are solved using three pair of values $[\tau_1,\ \lambda_1]$, $[\tau_2,\ \lambda_2]$, $[\tau_3,\ \lambda_3]$, corresponding to three different external loads (0 g, 30 g, and

60 g) applied to the TCA, which are identified through an experiment using a free stroke TCA. We choose 30 g and 60 g because 60 g is the largest load for the TCA in this work and 30 g is the half of the maximum load, over which the moduli changes become significant based on our observations. Since the moduli only drop significantly when the temperature and load are high, we measure the displacement of the TCA at the highest temperature (160°C). When there is no load, we have [$\tau_1$, $\lambda_1$]=[0, 1], which means the change of $E_f$ in Eq. (3.11) is only from the increase of the temperature. When there is a 30 g load, we can obtain $\lambda_2 = 1$ by assuming that there is no moduli change from no load to 30 g. Based on the linear strain deformation theory, $\tau_3 - \tau_2 = \tau_2 - \tau_1$, therefore, $\tau_2 = \tau_3/2$.

When there is a 60 g load, we solve the corresponding [$\tau_3$, $\lambda_3$] as follows. We first calculate the shear modulus corresponding to 60 g using a linear relationship $G_{60} = (l_t r^2 \cos\alpha_{30})/(\Delta x J)\Delta Fe$, where $\Delta x$ is the displacement of the TCA when a weight is increased from 30 g to 60 g, and $\alpha_{30}$ is the pitch angel for the situation with 30 g. $\lambda_3 = 5.68$ can be reversely calculated using Eq. (3.10) and Eq. (3.11) with known $G_{60}$. To obtain the torsional strain $\tau_3$, we first calculate the pitch angle $\alpha_{60}$ using the displacement, and then the torsion strain change with respect to the situation of 30 g can be calculated using $\tau_3 - \tau_2 = (\sin 2\alpha_{60} - \sin 2\alpha_{30})/2r \approx 85.5$ (similar to Eq. (3.19)). Therefore, $[\tau_3, \lambda_3]$ = [171, 5.68] and $[\tau_2, \lambda_2] = [85.5, 1]$. We can find the coefficients $\mu_2$, $\mu_1$, and $\mu_0$ by fitting the three points.

### 3.5.3 The Reference Twist and Boundary Condition for Conical TCAs

We fabricate the conical TCA in conical Archimedes's spiral shape

$$p^*(z) = \begin{bmatrix} bz\cos(az), & bz\sin(az), & z \end{bmatrix}^T \tag{3.36}$$

where $z$ is the vertical height, $b$ is radial scaling factor, and $a$ is angular scaling factor.

To establish initial and boundary condition for the rod model, the rod geometry needs to be parameterized using arc length $s$ that can be easily derived by integrating the derivative of the position vector with respect to $z$

$$s(z) = \int_0^z |\frac{dp^*}{dz}|dz = \frac{1}{2}z\sqrt{1+b^2(1+a^2z^2)} + \frac{1+b^2}{2ab}\sinh^{-1}\left(\frac{abz}{\sqrt{1+z^2}}\right) \tag{3.37}$$

To use the Cosserat rod model, the curve needs to be parameterized using $s$. However, $z$ in Eq. (3.37) cannot be analytically solved and there is no explicit form to express $p$ in terms of $s$ as done for a helix in Eq. (3.12).

To solve this problem, we discrete the spiral into $N$ segments and numerically find $z_i$ for a specific $s_i$ ($i \in [1,N]$) by solving $s(z_i) = s_i$ using Eq.(3.37) by a root searching method ($fzero()$ in Matlab). At the end of $i^{th}$ segment, the curvature and the torsion of the spiral can be found by

$$\kappa^*(z_i) = \frac{abz\sqrt{4+a^2z_i^2+b^2(2+a^2b^2)^2}}{\left(1+b^2(1+a^2z^2)\right)^{3/2}\right)} \tag{3.38}$$

$$\tau^*(z_i) = \frac{a(6+a^2z_i^2)}{4+a^2z_i^2+b^2(2+a^2z_i^2)^2} \tag{3.39}$$

The global frame's $Z$ direction along the centerline of the helical spiral; the body frame's $z$ direction is along tangent direction of the curve and the cross section is in the $x$-$y$ plane. The heated reference strain can be obtained as

$$u^{\mathrm{h}}(z_i) = \begin{bmatrix} 0 \\ \kappa(z_i) \\ \tau(z_i)^* + \Delta\bar{\theta}^{\mathrm{h}} \end{bmatrix}, v^h = v^* = [0,0,1]^T \tag{3.40}$$

The initial orientation and position for $s_i = 0$ are

$$p_0 = [0,0,0]^T, R_0 = R_z(\pi + 0.1) \tag{3.41}$$

The boundary condition for the free end is $W(l_t) = [0,0,0,0,0,0]^T$ since no load is applied.

### 3.5.4 Kinetostatic Modeling using CST

In our previous work [34], CST is directly used to model a TCA, but here we present a more concise derivation. The actuation is considered as an external force, $M_a = \Delta\bar{\theta}^{\mathsf{h}} GJ$ applied along $z$ axis, which means $M_z = -F_e r \cos\alpha - M_e \sin\alpha + M_a$ in $W$. The complementary strain energy will be equal to the strain energy under the small deformation assumption, leading to [105]

$$\begin{aligned} U^* &= \int_0^{l_t} (W^T K^{-1} W) ds \\ &= \int_0^{l_t} [\frac{M_z^2}{2GJ} + \frac{M_y^2}{2EI} + \frac{F_y^2}{2GA_t} + \frac{F_z^2}{2EA_t}] ds \end{aligned} \tag{3.42}$$

where $U^*$ is the complimentary strain energy. Notice that six deformation terms are reduced to four terms since $M_x = 0$ and $F_x = 0$. Since $M_e$ is not considered, we can obtain Eq. (3.29) after we apply CST: $\frac{dU^*}{dF_e} = l^* - l$.

## 3.6 Chapter Summary

This chapter presents a general physics-based modeling framework for various types of TCAs using the Cosserat rod model. Compared with existing works, the model was able to not only provide more accurate results but also simulate TCAs with non-uniform geometries. We also showed that existing Love's and CST methods are two special simplified cases of a Cosserat rod model. This model paved the way to better understand the mechanics of TCAs as well as design TCAs to actuate a variety of robots/systems/devices. Our future work could attempt to improve model accuracy by incorporating additional effects, such as the creeping of the TCA and stress relaxation. Future work will also apply the model for TCA-driven robots, which involves interaction with the environment such as friction and contact forces.

**Table 3.3:** Nomenclature

| Symbol | Unit | Definition |
|---|---|---|
| $r_t$ | m | Twisted fiber radius |
| $l_t$ | m | Length of the twisted fiber |
| $\alpha_t$ | rad | A twisted fiber's bias angle |
| $E$ | Pa | Twisted fiber's longitudinal Young's modulus |
| $G$ | Pa | Twisted fiber's longitudinal shear modulus |
| $r$ | m | radius of a TCA |
| $n_t$ | none | Number of twists in the twisted fiber |
| $n$ | | Number of the TCA's coils |
| $\phi$ | rad | Winding angle of the TCA $\phi = 2\pi n$ |
| $l$ | m | Length of the TCA |
| $\alpha$ | rad | The coil pitch angle of the TCA |
| $\boldsymbol{M}_e$ | N·m | External moment vector applied applied at the boundary |
| $\boldsymbol{F}_e$ | N | External force vector applied at the boundary |
| $A$ | $\mathrm{m}^2$/rad | Coil kinematic coefficient |
| $K_c$ | N/m | Coil Stiffness coefficient |
| $s$ | m | Arc length of a twisted fiber |
| $t$ | sec | Time |
| $p$ | m | Position vector in the global frame |
| $R$ | | Rotational matrix of material cross section |
| $h$ | | Quaternion for the material cross section |
| $u$ | 1/m | Angular strain in the body frame |
| $v$ | | Linear strain in the body frame |
| $\xi$ | | Spatial twist $\xi = \begin{bmatrix} u^T & v^T \end{bmatrix}^T$ in the body frame |
| $m$ | N·m | Internal moment in the body frame |
| $n$ | N | Internal contact force in the body frame |
| $W$ | | Internal wrench $W = \begin{bmatrix} m^T & n^T \end{bmatrix}^T$ in the body frame |
| $\bar{f}$ | N/m | Distributed force in the body frame |
| $\bar{l}$ | N·m/m | Distributed moment in the body frame |
| $\bar{\boldsymbol{W}}_e$ | | Distributed external Wrench applied to the centerline in the body frame $\bar{\boldsymbol{W}}_e = \begin{bmatrix} \bar{l}^T & \bar{f}^T \end{bmatrix}^T$ |
| $\Delta(\cdot)$ | | The change of the variable with respect to the state defined by the superscripts |
| $(\cdot)^*$ | | Variables corresponding to the original reference state |
| $(\cdot)^{\mathsf{h}}$ | | Variables corresponding to the heated reference state |
| $(\cdot)'$ | | Derivative with respect to $s$, $\frac{\partial}{\partial s}$ |
| $\dot{(\cdot)}$ | | Derivative with respect to time, $\frac{\partial}{\partial t}$ |
| $\ddot{(\cdot)}$ | | Derivative with respect to time, $\frac{\partial^2}{\partial t^2}$ |
| $\widehat{\cdot}$ or $(\cdot)^\wedge$ | | Mapping from $\mathbb{R}^3$ to $\mathfrak{so}(3)$ or $\mathbb{R}^6$ to $\mathfrak{se}(3)$, e.g. $\widehat{\xi} = \begin{bmatrix} \widehat{u} & v \\ 0 & 0 \end{bmatrix}$, $\widehat{u} = \begin{bmatrix} 0 & -u_z & u_y \\ u_z & 0 & -u_x \\ -u_y & u_x & 0 \end{bmatrix}$ |
| $\check{\cdot}$ or $(\cdot)^\vee$ | | Inverse of $\widehat{\cdot}$ or $(\cdot)^\wedge$ |

# Chapter 4

# TCA-driven Soft Robots

Based on Chapter 1, the free strokes of the TCAs allow us to embed them with an arbitrary shape inside a soft body to generate programmable and versatile motions. To demonstrate this, we embed TCAs in a curved U shape, a helical shape, and straight shapes in parallel to enable three different motions: two-dimensional bending, twisting, and three-dimensional bending, respectively. These three motions represent typical ways to arrange soft artificial muscles in a 3D shape within a soft body to achieve complex motion. Further, they can be combined together to generate a soft robotic arm that mimics a human forearm to perform pick-and-place tasks. For the results presented below, we only use the same module throughout the experiments (the soft robotic arm comprises the same module used in the characterization sections) to maintain consistency. We also demonstrate the self-sensing of TCAs enables innervated soft robots that can be triggered by external stimuli and also perform closed-loop control without external sensors.

## 4.1 TCA-actuated Soft Robots with Programmable Motions

To better actuate soft robots with TCAs, we introduce a novel fabrication technique of contraction TCAs that will have uniform initial gaps between neighboring coils. In this case, they can contract over 48% without a preload, termed as free stroke. Such free strokes can enable soft robots by directly embedding one or multiple TCAs into a soft body without preloading those TCAs (Fig. 4.1a). With a large free stroke, TCAs can actuate the soft body to achieve a large magnitude of motion. They can also be arranged in different shapes inside a soft body to achieve programmable motions.

### 4.1.1 Two-dimensional Bending

We demonstrate two-dimensional bending motion with a soft gripper that is initially closed and can be opened by actuating an embedded TCA (Fig. 4.2a ). We choose such a design strategy

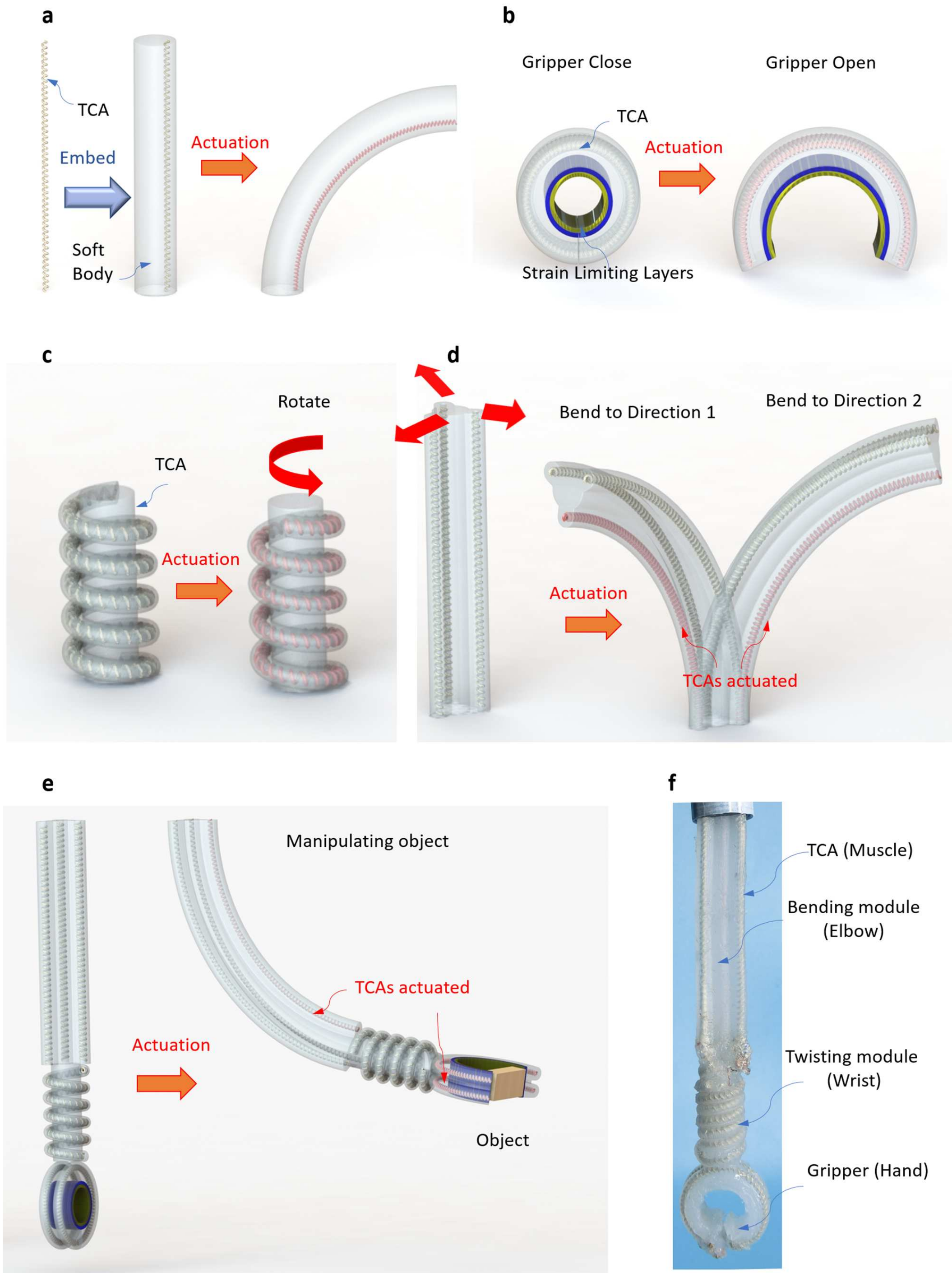


**Figure 4.1:** TCAs with free strokes can enable programmable motions for soft robots. (a) TCAs with free strokes can be directly embedded into a soft body to generate a large bending angle when actuated. (b)-(d) Versatile motions generated by arranging TCAs in soft bodies. (b) A 2D bending module (gripper) with TCA in a curved U shape. (c) A twisting module with a TCA in a helical shape. (d) A 3D bending module with 3 TCAs in parallel. (e) The schematic of a soft robotic arm with a 3D bending module, twisting module, 2D bending module. (f) A prototype of the soft robotic arm.

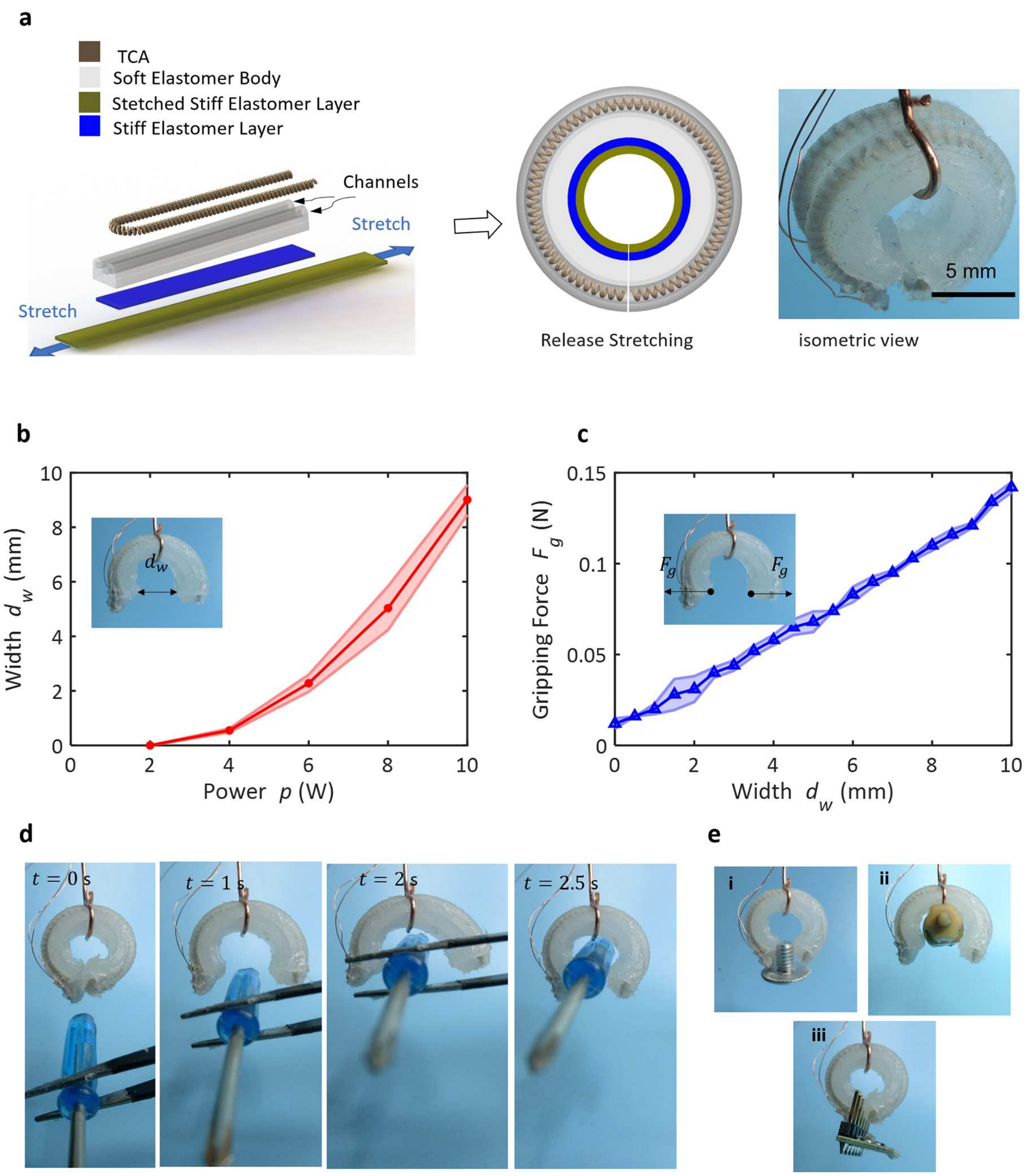


**Figure 4.2:** Two-dimensional bending motion manifested by a gripper which is normally closed and can be opened by actuating an embedded TCA. (a) The fabrication schematic of the gripper and an isometric view. (b) The opening width of the gripper when different power is applied for 2 s. Solid lines indicate the average and shaded regions indicate the standard deviation. The maximum standard deviation is 0.7990 mm. (c) The gripping force of the gripper with respect to the opening width. The maximum standard deviation is 0.085 N. (d) An example gripping process of a screwdriver. Electricity is applied at t = 0 s, the gripper opens wide enough at t = 2 s. Finally, at t = 2.5 s, the gripper closes and holds a screwdriver. (e) Several objects that the gripper can grasp: i. a metal screw. ii. a small DC motor. iii. a printed circuit board.

because the gripper can hold an object without consuming additional energy, whereas traditional soft grippers need to continuously consume energies when holding an object [27]. Further, our design only requires a single TCA, simplifying the design and eliminating possible complicated position control for grasping [106]. The gripper is made of four parts: a curved U-shaped TCA (total length: 70 mm), a straight soft body (size: $35 \times 3 \times 5$ mm), one elastomer layer stiffer than the soft body, and one stretched (120%) elastomer layer (Fig. 4.2a). The soft body has two through holes to host the U-shaped TCA to generate uniform bending. The elastomer layer without prestretch serves as a strain limiting layer, while the one with prestretch bends the soft body to generate an initially closed shape. Such a fabrication allows us to avoid the difficulty to create channels with spatially curved U shape.

To effectively use the proposed gripper for grasping objects with different sizes and weights, we need to address two questions: 1) how to open to different widths ( $d_w$ in Fig. 4.2b) so that it can grasp objects with different sizes; 2) how to determine the gripping force ( $F_g$ in Fig. 4.2c) it can generate at a given open width to make sure it can hold an object without additional energy input. We experimentally address these two questions. First, we evaluate how $d_w$ will change with respect to the applied power for a fixed amount of time (2 s). The results shown in Fig. 4.2b indicate that $d_w$ increases with respect to the input power, and the slope of the curve increases because the TCA displaces longer in the higher temperature region than in the low-temperature region as shown in Fig. 2.5d. To determine the gripping force, we drag the gripper open and record the displacement and force. Results in Fig. 4.2c suggest that $F_g$ increases with respect to $d_w$, which means a larger opening will allow the gripper to hold a heavier object. The almost linear shape for the gripping force with respect to the opening width can be explained by possible analytical solution $w_d = cF_g$ , where $c$ is a constant determined by the geometry and material stiffness (assumed linear within a small range of deformation) [107].

The experimental results shown in Fig. 4.2b and c (The maximum standard deviations are respectively 0.7990 mm and 0.085 N) can be used for guiding the grasping of an object. For an object with a given size and weight, we can first determine if it is possible to hold it using results

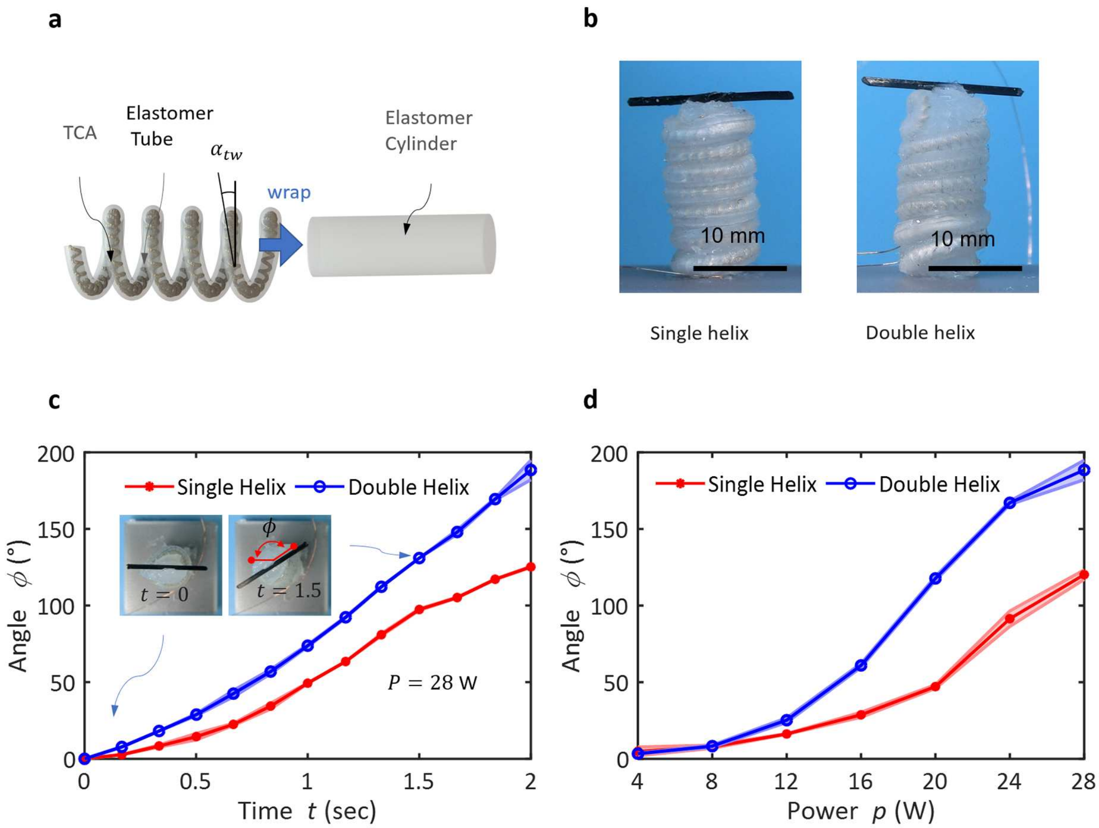


**Figure 4.3:** Twisting motion generated by wrapping a TCA around a cylindrical soft body. (a) The schematic of fabricating the twisting module. (b) The twisting module with two different wrapping strategies: single helix or a double helix. (c) The twisting angles $\phi$ of the twisting module with respect to time when a power of 28 W is applied. (d) The twisting angle of the two modules after applying different power for 2 s. The lines indicate the average and shaded regions indicate the standard deviation and the maximum standard deviations are both 6.3640° for (c) and (d)

in Fig. 4.2c (given a rough estimation of the friction coefficient). If it is possible to hold it, we can use the results in Fig. 4.2b to apply a proper power to open the gripper to a width that is slightly larger than the object's size. An example grasping process is shown sequentially in Fig. 4.2d with a screwdriver. The gripper can also grasp different objects (a printed circuit board, a screw, and a DC motor) with a variety of sizes and weights owing to the softness of the gripper (Fig. 4.2e).

### 4.1.2 Twisting

To enable twisting motion, we wrap a TCA in a helical shape around a cylindrical soft body (Fig. 4.3a). Before wrapping, the TCA is first inserted into an elastomer tube to protect the TCA.

We investigate two wrapping strategies using TCAs with the same total length (Fig. 4.3b) to compare the twisting results: a single and double helix. A single helix is obtained by wrapping a TCA uniformly along the soft body, while a double helix is fabricated by folding the TCA in half before wrapping it on the soft body. To make the twisting module compact (short), we wrap the TCA in both cases as close as possible.

To characterize the twisting motion, we record the twisting angle ($\phi$) with respect to time by applying the same power on the two different twisting modules (Fig. 4.3c), as well as different power for the same amount of time (Fig. 4.3d). For the results shown in Fig. 4.3c, the constant power is chosen as 28 W so that the double helix module can rotate around 180° in 2 s. The final twisting angle ( $\phi$) of the two designs gradually increases with respect to time. As shown in Fig. 4.3c and d (the maximum standard deviations are both 6.36° for the two figures), the double helix one can rotate faster and realize a larger angle than the single helix one under the same energy input (i.e., same actuation power for the same amount of time). This is because the force generated by the double helix is almost twice the single helix for the same energy input due to the small difference in their averaging wrapping angle ($<$ 10 degrees). So the single helix module is limited by the force instead of displacement that a TCA can generate.

### 4.1.3 Three-dimensional Bending

We can also achieve three-dimensional bending motion by placing three TCAs in parallel through three channels in a cylindrical soft body (Fig. 4.4a). By properly actuating the three TCAs, we can bend the soft body towards a specific direction (bending direction $\gamma$ ) with a specific amplitude (bending angle $\theta$ , Fig. 4.4b). To characterize how will $\gamma$ and $\theta$ change with respect to the input power for the three TCAs, we choose to apply different powers to TCA1 and TCA2 since other combinations will be similar (TCA1 and TCA3, TCA2 and TCA3). The bending direction $\gamma$ will be determined by the ratio of powers applied to TCA1 and TCA2, while bending angle will be determined by the magnitude of powers applied to TCA1 and TCA2. Therefore, we perform two sets of experiments. In each set, we fix the power applying to TCA2 $P_2$ , while change the power

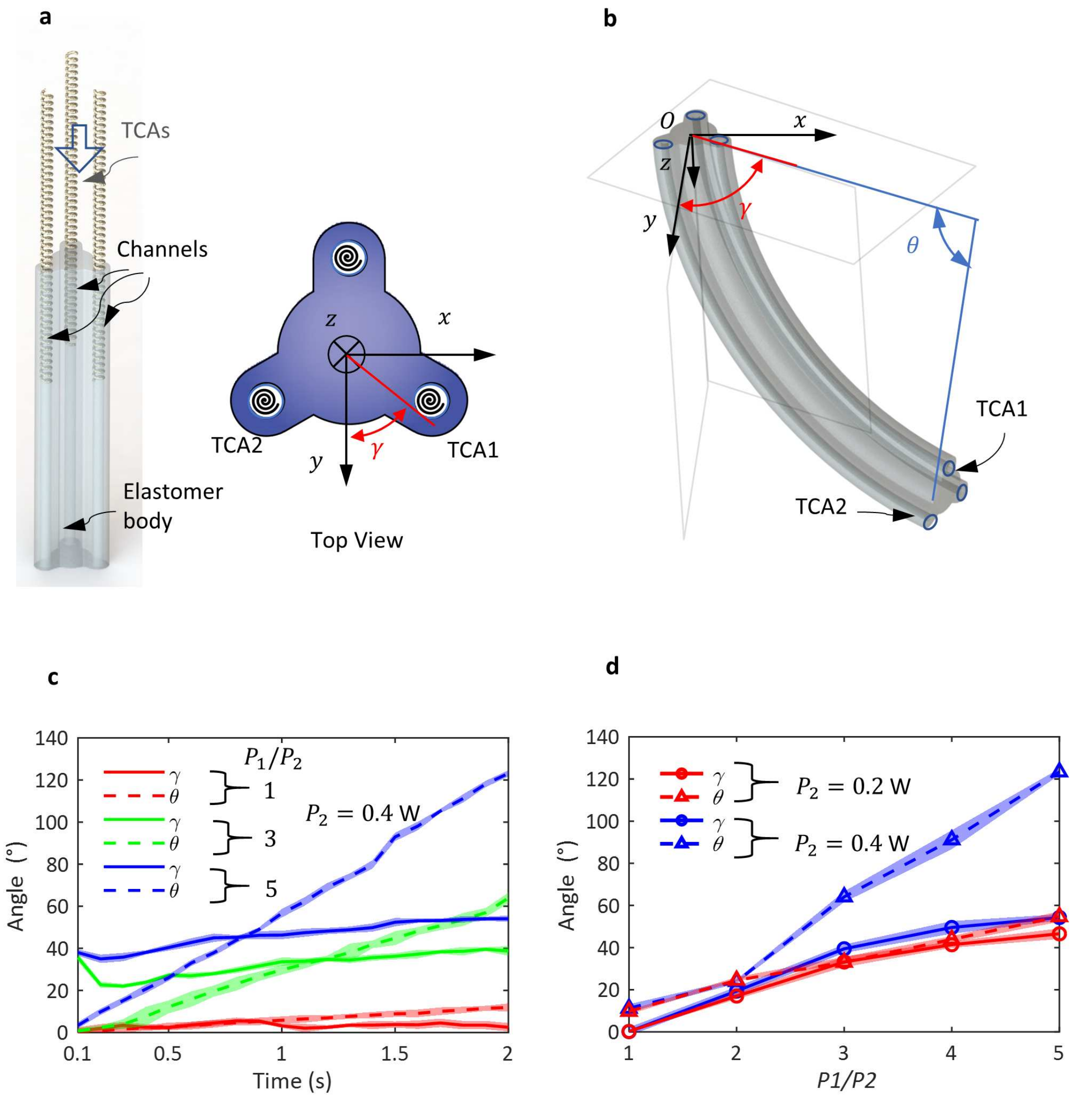


**Figure 4.4:** 3D bending motion generated by three TCAs placed in parallel in a soft body. (a) The schematic to fabricate the 3D bending module with the top view shown on the right. (b) A three-dimensional schematic showing bending direction $\gamma$ and the bending angle $\theta$. (c) The bending angle and the bending direction with respect to time. (d) The bending angle and the bending direction with respect to input power ratio for two cases P2 = 0.2 W and P2 = 0.4 W. For both (c) and (d), the lines indicate the average and shaded regions indicate the standard deviation. The maximum standard deviation of all curves for (c) is 4.53° and for (d) is 4.49°.

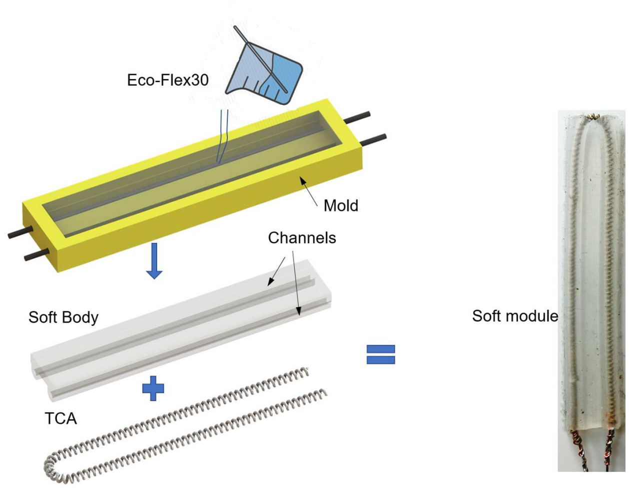


**Figure 4.5:** The fabrication process of the soft modules with an example.

applied to TCA1 $P_1$, thereby changing the power ratio $P_1/P_2$. For the first set of experiments, $P_2 = 0.2$ W, and the ratio $P_1/P_2$ changes from 1 to 5, while for the second set, $P_2 = 0.4$ W, and $P_1/P_2$ varies in the same range.

To obtain $\gamma$ and $\theta$ , we use a motion tracking system (Trio v120, OptiTrack) to track the end position of the 3D bending module (marker 2, Fig. 4.5). In the simplest case [39], we can assume the module has a constant bending curvature $\kappa = 1/r$ due to the relatively small weight at the end. In this case, $\gamma$ and $\theta$ can be solved from the end position of the module through the following minimization problem [108]:

$$min f(\gamma, \theta) = \|p - p'\| \tag{4.1}$$

$$s.t. \gamma \in [0°, 90°], \theta \in [0°, 180°] \tag{4.2}$$

where $p' = [p'_x, p'_y, p'_z]^T$, $p = [p_x, p_y, p_z]^T = L/\theta[\sin\gamma(1-\cos\theta), \cos\gamma(1-\cos\theta), \cos\theta]^T$ with $p'$ the end position measured in experiments, $p$ the end position represented using $\gamma$ and $\theta$, and $L$ is the length of the module.

Figure 4.4c shows $\gamma$ and $\theta$ change with respect to time under the same $P_2$ = 0.4W but different power ratio ($P_1/P_2$). The bending direction solid lines and the bending angle (dashed lines) increase with respect to time. The slope of $\theta$ is more influenced by the power ratio than $\gamma$. The increase of $\gamma$ and $\theta$ is almost linear, though $\gamma$ may decrease a little in the beginning. Figure 4.4d shows the final values of $\gamma$ and $\theta$ with respect to the power ratio ($P_1/P_2$) after applying electricity for 2 s. For the bending angle with the same $P_2$, it increases with respect to the power ratio, meaning the module bends more towards TCA1. Also, the values for $\gamma$ are approximately the same for the two different sets of experiments for the same power ratio, suggesting it indeed depends on the power ratio instead of the magnitude.

For the bending magnitude $\theta$, it increases with respect to the power ratio, similar to the trend for $\gamma$. But unlike $\gamma$, $\theta$ also depends on the magnitude of power. In fact, when the power ratio is the same, the bending magnitude for $P_2$ = 0.4 W can be much larger than the case with $P_2$ = 0.2 W. For instance, $\theta$ is around 120° when $P_1$ = 2 W and $P_2$ = 0.4 W, whereas it is only around 50° when $P_1$ = 1 W and $P_2$ = 0.2 W. Note that the applied power is relatively small compared with the input for the twisting module since the 3D bending module has a much smaller bending stiffness than the torsional stiffness. Also, due to the initial curved shape and inaccurate measurement, $\theta$ may have a maximum initial error of 10°. The maximum standard deviation for Fig. 4.4c and d are respectively 4.53° and 4.49°.

### 4.1.4 Combination of Modular Motions – A Soft Robotic Arm

We can combine the three modular motions (2D bending, twisting, and 3D bending) to develop a soft robotic arm: the gripper as a hand, the twisting module as a wrist, and the 3D bending module as an arm. Similar to the human's forearm, the robotic arm can achieve complicated motion and thus functions, for example, to pick and place an object by coordinating the three modules(Fig 4.1e and f). In our design, the arm is fabricated by connecting the gripper, the twisting module, and the 3D bending module in serial, with the end of the 3D bending module fixing to a base that can only move up and down (Fig. 4.6). The total weight of the arm is 6 g and the dimension is around $10 \times 10 \times 70$ mm.

Figure 4.6 shows the robotic arm can pick up different objects (a screwdriver and a PCB) and place them in different cups. In the process, the object is placed right under the arm with a known a

b

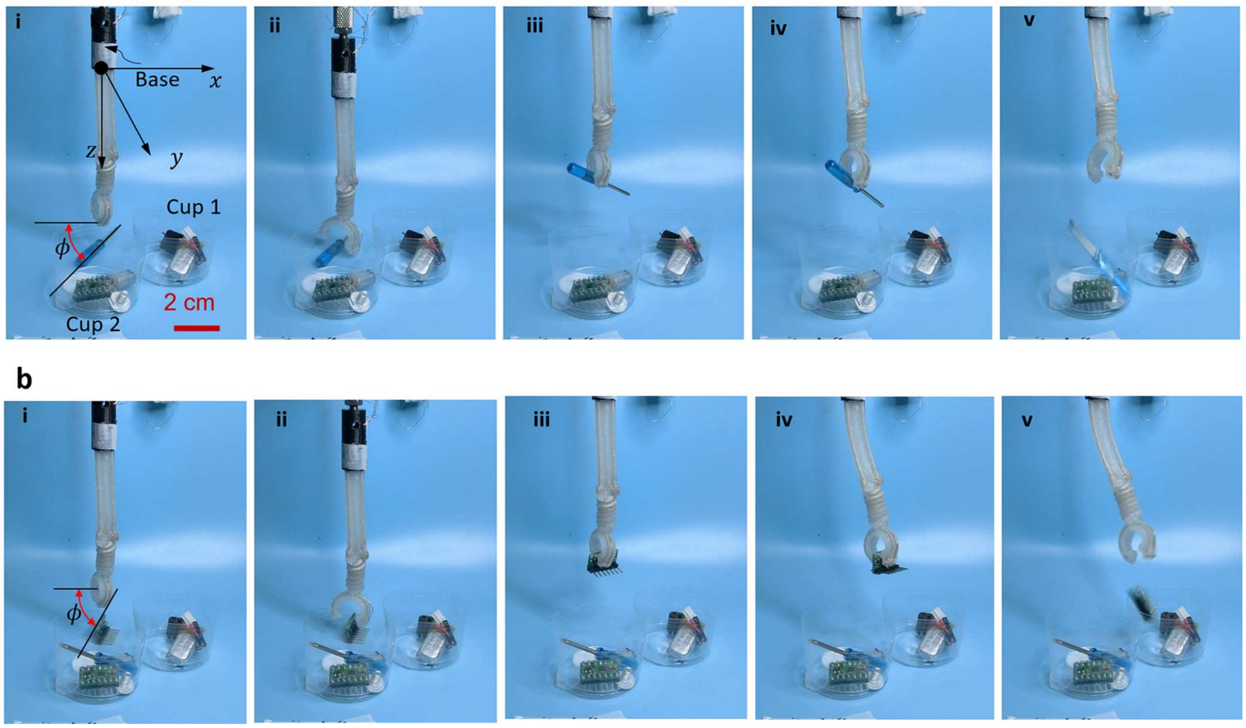


**Figure 4.6:** A soft robotic arm that can perform pick-and-place tasks. (a) and (b) i. The object is placed under the gripper. ii. The gripper opens and rotates when the arm approaches the object. iii. The gripper grasps the object and lifts it to a certain height. iv. The arm bends towards the target cup. v. The gripper releases the object into the cup.

orientation. In this case, the wrist needs to first rotate some angles (around 45° with an input power of 14 W in Fig. 4.6a(i) and around 58° with input power of 16 W in Fig. 4.6b(i)) to align the gripper with the object. Then, according to the width of the object, the gripper opens different widths to grip the object (10 W in Fig. 4.6a(ii) and 8 W in Fig. 4.6b(ii)). After grasping the object, the wrist will return to its original orientation and the arm lifts the object to some heights by moving up the base in Fig. 4.6a and b(iii). Then, the arm bends towards a desired cup ( $P_1$ = 0.6 W, $P_2$ = 0.6 W in Fig. 4.6a(iv) and $P_1$ = 0.2 W, $P_2$ = 0.8 W in Fig. 4.6b(iv)). Finally, the arm releases the object by opening the gripper. Note that the 3D bending module can still bend noticeably (larger than 30 °) with the additional weight of the gripper, the twisting module, and the object.

## 4.2 Innervated Soft Robot using Self-Sensing of TCAs

Based on the results in Section 2.3, the free-stroke TCA not only can actuate a soft finger but also enable the finger to sense and respond accordingly. In the following, the design and fabrication of the finger are first introduced, and then the finger's resistance-bending angle (R-$\theta$) relationship is characterized for the feedback control ($\theta$ is shown in Fig. 4.7(c). After that, we demonstrate that the innervated finger can sense environmental stimuli and respond to it.

### 4.2.1 Fabrication and Characterization of the Soft Finger

We fabricate our soft finger by assembling TCAs and the soft bodies (Fig. 4.7(a)) instead of directly embedding the TCAs in the curing process of the soft material. The method allows more flexibility in arranging TCA in the soft body, and more importantly, a damaged TCA can be easily replaced.

The fabrication procedures are [86]: 1) Fabricate soft bodies with channels. 2) Assemble TCAs in the soft bodies. Based on the length of channels in a soft body, we cut all three TCAs into the same length (45 mm) and then the TCAs are sewed into the soft body passing through the channels. 3) Connect electrical leads to the TCAs. After that, we stuck the two ends of the TCAs on the body

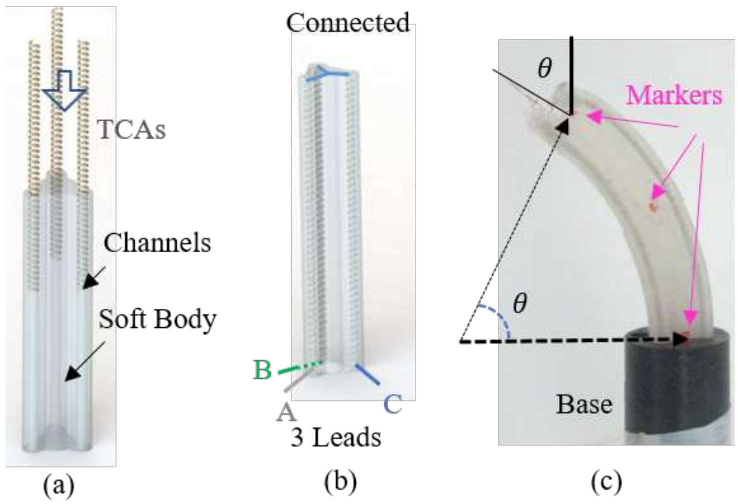


**Figure 4.7:** (a) Schematic of the soft finger. (b) The schematic shows how leads are connected. (c). The finger with markers showing the bending angle.

with Sil-Poxy Silicone Adhesive (Smooth-On Inc). Finally, we fix one end of the finger on a rigid base so that the other end can move freely.

To simplify the control, the three TCAs' top end is connected and two TCAs are actuated at the same time by applying a voltage between lead A and B (Fig. 4.7(b)). Since the load and the displacement of the TCA are both varying, we need to first measure the relationship between the bending angle of the finger and the TCA's resistance (R-$\theta$ relationship) for the closed-loop control. A constant voltage (5 V) is used to actuate the finger and the bending process is recorded. The curvature $\kappa$ is abstracted from the three markers on the body using Tracker software (https://physlets.org/tracker/) and the bending angle $\theta = L\kappa$ is calculated by assuming the arc length of the finger $L = 40$ mm does not change as shown in Fig. 4.7(c). A third-order polynomial is used to fit the curve and the RMSE is 1.6337°.

### 4.2.2 Experiments of the Innervated Soft Finger

Figure 4.8(a) shows the following scenario: the robot will sense an applied bending force and start to bend 60°and hold the configuration for 8 s. The corresponding bending angle and the resistance are shown in Fig. 4.8(b). In the experiments, the resistance of the finger is continuously

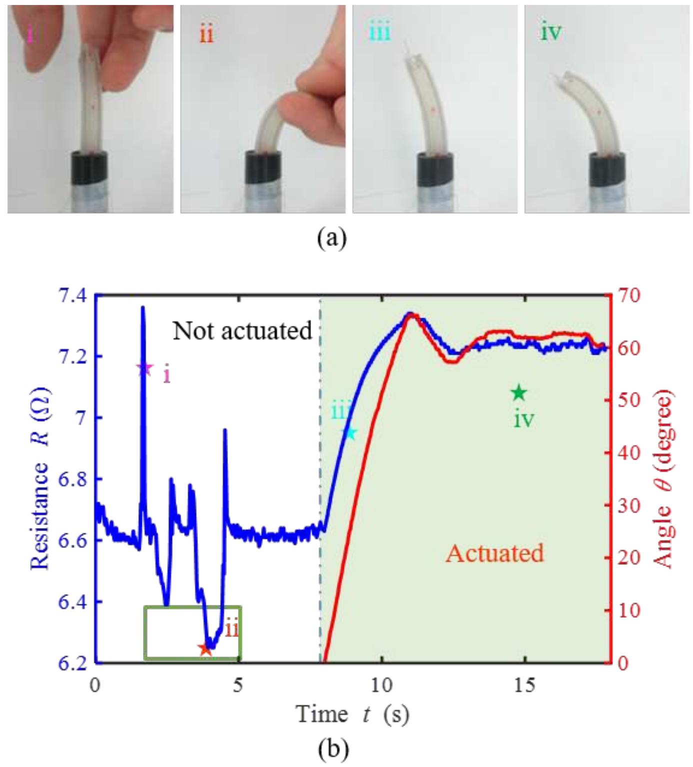


**Figure 4.8:** (a) The snapshots of the autonomous bending finger that is triggered by external stimuli. i ,ii , iii, iv are marked with stars in (b). (b) The resistance of the soft finger and the bending angle with respect to time.

monitored from the beginning and then the robot will be triggered (a step response of 60° bending) once a resistance that is lower 0.2 ohms than the initial value (6.6 ohms) is sensed.

The bending process is also controlled by a PI controller. From the perspective of a dynamic system, the finger can bend as fast as possible when the TCA is strong enough and sufficient power is supplied. However, from the perspective of a thermal system, it takes much longer for the finger to reach a steady-state temperature due to the relatively large heat capacity and the low thermal conductivity of the soft body. The mismatch between the motion dynamic and thermal-dynamic process of the finger causes two problems. First, it takes much longer for the finger's temperature to reach a steady-state after its shape has already arrived at the target configuration. So, the TCA's surrounding temperature (soft body temperature) is changing while the finger is holding the configuration, which could be considered a disturbance. For such a reason, the finger vibrates around the target configuration, and the vibration magnitude gradually decreases as the temperature of the soft body approaches steady-state.

It is desirable that the finger can arrive at the target position as fast possible (using a large $K_P$) but also guarantee the stability of the system. But this cannot be accomplished using fixed PI parameters since there is a conflict between response speed and stability. In this application, adaptive control parameters are applied to make the dynamic response faster and stable. We first use a larger $K_P = 20$, but tune it to be $K_P = 3$ after the error is small enough ($1^\circ$). With such a controller, the finger has a raising time around 1.5 s and steady-state error within 5% with $K_I = 0.08$.

## 4.3 Strong Soft Robots with Bistability

Soft robots can interact with environments and humans in simplified, safer, and adaptive ways owing to their body compliance. However, they usually cannot generate large forces also due to the body compliance, thus unable to realize fast motion. Although some soft robots can realize some rapid motions [14,109,110], they require an intensive power input. But intensive power inputs may not be always possible due to the limited capability of actuators such as motors, compressors, and especially artificial muscles, or sometimes due to limited power supply, especially when a robot is untethered. To address this problem, we leverage the internal energy stored in a soft robot to realize strong and fast motion without an intensive power input and strong actuators.

Our proposed strategy is to actively design the energy landscape for a soft robot, which can be considered as the total strain energy in the robot with respect to its deformation (e.g., bending angle for a soft manipulator). The energy landscape for a traditional soft robot in general is monostable, i.e., it only has one minimum, corresponding to a single stable state (Fig. 4.9a). When deformed under external actuation, the robot will return to this state if the actuation is removed. We propose to tune the energy landscape to achieve two local minima (details in section 4.3.1) corresponding to two stable states (Fig. 4.9b) by adding an additional elastic element (e.g., springs). To switch from one stable state to the other, the soft body needs to first store energy to surpass an energy peak,

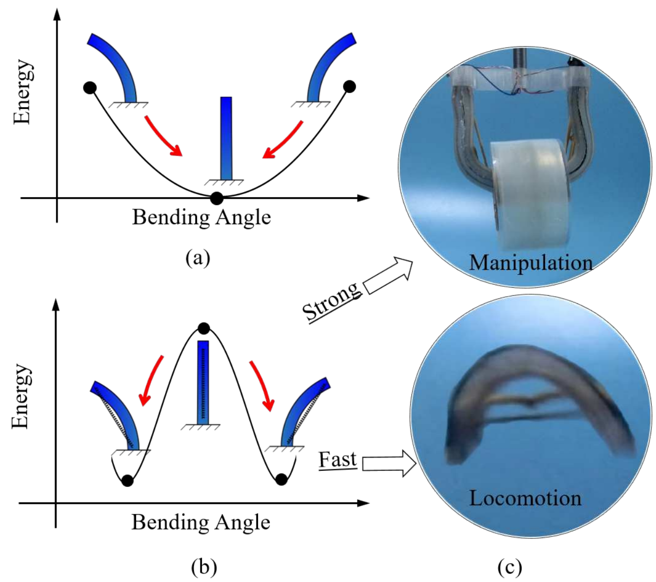


**Figure 4.9:** The proposed strategy for shaping the energy landscape of soft robots to enable fast and strong motion. (a) The energy landscape for traditional soft robots has one energy minimum corresponding to one stable state. (b) The energy landscape can be tuned to have two minima corresponding to two stable states. (c) Such a strategy can be used for strong manipulators and fast locomotion.

after which the stored energy can be released to generate fast motion. With such bistable designs, the dynamics for a soft robot can be actively tuned for strong manipulation and fast locomotion (Fig. 4.9c and the supporting video).

Our proposed strategy belongs to a more general framework called bistable or multistable mechanisms, for which a mechanism has two or more stable states. Such a strategy has recently been exploited in various areas beyond soft robots. For instance, it has been used to develop bio-inspired spring origami for shape morphing [111], dual stiffness structures for aerial robots [112], deployable structures [113], metamaterials for shock absorption [114], bistable valves to control air flow [115], perching mechanism for drones [116], and legs for swimming robots [117]. However, most of existing mechanisms rely on both rigid and soft components to design compliant bistable mechanisms [118]. It remains largely unknown on how to exploit the bistablity for soft robots to enable fast and strong motion.

We aim to investigate how to a tune energy landscape for desired stable states (bistable or monostable) for a soft module. This is accomplished by two competing energy-storing components: 1) potential energy in a linear spring attached to the body; 2) potential energy generated by the bending of the soft body. By actively designing these two energies, the total energy landscape for the module can be tuned to achieve a desired shape: symmetrically bistable (SB), asymmetrically bistable (AB), and monostable (MS). Using a soft actuator – twisted-and-coiled actuator (TCA) to actuate the module, we demonstrate that a soft gripper that can hold weights more than 8 times of its own weight, and a soft jumping robot that can jump more than 5 times its body height.

There are two main contributions this section. First, we propose a strategy to enhance the performance of soft robots: actively designing the energy landscape. We also perform detailed analysis using finite element method for how to implement the strategy. Second, we implement the proposed strategy and demonstrate its effectiveness by developing soft robots for manipulation (grasping) and locomotion (jumping) as shown in Fig. 4.9c. Such robots are driven by a light-weight and electrical-driven TCAs [119], which can potentially be used for untethered locomotion [25].

### 4.3.1 Working Principle

In this section, we introduce the working principle using a soft bending module. As shown in Fig. 4.10, the module has a flexible plastic sheet sandwiched between two soft bodies. Each soft body has two parallel channels to host an actuator, which can be a cable or a TCA. A linear spring is attached on the plastic sheet, and can freely move through a large hole in the plastic sheet when the module bends. The plastic sheet can have various initial shapes, i.e., it can either have an initially straight or curved shape. The spring can have various length and stiffness before attaching to the plastic sheet.

With such a design, we can tune the energy landscape for the module since the total energy is mainly comprised of two major components: potential energy from bending the soft body (bending potential energy), potential energy from stretching the spring (stretching potential energy). Such two components can be individually tuned by designing the initial shape of the plastic sheet and the initial length and stiffness of the spring. To illustrate the principle, we use a simplified linear model

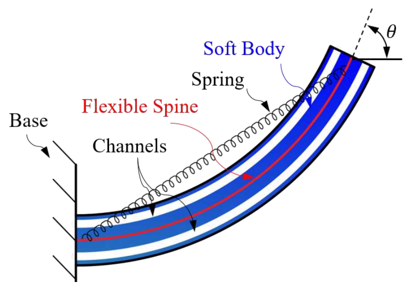


**Figure 4.10:** Schematic of the proposed soft bending module with tunable energy landscapes.

in this section, and a more accurate model using finite element analysis (FEA) will be introduced in section 4.3.3.

Both the bending and stretching energies can be approximated using functions with respect to the bending angle $\theta$ as in Fig. 4.10. Assume the initial shape of the plastic sheet is at a bending angle $\theta_0$, the strain energy stored in the sheet due to bending with respect to $\theta$ is

$$U_b = \frac{1}{2}k_b(\theta - \theta_0)^2 \tag{4.3}$$

where $k_b$ is the effective bending stiffness of the sheet and the body. The stretching strain energy in the spring is

$$U_l = \frac{1}{2}k_l(\Delta L)^2 \tag{4.4}$$

where $k_l$ is the linear stiffness of the spring, $\Delta L$ is the length change of the spring, which can be written as a function of $\theta$: $\Delta L = \frac{2L_{max}}{\theta} sin(\frac{\theta}{2}) - L_{in}$, where $L_{max}$ is the maximum length of the spring when the module bends, and $L_{in}$ is the initial length of the spring under no load. The total energy for the module is thus

$$U_{tot} = U_b + U_l = \frac{1}{2}k_b(\theta - \theta_0)^2 + \frac{1}{2}k_l(\Delta L)^2 \tag{4.5}$$

With the two potential energies, we can design the energy landscape of the module $U_{tot}$ to achieve three different interesting cases: symmetric bistable (SB), asymmetric bistable (AB), and monostable (MS).

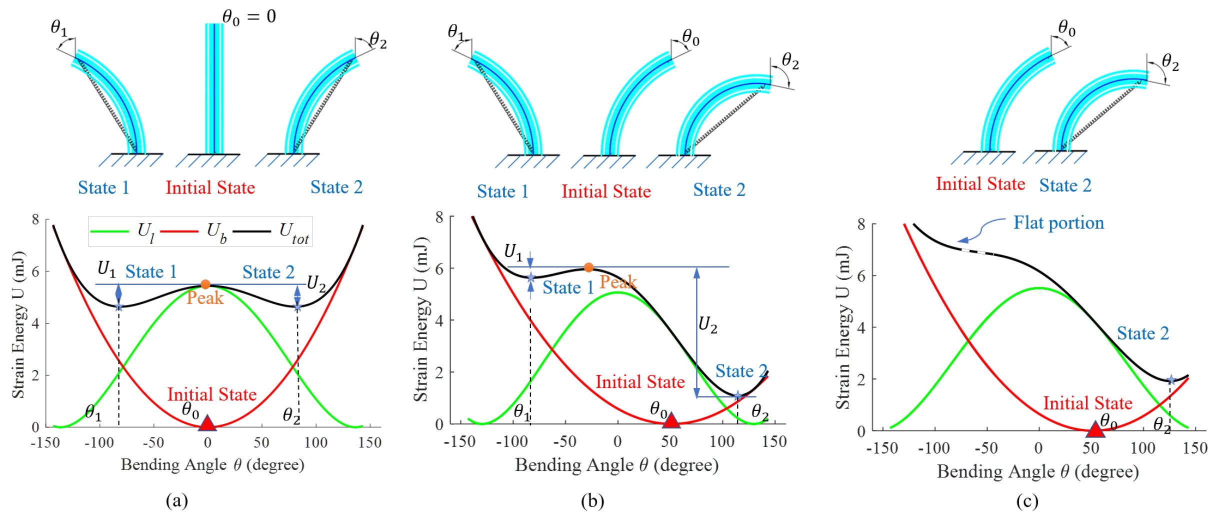


**Figure 4.11:** Different configurations of the energy landscape for a soft bending module. (a) Symmetric bistable (SB). (b) Asymmetric bistable (AB). (c) Monostable (MS).

- SB (Fig. 4.11a): The soft body is initially designed to be straight (i.e., $\theta_0 = 0$). In this case, the bending potential energy is a parabola with the minimum value at zero bending angle. Combining this energy profile with the stretching potential energy, we obtain a symmetric profile for the total energy.

- AB (Fig. 4.11b): The soft body is initially designed to be bent at an angle (i.e., $\theta_0 \neq 0$). Therefore, the bending potential energy will be shifted to the right, while the stretching potential energy will be the same. Combining these two energies together, we obtain an asymmetric energy profile with the left energy barrier (the energy difference in height between a local minimum and a neighboring energy peak) much smaller than the right one. In this case, it will be easier to switch from state 1 to state 2 owing to a smaller energy barrier.

- MS (Fig. 4.11c): By properly adjusting the peak value for the stretching potential energy, the left stable state (state 1) can disappear, leaving only state 2 as the single minimum for the total potential energy. In this case, the system is monostable.

Each of the three different types of energy landscapes has their own advantages compared with a normal bending module without a spring. An SB module (Fig. 4.11a) has a flat portion around the energy peak and two stable states. In this way, an SB module can store/release energy in the bending process, generating faster dynamics after the energy peak. An SB module may be used for robots that require faster symmetrical oscillatory motion (e.g., the repetitive bending motion in a robotic fish).

An AB module has an obvious advantage: a small energy input will allow it to pass the energy peak from state 1 to state 2, releasing a larger amount of stored energy than the input energy. This advantage can be interpreted in two perspectives. In terms of dynamics, the larger released energy will shape the dynamics the soft body to generate a relatively fast motion after the energy peak. In this case, it can be used for robot locomotion requiring an instant release of a large amount of energy (e.g., jumping [120]). On the other hand, in terms of statics, the module initially in state 2 will need a larger force to switch to state 1 compared with an SB module. In this case, an AB module is ideal for robotic fingers that can passively hold some weights.

A MS module's energy landscape could have a flat portion that means the stiffness of the module becomes almost zero, and it does not require energy for the module to bend more. In this case, the module will bend fast when driven force from the actuators is constant.

Although the proposed soft module contains a plastic sheet, it still preserves the most important features of soft robots – a continuum body that has infinite degrees of freedom, safe to humans, and resilient to harsh conditions. We can find similar examples in the biological world. Serpentes (snake) families with extraordinary dexterity have inspired many soft robots with this kind of structures – flexible spinal columns made up of many vertebrae and ligaments that can store energy. So, in the following, we refer the plastic sheet as a flexible spine.

### 4.3.2 Materials and Fabrication

A bending module is composed of the components as shown in Fig. 4.12(a), including: two TCAs (it can also be cables), two soft bodies with channels, a flexible spine, and a spring. Since the fabrication processes for different types of modules are similar, we illustrate the detailed fabrication process with the SB module. The actuator TCA is an artificial muscle that will contract or

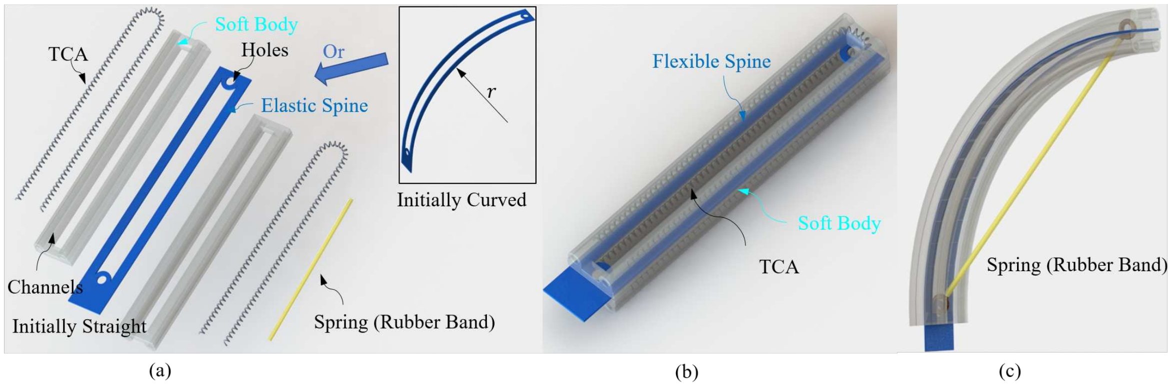


**Figure 4.12:** Fabrication process of the module. (a) All the components except the spring are assembled together to generate a complete module in (b). The spring is finally attached to the spine in (c).

extend [121] when subjected to Joule heating using electricity. It is low-cost compared to the more prevalent artificial muscles such as the shape memory alloy (SMA) and shape memory polymer (SMP). The TCA can contract by over 50% after heating, lift loads over 100 times heavier than can human muscle of the same length and weight [1]. The detailed treatment of TCAs can be found in [1]. We use a recently invented method to fabricate TCA with final geometry parameter: Outer diameter 1 mm, inner diameter 0.4 mm [87].

The fabrication of the bending module comprises three major steps. 1) Fabricate the flexible spine. The flexible spine is directly printed in a flat shape using a 3D printer (Prusa M3K3) with NylonX (MatterHackers Inc.). 2) Fabricate the soft body. The soft body is fabricated through standard molding method [122] for soft robots by curing mixed liquid EcoFlex-30 (Smooth-On, Inc.) in a 3D printed mold. We create channels by inserting carbon fiber rods into the mold, which are removed before demolding. 3) Assemble all the components. The spine and the soft bodies are combined together using Sil-Poxy Silicone Adhesive (Smooth-On Inc.) in Fig. 4.12b. After that, a folded rubber band with a length of 32 mm (Standard size 19, width = 1/16”) is attached to the holes in the flexible spine as in Fig. 4.12c. Finally, We insert TCAs into the two channels in the soft body to form an U-shape to generate large actuation force. Extra silicone adhesive is used to fix the two electric leads of the TCA on the soft body. The dimension for a straight module (Fig. 4.12b) is $45 \times 10 \times 8$ mm, and the thickness of the spine is 0.35 mm. We select NylonX, a nylon filament reinforced by adding micro-carbon fibers, to print the spine for two reasons. First, it retains the durability and flexibility of Nylon. Second, it can also retain its shape and stiffness when TCAs are thermally actuated as NylonX has a high heat defection temperature (150°C).

An AS soft module is fabricated by using an initially curved flexible spine in step (2), which is shown in the inset of Fig. 4.12a. We fabricate an initially curved spine from the flat one. First, we tape a flat spine to a heat-resistant cylinder (beakers) to form an arc shape. Then, we heat the spine over its glass transition temperature (180°C). The spine will keep the arc shape after cooling down and removing the tapes. We can use beakers of various diameters to fabricate spines with different initial curvatures.

### 4.3.3 Simulation and Characterization

The simplified model for energy analysis in section 4.3.1 is used to illustrate the working principle. In this section, we utilize FEA to perform detailed simulations and compare with experimental results for a single module.

#### Model Using Finite Element Analysis

For FEA simulations, we want to see how much force is required to trigger the switching of the module, and how the initial bending angle $\theta_0$ will influence the triggering force, which is the maximum force required for an actuator to switch the module's states. Since an AB module can be driven with any soft actuator such as cable, TCA, or SMA, here we assume the module is driven by cables to simplify the experimental procedure.

We conduct the FEA with Abaqus 6.14 (Dassault Systèmes Simulia Corp). The model can be simplified into 2D, and thus only a beam element type (B21) is used. The FEA model uses a spine of rectangular shape that has the same effective bending stiffness of the spine plus the soft body by specifying the second moment of area of the rectangular shape as the sum of the second moment of area of the spine and the soft body. Discrete channels are also simulated using a set of beam elements as shown in Fig. 4.13. The cable is also modeled with the beam element. A kinematic coupling interaction is used to attach the cable to the tip of the spine. A contact is established between the cable and the discrete channel. The spring is modeled with an Axial connector element (CONN3D2), with its two ends attached to the two nodes of the spine. We use a force stand (MARK-10, ESM303 stand & M5-2 force gauge) to obtain a force-displacement relationship of the spring and input it to Abaqus. As a boundary condition, the bottom of the spine is fixed.

In a simulation, there are two load steps. (1) A static step that allows the spring balances with the flexible spine to reach a steady state. (2) A full dynamics step analysis applies a pulling displacement with a slow speed as a boundary on the cable that will trigger the switching of states. The triggering force is the maximum force from the force-displacement curve of the cable recorded during the simulation.

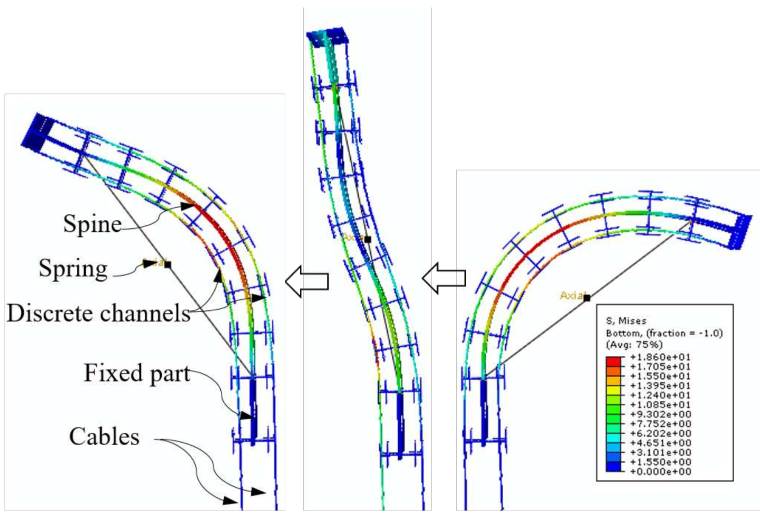


**Figure 4.13:** Different states in the FEA simulation.

### Experiments and Comparison

We experimentally test the triggering forces for different bending modules with different initial curvatures and compare the experimental results with those generated from FEA. For the experiments, we use cables to apply the force ($F_1$ on the left and $F_2$ on the right, Fig. 4.14a). When switching from state 1 to state 2, we let $F_1 = 0$ and gradually increase $F_2$. In this case, the module starts to bend toward the right side (state 2). When $F_2$ is increased to a threshold value, $F_{t2}$, the module passes through the critical point and bends automatically to the right side (state 2). $F_{t2}$ will

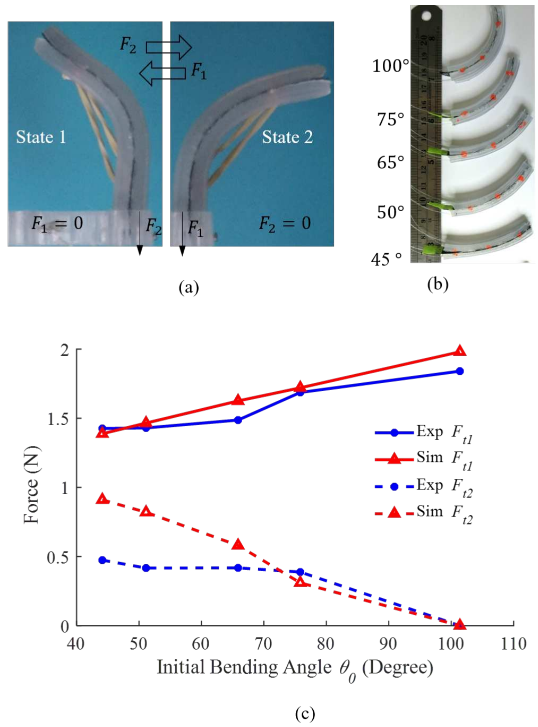


**Figure 4.14:** Characterization of the modules. (a) The two stable states with labeled forces for switching the states. (b) Five modules with different initial bending angles. (c) Simulation and experimental results for the triggering forces to switch the state.

be the triggering force from state 1 to state 2. Similarly, to switch from state 2 to state 1, we let $F_2 = 0$ while gradually increase $F_1$, and we record the triggering force $F_{t1}$.

Both $F_{t1}$ and $F_{t2}$ depend on the geometry of the module. We characterize the influence of the spine's initial angle $\theta$ on the switching force of an AB module and compare the experimental results with simulation results. The five different initial shapes are chosen to have an initial angle of 45°, 50°, 65°, 75° and 100° (Fig. 4.14b), since we use different beakers available to us to fabricate the spines. All of them are fabricated from a flat shape with the same dimensions. In the experiments, a force testing stand (ESM303 stand with M5-2 force gauge, MARK-10) is used to drag the corresponding cable slowly (100 mm/min) until the states are switched and the maximum force during the process is recorded as the triggering force. A complete testing process can be find in the supporting video.

The simulation results and the experimental results are plotted in Fig. 4.14(c). As the initial bending angle $\theta_0$ increases, $F_{t1}$ increases and $F_{t2}$ decreases, meaning it becomes more and more difficult to switch from state 2 to state 1, while it is easier to switch from state 1 to state 2. $F_{t2}$ is almost zero when $\theta = 100°$, suggesting the module becomes monostable with only the stable state 2 since it does not require a force to switch to state 2. The experimental and simulation results match each other with a mean error of 0.15 N. The relative large error for $F_{t2}$ with 45° and 50° might be due to the friction force between the cable and the channel, since we use a discrete channel instead of a continuous one.

### 4.3.4 Application

To demonstrate the usefulness of the proposed strategy, we develop a soft robotic gripper with two modules as the fingers and a jumping robot with a single module. In this section, we describe the design and experiments for these two robots.

#### A Soft Gripper with Two Bistable Bending Modules

For the gripper, we design the two fingers as two AB modules (Fig. 4.15(a)) to make it difficult to open while easy to close so that it can hold weights without additional energy input or hold heavier weights with some additional energy. We actuate the two fingers with TCAs as tendons, with each finger having two TCAs (TCA1 and TCA2 for left finger, and TCA3 and TCA4 for right finger). Each TCA has a length of 100 mm. Considering the actuation force that can be generated by a TCA as well as the required triggering force for AB modules obtained from the characterization, we choose $\theta = 50°$ for each finger. The two fingers are attached to a rigid base to fix their locations. The final gripper except the base weighs about 4.2 g, but it can hold 34 g, more than eight times its own weight.

Assume the gripper is initially open, we can close the gripper by applying a 1.5 A current to TCA2 and TCA3 for 0.8 s. To open the gripper, we can apply 1.5 A to TCA1 and TCA4 for 1.5 s. We demonstrate that the gripper can hold a weight of 15 g without energy input and hold 34 g if we apply 0.2 A to TCA2 and TCA3. It can potentially hold more when we applied a larger current. However, a gripper using traditional bending modules as fingers cannot hold the 34 g weight even when a current of 0.5 A is applied to TCA1 and TCA3 (see the supporting video). We record the temperature of the gripper using a thermal camera (E8, FLIR Systems, Inc), and the image with the highest temperature (45.3°C) is shown in the inset of Fig. 4.15(a).

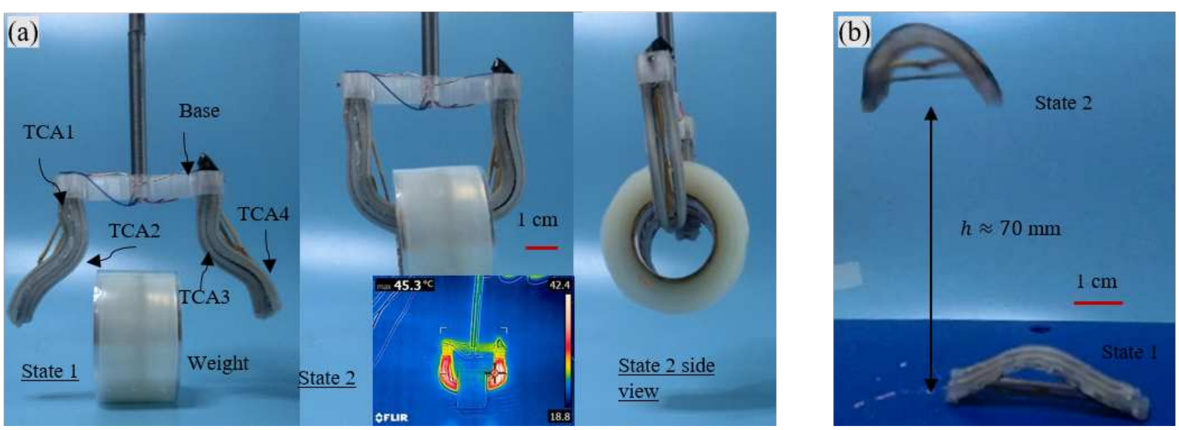


**Figure 4.15:** The applications. (a) Gripping 34g with the actuated TCAs (b) The jumping experiment.

### A Soft Jumping Robot with One Bistable Bending Module

To demonstrate the capability of fast motion, we design a soft jumping robot with one bistable bending module. It's in general more difficult to achieve jumping for a soft robot than a rigid one because a soft robot deforms when contacting the ground, absorbing a certain amount of energy. This difficulty, on the other hand, allows soft robots to withstand impact forces to protect them from damage. Here we demonstrate our soft robot can achieve a dynamic jumping motion relying on a sudden release of the stored energy.

To achieve a larger jumping height, we have the following design strategy: 1) decrease energy lost in contact with ground; 2) store more energy for jumping. To decrease energy lost in collision, one side of the soft body is removed to make the stiffer spine contact with the ground during take-off. Since the stored energy for jumping is positively related to spine deformation, the spine with a thickness of 0.5 mm and an initial angle of 75° is used.

For jumping experiments, we manually set the module to state 1 and apply a current of 2.5 A to the TCA for 0.3 s. A high-speed camera is used to record the jumping process and analyze the jumping height from the recorded video. The maximum jumping height for the robot is around 70 mm, which is twice of its length in state 1. In the experiments, the module needs to be manually set to the state 1, but this can be fixed by keeping the other part of the soft body removed previously. In this case, the robot's jumping height will be reduced as the weight increases, and the soft body will contact the ground during jumping.

## 4.4 Chapter Summary

In this chapter, when embedding TCAs with free strokes into a soft body to build soft robots, we can achieve versatile, programmed motion, compared with previous work 19,21,47. We demonstrate individual modules for 2D bending, twisting, and 3D bending motion by properly arranging the TCAs in the soft bodies. By concatenating the individual modules, we build a first-ever miniature soft robotic arm actuated by TCAs. We demonstrate pick-and-place operations using the soft robotic arm. More complicated motion can be potentially achieved by arranging TCAs in other desired shapes. By leveraging the resistance self-sensing capability, we realized an Innervated soft bending finger that can be automatically triggered by external stimuli and move to the desired angle with closed-loop control. Even if the environmental disturbance (temperature, flow condition) is applied, the finger can still achieve the precise motion required.The bistable module actuated by TCAs can hold more force and realize fast motion. We have demonstrated a strong gripper and a jumping robot driven by the TCAs using the bistable modules.

# Chapter 5

# Modeling of TCA-driven Soft Robots

Soft robots have been intensively investigated for manipulation and locomotion in recent years. However, the current state of soft robotics has significant design and development work but lags in modeling and control due to the difficulty in modeling them. In this chapter, we present a physics-based analytical framework to model soft robots driven by Twisted-and-Coiled Actuators (TCAs), an artificial muscle that can be arranged in arbitrary shapes in the soft body of a soft robot to achieve programmable motions. The framework can model 1) the complicated routes of multiple TCAs in a soft body, and 2) the coupling effect between the soft body and the TCAs during their actuation process. When not actuated, a TCA in the soft body is an antagonistic elastic element that restrains the magnitude of the motion and increases the stiffness of the robot. By stacking several modules together, we simulate the sequential motion of a soft robotics arm with three-dimensional bending, twisting, and grasping motion. The presented modeling and simulation approach will facilitate the design, optimization, and control of soft robots driven by TCAs or other types of artificial muscles.

To address the challenges, we have used Cosserat rod model that can accurately model continuum robots [61, 91] to model TCA-driven soft robots [27]. But the previously proposed method only considered the simplest case where only a straight TCA is actuated to drive a soft manipulator. However, the real cases could be more complicated with one example of a soft robotic arm shown in Fig. 5.1(a) [86]. The robotics arm has three serially connected modules: a 3D bending module, a twisting module, and a gripper. Our previous work cannot handle such a robotic arm correctly [121].

First, when three TCAs are arranged in parallel inside a soft body, the actuated TCA will need to overcome the antagonistic stretching force of the other two unactuated/passive TCAs, resulting in a much less actuation magnitude. Second, the twisting module has a TCA arranged in a helical route and this is usually difficult to model using conventional simplified methods such as the piece-

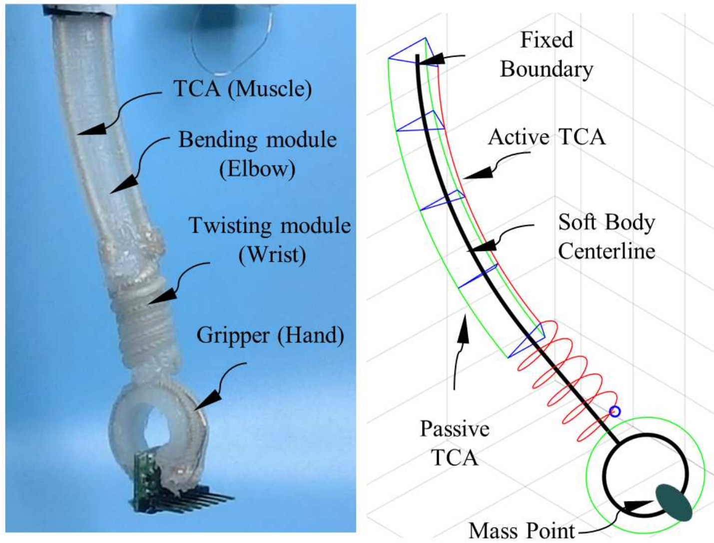


(a) (b)

**Figure 5.1:** (a) The TCA-driven soft robotics arm picks up a PCB board; (b) The simulated soft robotics arm.

wise constant curvature method. Third, several modules can be combined together to realized more complicated motions, introducing the coupling problem between neighboring modules.

## 5.1 Analytical Modeling

A soft body actuated by TCAs is modeled as a single Cosserat rod. In this section, we provide a brief overview on the system of ODEs of a Cosserat rod, and introduce how to incorporate an external load such as gravity, the actuation force from the artificial muscle, i.e., TCAs, and the coupling between the artificial muscle and the soft body.

### 5.1.1 Kinematics

In Cosserat theory, bodies are modeled as a collection of infinitesimal rigid bodies (IRBs) rather than point particles, and thus each IRB has both position and orientation rather than just position. For a given rod, we define the centerline, $s \in [0, L]$, as the curve passing through the centroids of all the cross sections where $L$ is the length of the rod in its reference configuration. At every point

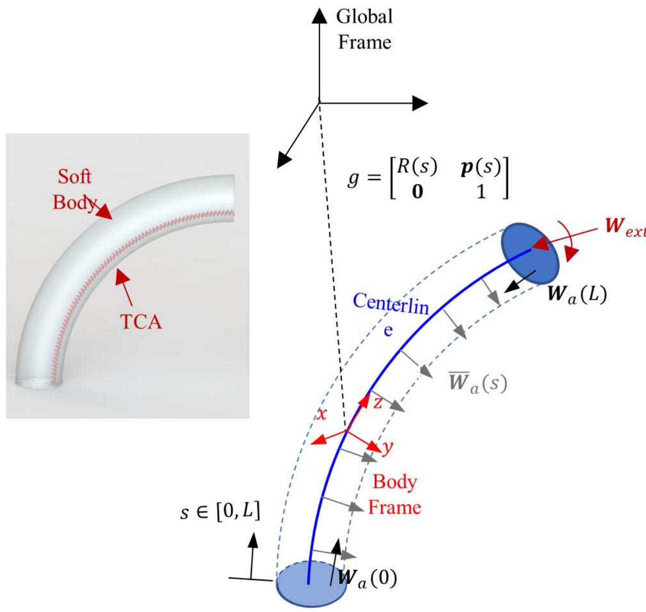


**Figure 5.2:** A soft body driven by a single artificial muscle and its corresponding diagram of the kinematics using the Cosserat rod theory. It shows the centerline $s \in [0,L]$ as the blue solid curve, the configuration $g$, and the body frame (in red) attached to a cross section.

$s$ along the centerline, we establish a body frame for the cross section. The $z$ axis of the frame is tangent to $s$, and the $x$ and $y$ axes are assumed to be aligned with the principal axes of the cross sections. Each body frame has a rotation and a translation relative to the global (fixed) frame. We describe the position and orientation of all the IRBs along the centerline using a homogeneous transformation matrix $g(s) \in SE(3)$.

$$g(s) = \begin{bmatrix} R(s) & p(s) \\ 0 & 1 \end{bmatrix} \tag{5.1}$$

where $R(s) \in SO(3)$ is a rotation matrix and $p(s) \in \mathbb{R}^3$ is the position vector.

With $g(s)$, the system of ODEs for the kinematics and statics can be written as [91]:

$$g' = g\hat{\xi} \tag{5.2}$$

$$W = K\Delta\xi \tag{5.3}$$

$$\bar{W}_e - ad_{\xi}^T W + W' = 0 \tag{5.4}$$

where $'$ is the derivative with respect to $s$, and $\xi = [u^T, v^T]^T \in \mathbb{R}^6$ is the spatial twist (strain) representing the relative configuration change between adjacent cross sections along the centerline, with $u, v \in \mathbb{R}^3$ the angular and linear strain component, respectively. The 'hat' operator $\widehat{\cdot}$ is a mapping from $\mathbb{R}^3$ to $\mathfrak{so}(3)$ or $\mathbb{R}^6$ to $\mathfrak{se}(3)$, e.g., $\widehat{\xi} = \begin{bmatrix} \widehat{u} & v \\ 0 & 0 \end{bmatrix}$, $\bar{W}_e = \begin{bmatrix} \bar{l}^T, & \bar{f}^T \end{bmatrix}^T$ is the distributed external wrench with $\bar{l}, \bar{f} \in \mathbb{R}^3$ as the moment, force per unit arclength applied to the centerline in the body frame, $ad_{\xi} = \begin{bmatrix} \widehat{u} & 0 \\ \widehat{v} & \widehat{u} \end{bmatrix}$ is adjoint representation of the spatial twist $\xi$. $W = \begin{bmatrix} m^T, & n^T \end{bmatrix}^T$ is the internal wrench in the body frame with $m, n \in \mathbb{R}^3$ as the internal moment and force in the body frame. $K_{bt} = \mathbf{diag}[EI_x, EI_y, GJ]$ is the diagonal stiffness matrix for bending and torsion, and $K_{se} = \mathbf{diag}[GA_t, GA_t, EA_t]$ is the diagonal stiffness matrix for shear and extension. $E$ and $G$ are the Young's modulus and shear modulus, respectively. $A_t$ is the cross section area of the rod, $I_x$, $I_y$ are the second moment of area with respect to $x$ and $y$ axis, and $J = I_x + I_y$ is the polar moment of inertia of the rod's cross section about its centroid.

We decompose (5.2) into the angular and linear component to facilitate our numerical simulation using non-unit quaternion, and rewrite the system of ODEs using $R$, $p$, and $\xi$ as state variables

$$R' = R\widehat{u} \tag{5.5}$$

$$p' = Rv \tag{5.6}$$

$$\xi' = K^{-1}(ad_{\xi}^T K\Delta\xi - \bar{W}_e) + \xi'^* \tag{5.7}$$

External distributed wrench comes form the artificial muscle and gravity

$$\bar{W}_e = \bar{W}_{grav} + \bar{W}_a \tag{5.8}$$

where

$$\bar{W}_{grav} = \rho A \begin{bmatrix} 0_{3\times 1} \\ R^T g_r \end{bmatrix}, \tag{5.9}$$

is the distributed gravitational force in the global frame, and $g_r = [0, 0, -9.81]^T$ is the gravitational vector. $\bar{W}_a$ is the distributed wrench due to the artificial muscle TCA's tension force.

Note that the TCA-driven soft robots is different from tendon-driven robots since a TCA has two anchoring points on the body and the wrench exerted on a robot is considered as an internal wrench that does not influence the segment where the TCAs is not embedded as shown in Fig. 5.2. Therefore, the initial and distal boundary conditions need to be adjusted as

$$W(0) = W_0 - W_a \tag{5.10}$$

$$W(L) = W_a + W_{ext} \tag{5.11}$$

where $W_{i,0}$ is the initial internal wrench if the TCA is connected to the ground, $W_a$ is the sum of point wrench exerted by TCAs, and $W_{ext}$ is the sum of explicit external wrench applied to the distal end.

### 5.1.2 TCA Force Mapped to the Rod

A TCA is embedded into a soft body by running through a channel in the soft body and the channel is created during the soft body's fabrication process [86]. The friction force between the TCA and the soft body is negligible. We assume that the TCA is able to freely slide in the channels and the TCA only has axial loads (no bending stiffness). This derivation is general for any tendon-like artificial muscles.

In the following, we derive the wrench exerted by $i^{th}$ TCA to the centerline of the rod in the global frame

$$W^g_{a,i} = -F_a \begin{bmatrix} \widehat{p}_a t_a \\ t_a \end{bmatrix} \tag{5.12}$$

where the superscript $g$ indicates that the wrench is represented in the global frame. $F_a$ is the tension force in the TCA (positive if the TCA is stretched), $p_a = Rr_a + p$ is the position of the TCA in the global frame, and $r_a = [x_a, y_a, 0]^T$ is the position vector of the TCA in the body frame. $t_a = \frac{p'_a}{\|p'_a\|}$ is the unit tangent vector to the TCA, where

$$p'_a = \frac{\partial(Rr_a + p)}{\partial s} = R(v - \widehat{r}_a u + r'_a) \tag{5.13}$$

To get the distributed wrench, we take the derivative of (5.12) with respect to $s$.

$$\bar{W}^g_{a,i} = \frac{\partial W^g_a}{\partial s} = -F_a \begin{bmatrix} \widehat{p}'_a t_a + \widehat{p}_a t'_a \\ t'_a \end{bmatrix} - F'_a \begin{bmatrix} \hat{p}_a t_a \\ t_a \end{bmatrix} \tag{5.14}$$

Note that $\widehat{p}'_a t_a = 0$

$$\bar{W}^g_{a,i} = -F_a \begin{bmatrix} \widehat{p}_a t'_a \\ t'_a \end{bmatrix} - F'_a \begin{bmatrix} \widehat{p}_a t_a \\ t_a \end{bmatrix} \tag{5.15}$$

Since the balance equation (5.7) is established in the body frame. We need to map the distributed wrench and point wrench back to the body frame using the adjoint transformation and note that $F' = 0$, $\widehat{p}_a - \widehat{p} = \widehat{(Rr_a)} = R\widehat{r}_a R^T$ leading to:

$$\bar{W}_{a,i} = Ad^T_g \bar{\bar{W}}^g_a = -F_a \begin{bmatrix} \widehat{r}_a R^T t'_a \\ R^T t'_a \end{bmatrix} \tag{5.16}$$

where $Ad^T_g = \begin{bmatrix} R^T & -R^T\widehat{p} \\ 0 & R^T \end{bmatrix}$ is the transpose of adjoint transformation.

We also need the following to calculate the explicit form of the cable wrench, and represent it with strains [61]

$$t'_a = -\frac{(\widehat{p'}_a)^2}{\|p'_a\|^3} p''_a$$

$$p''_a = R(\widehat{u}(v - \widehat{r}_a u + r'_a) + v' - \widehat{r}_a u' - \widehat{r}'_a u + r''_a)$$

Therefore $R^T t'_a$ term in Eq. (5.16) that appears both in moment and the force term is

$$\begin{aligned} R^T t'_a &= -R^T \frac{(\widehat{p'}_a)^2}{\|p'_a\|^3} p''_a \\ &= Pv' - P\widehat{r}_a u' + b - P(\widehat{r}'_a u - r''_a) \end{aligned} \tag{5.17}$$

where $b = P(\widehat{u}(v - \widehat{r}_a u + r'_a)), P = -R^T \frac{(\widehat{p'}_a)^2}{\|p'_a\|^3} R$

We can split $\bar{W}_a$ and $W_a$ into components that do and do not depend on $\xi'$

$$\bar{W}_{a,i} = \bar{A}_i \xi' + \bar{B}_i \tag{5.18}$$

where

$$\bar{A}_i = -F_a \begin{bmatrix} -\widehat{r}_a P \widehat{r}_a & \widehat{r}_a P \\ -P\widehat{r}_a & P \end{bmatrix}, \bar{B}_i = -F_a \begin{bmatrix} \widehat{r}_a (b - P(\widehat{r}'_a u - r''_a)) \\ b - P(\widehat{r}'_a u - r''_a) \end{bmatrix}$$

Both $\bar{A}_i \in \mathbb{R}^{6\times 6}$ and $\bar{B}_i \in \mathbb{R}^6$ are independent of $\xi'$, but dependent on $\xi$. It is simple to use $\xi$ instead of $W$ as the state variables because of the dependence of $\bar{W}_a$ on $\xi$ and $\xi'$.

The ends of the TCAs are always fixed to the soft body, typically the ends. In this case, a TCA will exert a point wrench due to the tension. This can be written in the body frame as:

$$W_{a,i} = Ad_g^T W_{a,i}^g = -F_a \begin{bmatrix} \widehat{r}_a R^T t_a \\ R^T t_a \end{bmatrix} \tag{5.19}$$

If there are $n$ TCAs arranged in the soft body, the total distributed will be

$$\bar{W}_a = \bar{A}\xi' + \bar{B} \tag{5.20}$$

$$W_a = \Sigma_{i=1}^{n} W_{a,i} \tag{5.21}$$

where $\bar{A} = \Sigma_{i=1}^{n} \bar{A}_i$ and $\bar{B} = \Sigma_{i=1}^{n} \bar{B}_i$

.

### 5.1.3 TCA Model and Coupling to the Rod

The TCA's displacement and tension force are both coupled to the rod's deformation. The displacement of a TCA can be calculated from the positions of the TCA coupled to the soft body

$$\delta_a = \int_0^L \|p_a'\| ds - \int_0^L \|(p_a^*)'\| ds \tag{5.22}$$

where $\delta_a$ is the displacement of the TCA, and this is the difference of the TCA's arc length between the current configuration and the original configuration.

TCAs can be modeled using the Castigliano's Second Theorem (CST) due to its helical structure [123]

$$\delta_a = A_{cst}\Delta\bar{\theta}^{\mathsf{h}} + \frac{1}{K_{cst}} F_a \tag{5.23}$$

where $\Delta\bar{\theta}^{\mathsf{h}}$ is the unit untwisting of a twisted fiber used to fabricate TCAs with respect to temperature. A polynomial can be used to approximate $\Delta\bar{\theta}^{\mathsf{h}} = -0.0161T^2 + 0.3338T - 7.7311$ based on our previous work, and

$$\frac{1}{K_{cst}} = l_t \left( \frac{r^2 \cos^2 \alpha}{G_t J_t} \right), A_{cst} = l_t r \cos \alpha$$

$r$ is the TCA's diameter, $l_t$ is the twisted fiber's length, $A_t$ is the cross section area of the twisted fiber, and $\alpha$ is the pitch angle of the TCA. Note that based on the small deformation assumption,

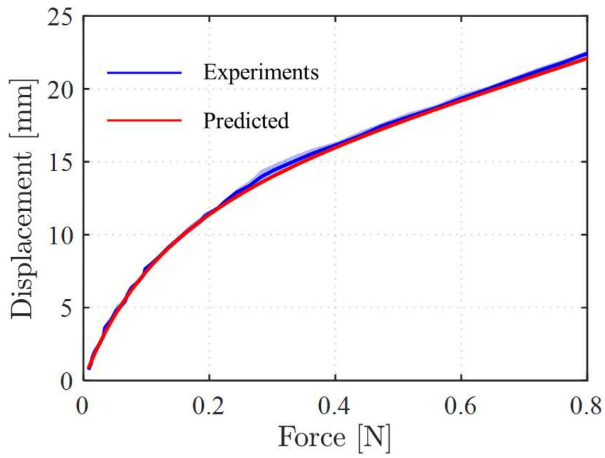


**Figure 5.3:** The experimental and predicted results of the passive displacement of a TCA with respect to external force.

all the variables are close to their values of the reference states, for example, $\alpha \approx \alpha^*$. We also ignored the bending, shear, and extension strain of the TCA for simplicity.

However, when a TCA is not actuated, it will act as a nonlinear mechanical spring. Its share modulus $G_t$ gradually increases with respect to the TCA's stretching deformation, resulting in increasing stiffness for a passive TCA. We conduct experiments to measure the stretching force of a TCA with its deformation and fit $G_t$ using a second-order polynomial with respect to the TCA's external force, $G_t = 37.58Fa^2 + 111.33Fa + 0.85$ MPa. With such a fitting, the predicted passive displacement of a TCA of 55 mm is pretty close to the experimental results as shown in Fig. 5.3.

Combining (5.22) and (5.23), we can have an compatibility equation for the TCA

$$\int_0^L \|p_a'\| ds - l^* - (A_{cst}\Delta\bar{\theta}^{\mathsf{h}} + \frac{1}{K_{cst}} F_a) = 0. \tag{5.24}$$

Plugging (5.20) in (5.8) and (5.7), and rearrange to make $\xi'$ explicit, we have

$$\xi' = (K + \bar{A})^{-1}(ad_{\xi}^{T} K\Delta\xi - \bar{B} - \bar{W}_{grav} + K\xi'^{*}). \tag{5.25}$$

Rearranging (5.10) and (5.11), we can obtain

$$\xi(0) = \xi_0 - K^{-1}W_a \tag{5.26}$$

$$\xi(L) = K^{-1}(W_a + W_{ext}) + \xi^* \tag{5.27}$$

where $\xi_0$ is the initial strain if the TCA is connected to the ground.

A single module driven by a TCA can be fully defined by the system of ODEs (5.5), (5.6) and (5.25) with compatibility equation (5.24) and boundary condition (5.26) and (5.27).

## 5.2 Numerical Implementations

We use the method described in Section 3.4.2, to avoid truncation error during the integration of the rotation and a shooting method is used to solve the BVP.

### 5.2.1 Shooting method Solving Connected Rods

TCA actuation force $F_a$ is an implicit variable that is required both for the boundary condition and for the ODEs. A shooting method can be used to solve the boundary value problem with the unknown/implicit force. The method starts from guessing the initial strain $\xi_0$ and the actuation forces $F_a$ for the TCAs using the trust-region-dogleg method. Then the ODEs are integrated from $s = 0$ to $s = L$ using a standard library code (e.g., $ode45$ in Matlab), during which the distributed wrench and point wrenches will need to be calculated. Finally, the boundary conditions and the compatibility equation are checked. If the residual error $\varepsilon$ as in (5.28) is within the specified tolerance, the algorithm stops and returns the results; otherwise, new guess values will be generated and the process repeats until the boundary conditions and the compatibility equations are satisfied.

$$\varepsilon = \begin{bmatrix} \int_0^L \|p_a'\| ds - l^* - (A_{cst}\Delta\bar{\theta}^{\mathsf{h}} + \frac{1}{K_{cst}}F_a) \\ K^{-1}(W_a + W_{ext}) + \xi^* \end{bmatrix} \tag{5.28}$$

If two or more rods are serially connected, a piece-wise integration needs to be implemented to solve them together as shown in Algorithm 2. For this case, we only guess the very first rod's initial condition to make sure that the very last rod's distal boundary condition and the compatibility equation for each TCA are satisfied.

---

**Algorithm 2:** Solving serially connected modules

---

**Input:** Temperature vectors of the TCAs
Initiate parameters;
Setup Initial boundary conditions $g_0$;
**for** $T = T_0 \rightarrow T_{max}$ **do**
  **while** $\varepsilon > Tol$ **do**
    Guess $\xi_0$ for the first rod;
    Adjust the initial boundary Eq. (5.26);
    Integrate the first module Eqs. (5.5), (5.6) and (5.25);
    Adjust the distal boundary condition to include point forces Eq. (5.27);
    Use the distal boundary of first module as the initial boundary condition of the second module;
    Adjust the initial boundary Eq. (5.26);
    Integrate the second module Eqs. (5.5), (5.6) and (5.25) ;
    Return the error of the compatibility equations of all TCAs, and the distal boundary condition of the second module Eq. (5.28).
  **end**
  Visualization;
**end**

---

## 5.3 Results

We use the 3D bending module and the soft robotics arm as examples to illustrate the simulation of a single module and serially connected modules. We use Young's modulus $E = 0.125$ MPa and $G = E/3$ for the soft body made of Ecoflex-30 (Smooth On Inc.). The 3D bending module and twisting module are simplified as a rod with a circular cross section that has a diameter of 4.5 mm. The gripper's cross section is a rectangular shape of $3 \times 6$ mm.

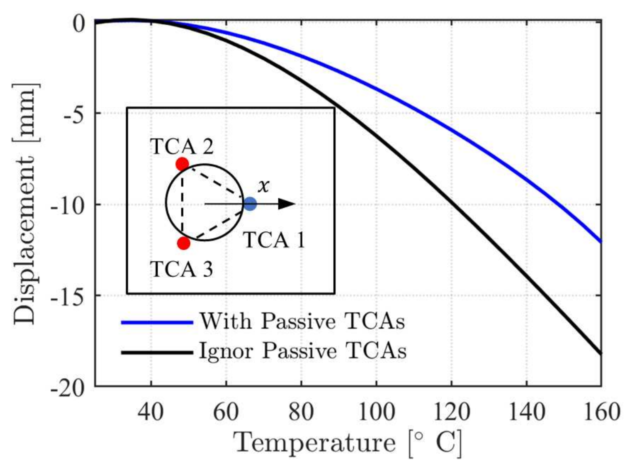


**Figure 5.4:** The comparison between the cases with and without considering the antagonistic forces from the passive TCAs. The inset shows the cross section of the 3D bending module and the actuated TCAs.

### 5.3.1 Simulation of a Single 3D Bending Module

The 3D bending module has three TCAs located 4 mm from the center at the angle of 0, 120, and 240° as shown in the inset of Fig. 5.4. The length of the soft body and the TCA is 45 mm. We simulate the case that TCA 2 and 3 are actuated, and TCA 1 serves as a passive TCA that generate antagonistic forces. Figure 5.4 shows that the bending magnitude without considering the passive TCAs is more than 40% larger than the case considering the passive TCAs' antagonistic forces. The error could be even larger when a stiffer material is used or the module has different geometry parameters. The results suggest that antagonistic force cannot be ignored if multiple TCAs are embedded in the module.

With this model, we can also simulate the variable stiffness effect of the 3D bending module when all three TCAs are equally actuated at the same time. Figure 5.5 shows the displacement of the module with respect to a force along $x$ direction. When the temperatures of the 3 TCAs are increased from 75 to 125 °C, the same amount of force can cause much less displacement.

### 5.3.2 Simulation of the Soft Robotics Arm

The soft robotics arm shown in Fig. 5.1 is realized by serially stacking a twisting module and a gripper (pre-curved 2D bending module) on the top of the 3D bending module [86]. The TCA in the twisting module is wrapped around a soft cylinder (16 mm) in a helical shape located 3.5

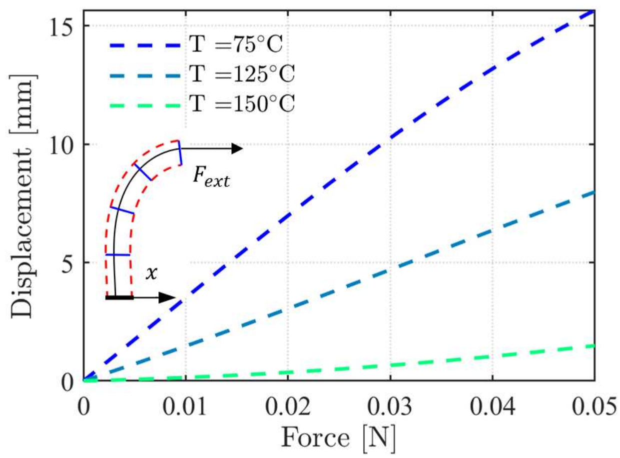


**Figure 5.5:** The 3D bending module displaces differently When a horizontal force is applied at the top, demonstrating the variable stiffness function of the module. The inset shows the direction diagram of the applied force on the module.

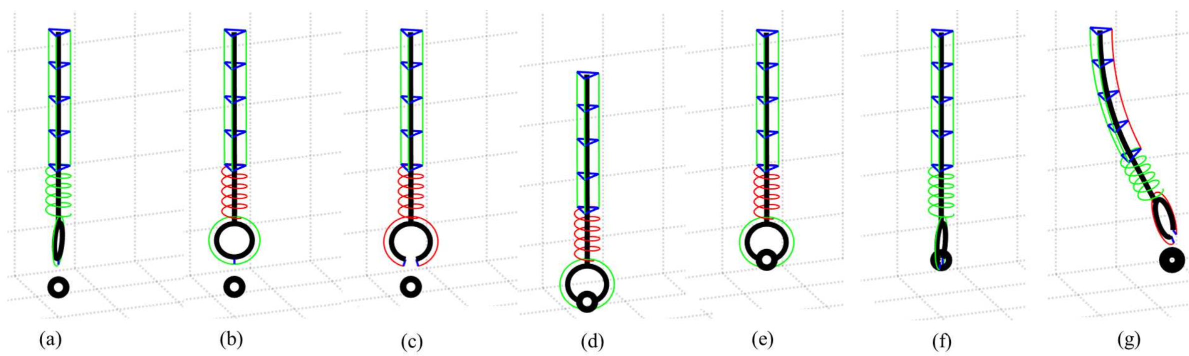


**Figure 5.6:** The simulation of a pick-and-place process of the soft robotics arm. The red and green lines represent the active and passive TCAs, respectively. The centerlines of the soft bodies are represented by the thicker black lines. The blue lines illustrate the cross sections of the 3D bending module. (a) The initial straight configuration. The object is 10 mm under the gripper. (b) The twisting module rotates the gripper to align it with the object. (c) The gripper opens. (d) The arm is lowed and the gripper closes to pinch the object. (e) The arm lifts the object. (f) The twisting module is deactuated to rotate the gripper to its original orientation. (g) The bending module bends to $x$ direction, and the gripper opens again to release the object to a different location. A video can be found: https://youtu.be/MrTmZ8F50rs

mm from the center. There are total 5 rounds of TCAs and the two ends of the TCA is fixed on the cylinder. The gripper has a circular body shape and is normally closed, which means When the TCA contracts, the gripper can open itself. Therefore it holds objects when the TCA is not actuated and the TCA is located 2.5 mm from the center of the gripper's cross section.

Due to the small size of the gripper, only the 3D bending module and the twisting module are treated as serially connected modules that are solved together. The weight of the gripper and the object grasped by the gripper are considered as an external load that can be mapped to the tip of the twisting module.

Figure 5.6 shows the simulation of the robotics arm that conducts a pick-and-place task. First, the robotics arm is at its initial straight configuration. Then the twisting module rotates the gripper to allow it to align with the object. The gripper opens to pinch the object. The 3D bending module bends to the desired direction, and then the object is released by the gripper.

## 5.4 Chapter Summary

In the chapter, we use TCA-driven soft robots as an example to present a general analytical model using the Cosserat rod theory for soft robots driven by an artificial muscle. The model solves the coupling implicit force of the artificial muscles with deformation of the soft body, and considers the antagonistic force of passive artificial muscles. The simulation scheme for serially connected modules is also presented for simulating more general and complicated cases.

# Chapter 6

# TCA-driven Shape Morphing Robots

In this chapter, we propose a TCA-driven shape morphing robot that can adapt to the surrounding environment by correspondingly changing its body shapes. The shape morphing robot has two states: one is soft, and one is rigid. When it is in a soft state, it can be driven by TCAs to change its shape like a soft robot. Once it arrives at a target shape it starts to hold the shape, and eventually becomes rigid. It has many promising applications including human-machine interface, deployable structures, self-assembly, and in particular, robotics [124].

Robots with shape morphing capabilities can leverage the same mechanical mechanism to locomote in different environments or extend their dynamic envelopes. Examples include aircraft with morphing wings that can successfully maneuver to land on a human hand with improved dynamics performance [125], and a robot equipped with passively morphing wheels that can roll on a flat surface and passively morph into whegs to negotiate obstacles [126].

A structure with shape morphing capabilities should have two essential elements: 1) controllable stiffness, so it can be rigid before and after the shape change and soft in-between; 2) an actuator to provide sufficient force and displacement to achieve the desired shape.

These two elements have been separately studied extensively. Stiffness tuning between soft and rigid is conventionally achieved in a system level by the variable stiffness of mechanisms [127] or employing Electro-rheological (ER) [128] and Magneto-rheological (MR) fluids [129]. However, it can be more easily achieved at a material level through the use of thermally responsive materials such as shape memory polymers (SMP), conductive elastomer, phase-changing alloys, or low-melting-point alloys (LMPA). Shape memory alloy (SMA) has been widely used for actuation to enable shape morphing, such as a shape-morphing fabric that can contract to a certain length and hold that position [130]. Tendons driven by external motors have also been widely used to achieve reliable, cheap, and easy control of the soft body for shape morphing, but electrical motors, stiff and heavy, might limit bending or shape changing of the soft body [131]. Hydraulic or pneumatic actuation based on modular inflatable chambers can generate relatively larger forces and faster responses, but they require external parts to generate pressure, restricting their applications in small robots [132].

## 6.1 Shape Morphing Module

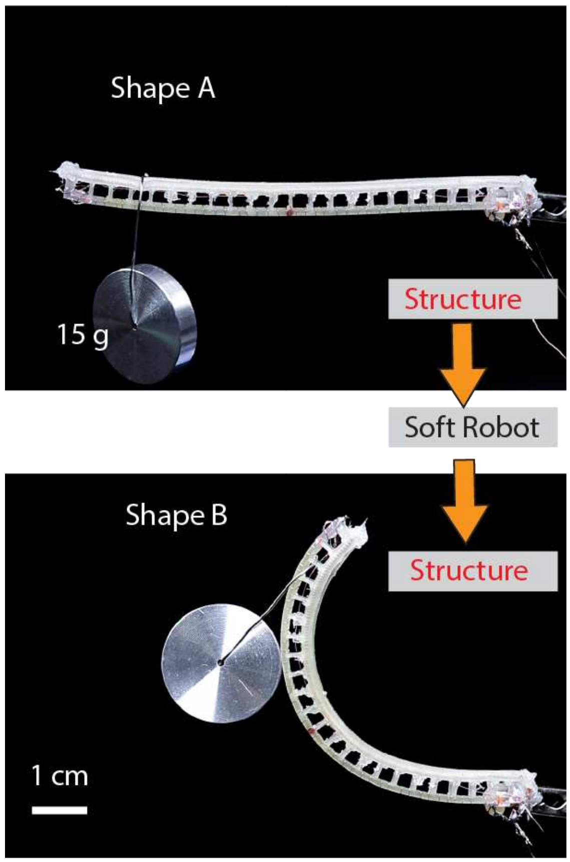


**Figure 6.1:** The shape morphing module can morph into different shapes .

We leverage shape memory polymer (SMP) for the variable stiffness element and TCAs as actuators. As shown in Fig. 6.1, a 15 g weight is placed at the tip of the module to show that the module can hold different shapes and stay at the shapes as a rigid structure for various applications.

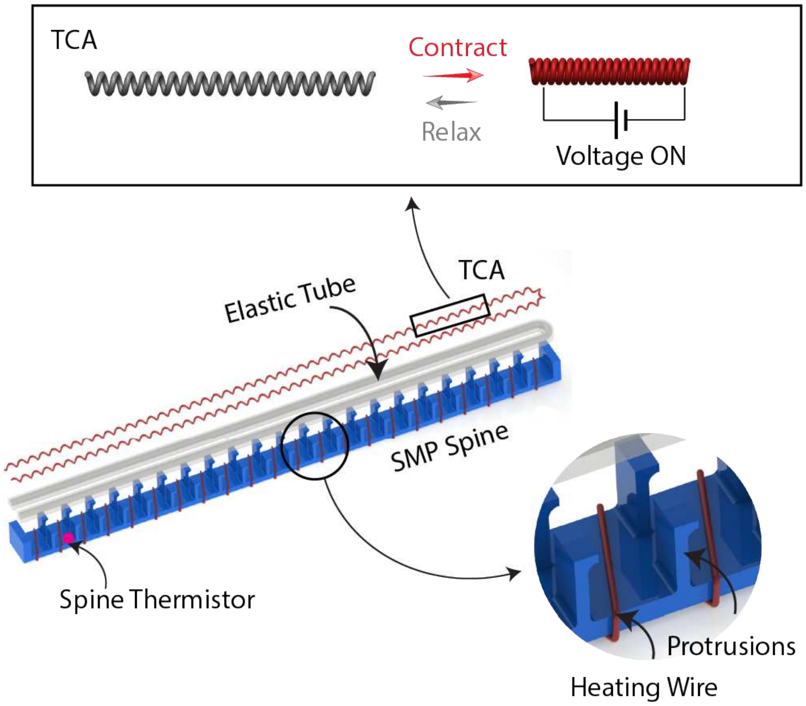


**Figure 6.2:** The schematic of the shape morphing module.

### 6.1.1 Shape Morphing Module Working Principle

We demonstrate the shape-morphing concept by fabricating a 115×6.5×5 mm bending module that can morph and hold different angles as structures. As shown in Fig. 6.2, such a module requires two basic elements: a variable-stiffness element and an actuator together with sensors for actuate control. Our design consists of a variable stiffness spine casted using shape memory polymer (SMP) as the variable stiffness element, and a soft actuator twisted-and-coiled actuator (TCA) that can serve both as an actuator and a sensor at the same time. The stiffness of the spine is controlled by regulating its temperature through a resistance wire wrapped on the spine. A thermistor is embedded into the spine for controlling the spine's temperature, thus stiffness. The TCA is enclosed in a soft silicone tube that is arranged into a U shape and attached to the protrusion of the spines. The purpose of the protrusion is to decouple the thermal interference of the VS spine and the TCA. Electrical wires are connected to the ends of the resistance wires and the TCAs to apply electricity.

### Shape Morphing Process

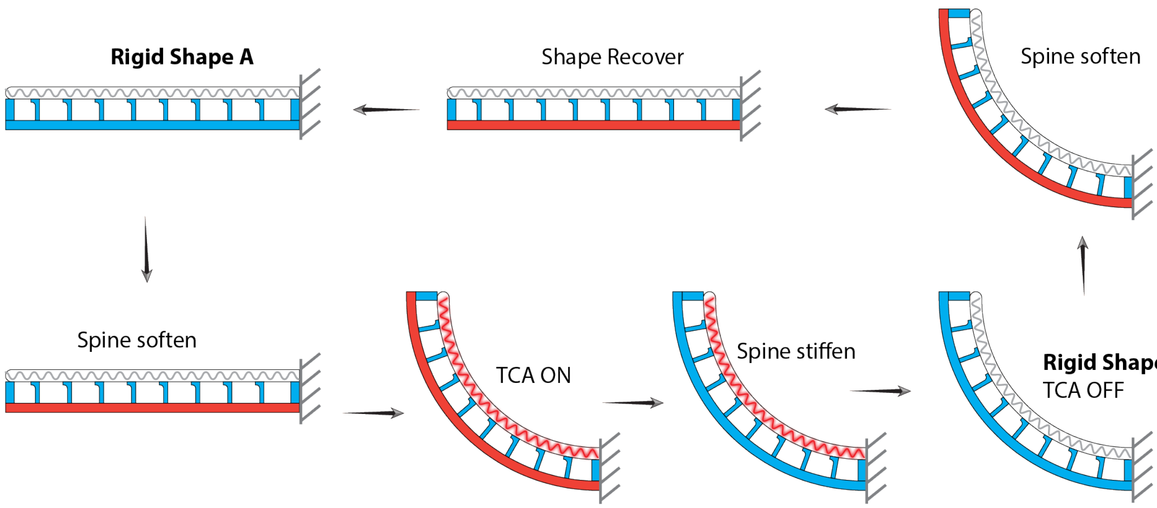


**Figure 6.3:** The shape morphing process of the module.

Basically, the module switches its state between rigid structures and a soft robot. In the states of rigid structures, the module can function with rigidity and strength, while in the state of a soft robot, the module can be controlled to realize different shapes with flexibility.

Fig. 6.3 shows the morphing process of the module. Initially, the module has a shape A. First, we soften the spine by applying electricity on the resistance wire wrapped on the spine. Once the temperature of the spine is over it's glass transition temperature, the TCA will be actuated to deform the module to a specific shape. After that, the spine will cool down after removing the voltage on the resistance wire while the TCA is still active to maintain the shape until the spine's rigidity is fully recovered. The module can stay at shape B as a rigid structure for various applications. The spine can be heated to recover to the Shape A using its shape memory effect.

### Fabrication

All the SMP parts are fabricated by casting the SMP into silicone molds that are fabricated from 3D-printed parts (Prusa, SL1S). To make the shape more accurate, we always want to enclose the SMP in a closed chamber. We either directly fabricate the mold and split it into two half to take the cured SMP parts out or fabricate the mold as two parts and assemble them together. The SMP epoxy is fabricated by mixing a standard epoxy resin Epon 828 (Momentive Performance Materials Inc.) with 6wt% Diethylaminopropylamine as a curing agent.

The mixture will turn viscous when it is at room temperature. Therefore, the mixing is conducted in 60 °C for 5 mins using a magnet stirrer with 500 rot/min. We pour the mixture SMP into the mold that is heated to 60 °C , and then degas it in a vacuum oven 3 times. Then the SMP is cured at 60°C for 10 hours in silicone molds. For the twisting module that requires an embedded resistance wire at its middle rod, we use a 3D printed jig to hold the resistance wire in the center of the middle rod while the SMP is curing.

Assembling TCAs and the SMP Parts The TCA is first cut and connected to two copper wires at its ends. Then we run the TCA into a silicone tube made of Eco-flex 50. After that, the TCA is trained and shrinks into the tube. The two ends of the TCA are fixed to the tube by using silicone glue. Then the TCA with tube will be glued to the protrusions of the SMP parts using a jig as shown in Fig. 6.4.

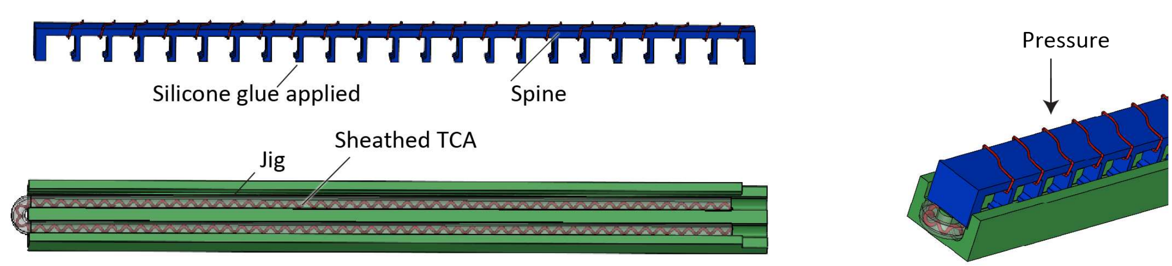


**Figure 6.4:** The fabrication of the 2D bending module.

### 6.1.2 Characterization

The technology underpinning the morphing module is the coordination of the TCA and the SMP spine. Especially, during the soft robot state. To allow the module to bend to different angles, the control of the morphing process involves controlling the temperature of the spine and controlling the actuation of the TCA.

### 6.1.3 Characterization of the Shape Memory Polymer

We conducted a dynamic mechanical analysis (DMA) for the SMP to measure the modulus of the SMP with respect to temperature. The specimen has a dimension of 65x10x3 mm and is tested using 3-point bending method using an SII Exsta 6000 DMA tester.

Fig. 6.5 shows the tested results. When the temperate is above 110 °C, the modulus of the SMP is below 50 MPa, which is close to the hyperelastic material used for soft robots, e.g., EcoFlex-30. When the temperature is below 80 °C the SMP recovers its rigidity.

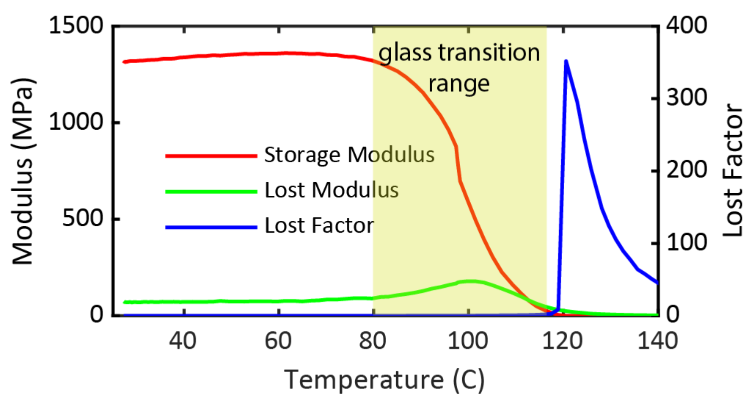


**Figure 6.5:** The DMA test results that show the glass transition range of the SMP.

Fig. 6.6 shows the spine's temperature changes with respect to time. The spine is heated using 25V and the temperature of the spine is maintained using 9.5 V for 10s. We compared two different cooling conditions under room temperature. It shows the natural cooling can cool the spine to 80 °C in 25 s and the force cooling with a fan (1m/s) can cool the spine in 12 s.

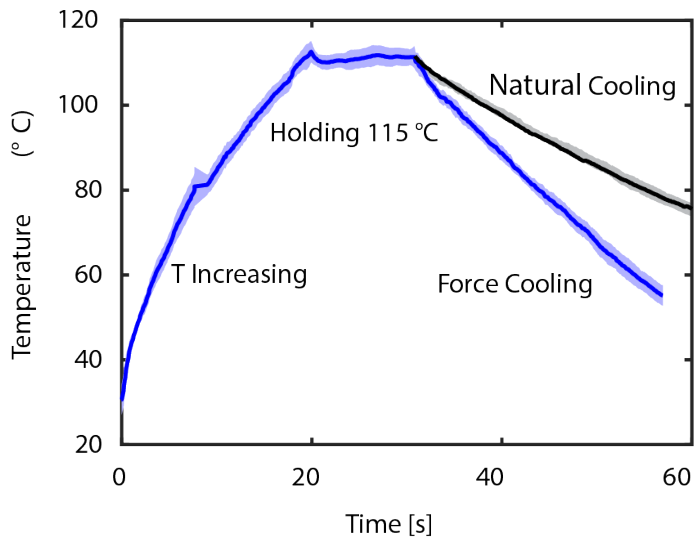


**Figure 6.6:** The temperature of the spine during a morphing process.

## 6.2 Control of the Module

### 6.2.1 Open-loop Control

The actuation of the shape-morphing module is also characterized when it is at the soft-robot state. The fast response of the TCA allows the module to move to the largest bending angle (240º) in one second with 25 V applied (Fig. 6.7). The bending angle is defined as the angle of the spine's tip from the horizontal line. However, sophisticated control is required for the sheathed TCA to steadily hold the desired angle (< 5º vibration) during the stiffening process of the spine. Because keeping contracting the TCA when the spine becomes rigid damages the TCA permanently. While keeping relaxing TCA during stiffing the spine causes an inaccurate holding angle, though it does not damage the actuator.

A constant voltage can be applied until the steady state before stiffening the spine, which can realize a simple successful control without extra control algorithms and sensors. Fig. 6.8 shows that small constant voltages are applied to the sheathed TCA to test the bending angles of the modules with respect to time. It is considered as the steady state when the bending angle changes less than 3º in 20 s. The circles in Fig. 6.8 represent the starting point of the steady state, and the

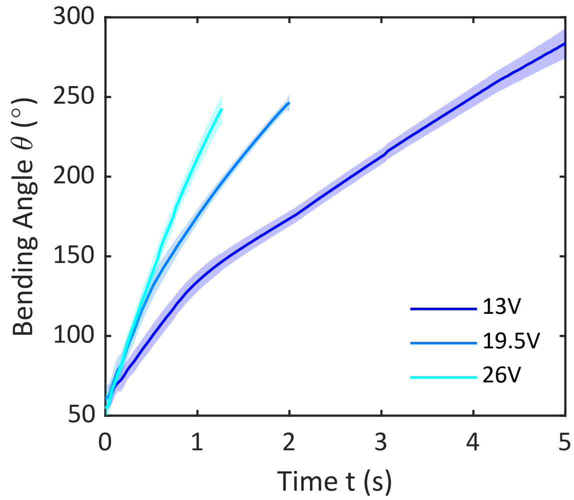


**Figure 6.7:** The fast actuation of the module when the spine is soft.

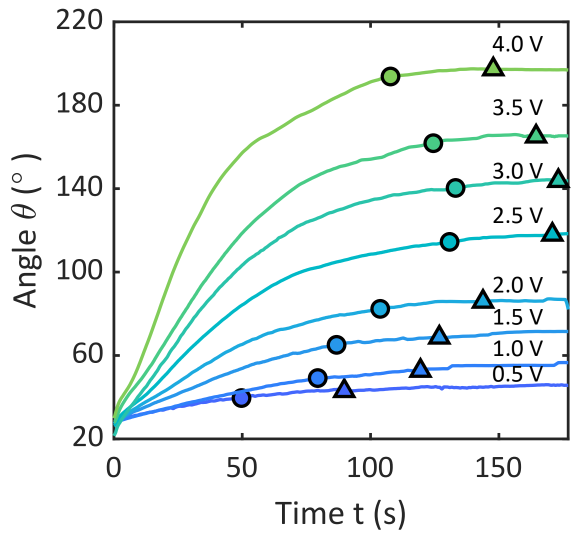


**Figure 6.8:** The steady-state bending angle corresponding to different constant voltages.

triangles represent the angle after 20 s, which is 3º more than the circles. The circle also represents the point where the stiffening process is safe to start for this controlling method.

### 6.2.2 Closed-loop Control

Usually, a closed-loop control could be realized using external contact and contactless sensors, such as a strain sensor or a camera. However, free of external sensors, the morphing can also be accurately controlled by leveraging the TCAs' self-sensing capability, which uses its resistance change during the actuation to reflect the displacement of the TCA thus the bending angle of the module. The resistance of the module is measured during the morphing process under a constant 10 V and fitted with a third-order polynomial (Fig. 6.9)(A). With this monotonic relationship, a PI controller can be implemented to control the module to arrive the desired angle within 3 s and hold the angle steadily for the stiffening process of the spine (Fig. 6.9(B)). Compared with the open-loop method, the morphing process using the closed-loop control method based on self-sensing is more than 100 times faster.

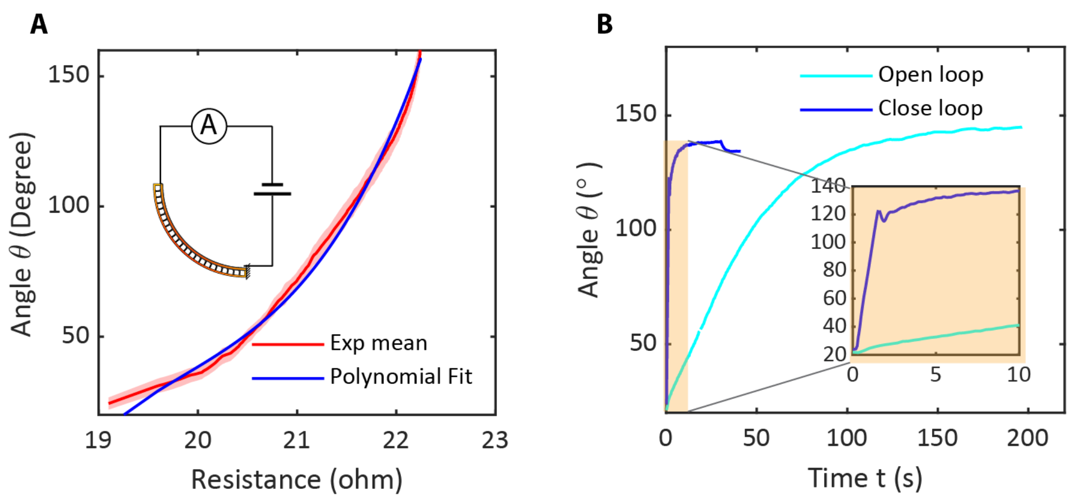


**Figure 6.9:** (A) Then measured resistance and fitted polynomial. (B) The comparison between a closed loop control and open loop control.

## 6.3 Demonstration: Adaptive Gripper and Tetrapod Robot

We propose three shape morphing robots under this concept: an adaptive shape morphing gripper, and a multimodal terrestrial robot. The adaptive gripper has a shape morphing module as the rigid base for two soft fingers. The opening of the shape morphing module will allow the gripper to adapt to the size of the object. The multimodal terrestrial robot has a body that is made by the shape morphing modules, and four continuum legs driven by TCAs are connected to the body. First, when the body is flat, the robot can move using a crawling gait. Second, when the body curves to 90 °, the robot can use an ambling gait to walk. Third, when the robot curves to almost 0 ° (a U shape), the robot can shimmy on a bridge

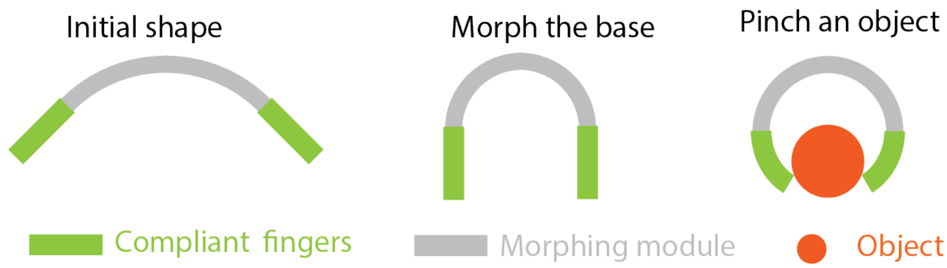


**Figure 6.10:** The schematic of the pitching gripper. The base of the gripper morphs to different angles to allow the finger to reach the objects of different widths. Finally the compliant finger can bend to pinch the object.

### 6.3.1 Adaptive Gripper

Morphing materials that can reconfigure shapes and support load without continuous energy input can enable highly adaptable. To demonstrate the enabling characteristic, the bending morphing modules were used as a reconfigurable base to create a multifunctional, adaptive gripper. Fig. 6.10 shows the grippers with the morphing module as a rigid base during grasping. The gripper is fabricated by connecting two compliant fingers to the two ends of a bending module and anchoring the middle of the module to a rigid rod. The compliant fingers are driven by sheathed TCAs and can quickly bend and relax as demanded. The assembling of the compliant finger to the shape morphing module is shown in Fig. 6.11

To grasp an object, the gripper's base is controlled to move and hold a size using the closed-loop control that allows the fingers to reach and apply force on the object. We demonstrate that the morphable base allows the gripper to adapt to objects' sizes realizing successful grasping that is impossible without modifying the design (Fig. 6.12).

### 6.3.2 Adaptive Tetrapod Robot

We demonstrate the ability of the morphing modules to facilitate different locomotion modes of a tetrapod robot. The body of the robot consists of three parallel shape morphing modules (Fig.6.13A) connected using a 3D printed frame. There are four legs connected to the body, and each leg of the four legs embodies a continuum shape that consists of one carbon fiber rod and several rigid plates. Three TCAs run through the holes in the plates and each TCA is controlled

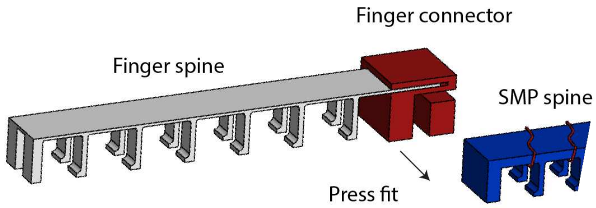


**Figure 6.11:** The rigid finger for the variable-stiffness gripper. It can be snap into the ends of the shape morphing module.

**Figure 6.12:** The objects that the adaptive gripper can pinch by morphing the base, i.e., a sponge, a Coke can, a pingpong ball, and a glove.

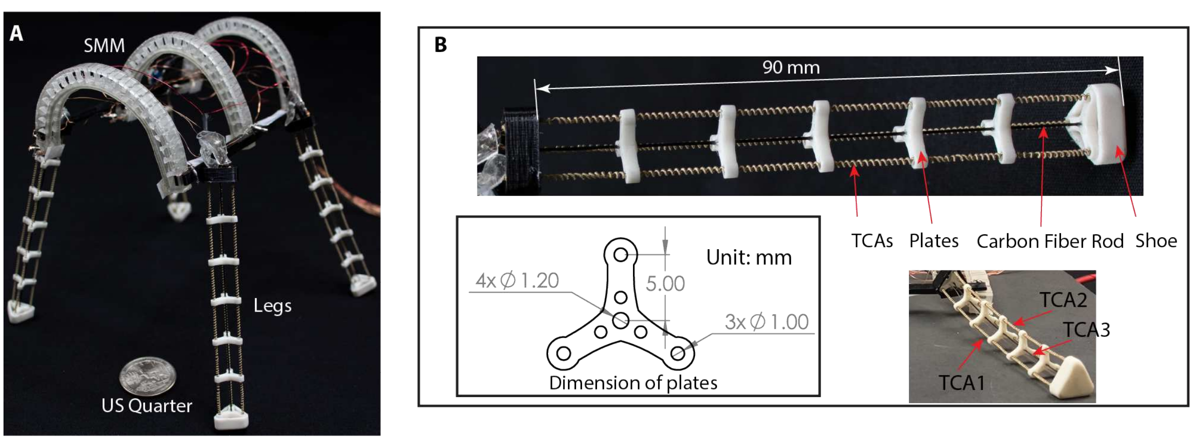


**Figure 6.13:** (A). The adaptive tetrapod robot has two main parts: three parallel 2D bending SMM and four continuum legs. A US quarter is placed on the ground to indicate the robot's size. (B). The assembly of the continuum leg driven by the TCAs. It has three TCAs running through the holes in the plates. The dimensions of the plates are shown in the inset.

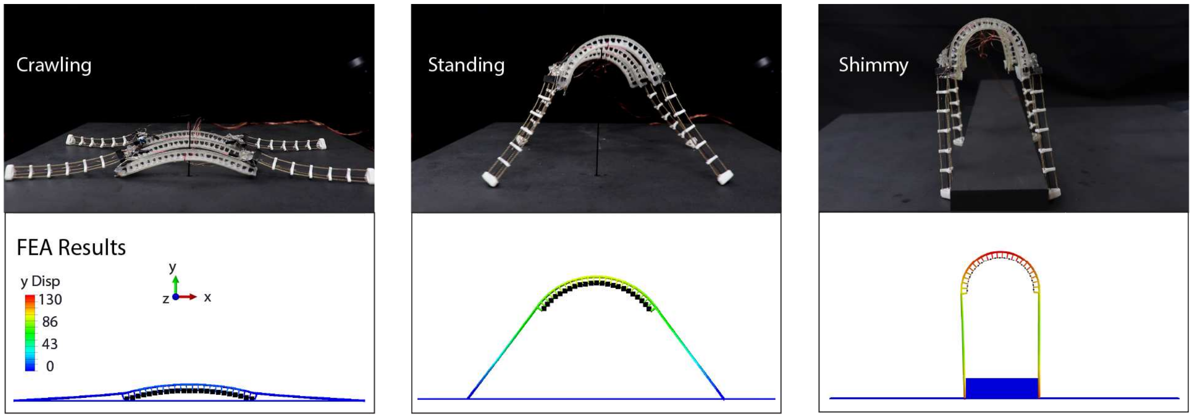


**Figure 6.14:** The front view of the three distinct shapes respectively correspond to crawling, walking, and shimmy. The corresponding shapes are also simulated using FEA.

independently to realize 3D bending (Fig. 6.13B). We actuate the robot by powering the TCAs in specific sequences to realize a looping trajectory for each foot. The robot body initially is almost flat, and it can bend to different angles to facilitate crawling, walking, and climbing motions. These shapes can also be simulated using FEA, though the gravitational force of the body and friction force from the ground are considered.

We demonstrate the adaptivity of the robot by running it through a complicated environment using crawling, walking, and shimming in Fig. 6.14. As shown in Fig. 6.15, at the flat configuration (height of the robot is 2.5 cm), the robot is able to propel itself using a sea turtle-like motion to crawl under a glass plate elevated 3 cm above the ground. During the motion, the four legs are synchronously actuated to generate a loop for the foot to lift the body and transport itself forward (Fig. S4-4 shows the actuation sequence of the three TCAs for the gait). We drove the robot at 2.4 mm/s ( 0.016 body lengths/s)

After passing the glass, the robot stands up to move faster. During the process, the robot body morphs to an angle of 90° and after that, the robot is able to walk using an ambling gait at 9 mm/s ( 0.06 body lengths/s 5%). The morphing of the body improves its speed by 5 times.

When the robot comes to a narrow bridge that connects two desks, it can also bend more to clamp a beam with four legs to realize a shimmy gait. The morphing process starts from the walking configuration and eventually holds a U shape, though it flattens during the heating process.

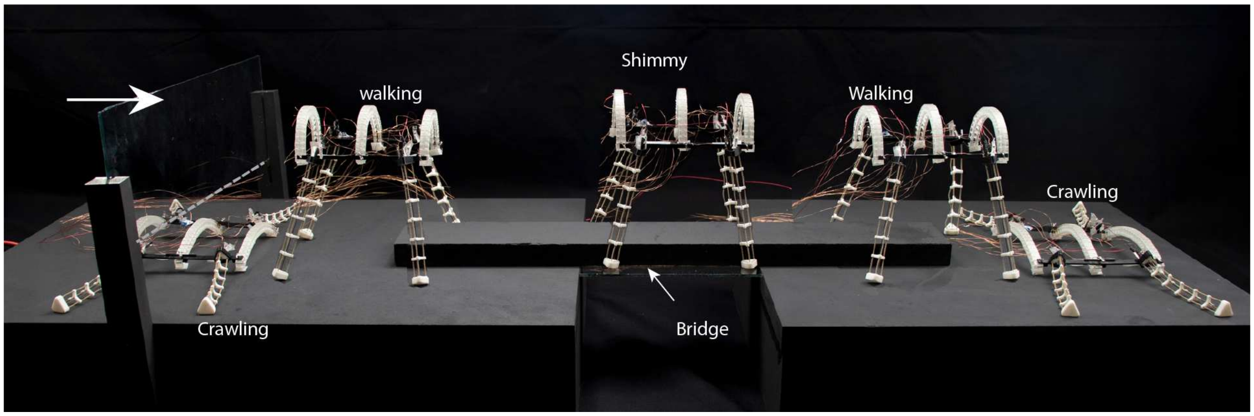


**Figure 6.15:** The robot crawls under a glass, walks to a bridge, shimmy through the bridge, walks to a target point before, and finally recovers its original shape.

After the morphing, the robot is only 1/3 of its original width. The front or rear two legs alternatively clamp the beam to move the robot forward using friction force like a caterpillar. The robot is able to climb along the beam at 0.75 mm/s ( 0.005 body lengths/s). After it walks off the bridge, it can morph to the walking configuration to allow fast moving, and then recovers to a flat shape once it arrives at the target position on the second desk.

## 6.4 Chapter Summary

In the chapter, we demonstrate that the ability to morph shapes is critical for packing multi-functions into next-generation, small-scale robots. In lieu of traditional approaches that rely on thermally activated variable stiffness materials and state-of-the-art high-energy-density artificial muscle, here, we introduce versatile and controllable shape-morphing modules. Shape-morphing modules combine the desirable features of the existing stiffness modulation techniques and artificial muscles. The shape-morphing modules do not require bulky external components such as fluid/pneumatic pumps, magnetic field generators, high-voltage generators, and uniform heating chambers. As examples, the adaptive grippers and adaptive morphing tetrapod are demonstrated.

# Chapter 7

# Conclusion and Future Work

## 7.1 Conclusion

TCAs have recently emerged as a promising artificial muscle, exhibiting several unique advantages compared with other muscles, such as low-cost, easy-to-fabricate, low actuation voltage, and large work density. Due to TCAs' merits, they have been recently used in many robots/devices/systems. In this dissertation, the design, modeling, and control of TCA and TCA-driven soft robots are well studied.

To better actuate soft robots with TCAs, we introduce a novel technique to fabricate TCAs that will have can contract larger than 48% without a preload, termed free stroke. The TCA overcomes the weakness of the previous TCAs, and thus can recover to initial lengths without external load. By characterizing the relationship between the resistance and the actuation displacement of a TCA, the displacement of a TCA is controlled using the resistance as a feedback signal.

The modeling of TCAs lags far behind the various implementations. Because TCA actuation represents a complicated thermal-mechanical system, involving many parameters such as the geometry (e.g., diameter, pitch angle), and the material property (e.g., thermal expansion, Young's modulus). Existing models generally simplify the problem by treating the actuator as a uniform spring, limiting its usage to specific types of TCAs. The model developed by us represents the first comprehensive physics-based model for TCAs. It leverages Cosserat rod theory to accurately model the strains of the twisted fiber in a TCA. Such a model is geometrically exact because no approximation of small deflection is assumed. It can also include nonlinearity of material such as temperature and strain dependency. Remarkably, the developed models are so general that existing models for TCAs can be considered special cases

We demonstrate soft robots with programmable motions by placing TCAs in different shapes inside a soft body. By placing TCAs in different shapes, we demonstrate a completely soft robotic arm that mimics a human forearm. Since the TCA can also be directly used as a sensor therefore the robotic arm can also sense the external load and be controlled precisely. We developed a physics-based model based on TCAs' physical that is a general model for different types of TCAs. A simulation model is also developed to simulate the TCA-driven soft robots. The presented modeling and simulation approach will facilitate the design, optimization, and control of soft robots driven by TCAs or other types of artificial muscles.

Finally, we demonstrate a bending shape-morphing module that can move to a specific angle and lock into the shape. With the TCAs, we can achieve embedded actuation and control with a compact design. Characterization of the model is conducted and robots (morphing grippers, morphing tetrapods) driven by TCAs are built. We demonstrate that the robots can change their shape for facilitating themselves to accomplish different tasks.

## 7.2 Future Work

For future work, we will focus on the following three directions:

First, we can continue research on the dynamics modeling of soft robots to realize real-time simulation. Physics-based modeling of soft robots, especially those driven by artificial muscles, is time-consuming; the learning-based method is fast but requires large training data sets. How to combine both methods (or even online learning) to realize fast simulation is challenging and underexplored. To address this challenge, I will generate training data through the high-fidelity physics-based model and then use the data to develop data-driven models (e.g., deep neural networks or Koopman operator). The fast simulation will pave the way for the optimization and control of soft robots.

Second, we can further study the control of the TCAs based on self-sensing technology. So far the position control is only limited to the constant-weight case, we can extend the control to a varying load case by modeling. Also, the force and thus the stiffness of the TCA can be controlled to realize necessary compliance when the TCAs are implemented in wearable prosthetic devices. The hysteresis also can be compensated using algorithms to achieve more precise control.

Third, there are more possibilities for the shape morphing concept. More complicated demonstrations can be realized through the combinations of the bending shape morphing module, e.g., a grid surface. In the dissertation, we only implemented the bending shape morphing module, but there are more deformations, for example, we can extend the type of motions to 3D bending and twisting. The concept can also be implemented on origami or continuous surface to realize more interesting applications.

We envision that the upgraded TCAs can endow a variety of robots, soft or rigid, with large, programmable, and controllable motion in the future.

# Bibliography


[1] Carter S Haines, Márcio D Lima, Na Li, Geoffrey M Spinks, Javad Foroughi, John DW Madden, Shi Hyeong Kim, Shaoli Fang, Mônica Jung de Andrade, Fatma Göktepe, et al. Artificial muscles from fishing line and sewing thread. *science*, 343(6173):868–872, 2014.

[2] Seyed M Mirvakili, Ali Rafie Ravandi, Ian W Hunter, Carter S Haines, Na Li, Javad Foroughi, Sina Naficy, Geoffrey M Spinks, Ray H Baughman, and John DW Madden. Simple and strong: Twisted silver painted nylon artificial muscle actuated by joule heating. In *Electroactive Polymer Actuators and Devices (EAPAD) 2014*, volume 9056, page 90560I. International Society for Optics and Photonics, 2014.

[3] Carter S Haines, Na Li, Geoffrey M Spinks, Ali E Aliev, Jiangtao Di, and Ray H Baughman. New twist on artificial muscles. *Proceedings of the National Academy of Sciences*, 113(42):11709–11716, 2016.

[4] Michael C Yip and Günter Niemeyer. On the control and properties of supercoiled polymer artificial muscles. *IEEE Transactions on Robotics*, 33(3):689–699, 2017.

[5] Kyeong Ho Cho, Ho Sang Jung, Sang Yul Yang, Youngeun Kim, Hugo Rodrigue, Hyungpil Moon, Ja Choon Koo, and Hyouk Ryeol Choi. Sliding filament joint mechanism: biomimetic artificial joint mechanism for artificial skeletal muscles. *Journal of Mechanisms and Robotics*, 11(2), 2019.

[6] Lianjun Wu, Indrajeet Chauhan, and Yonas Tadesse. A novel soft actuator for the musculoskeletal system. *Advanced Materials Technologies*, 3(5):1700359, 2018.

[7] Yara Almubarak and Yonas Tadesse. Twisted and coiled polymer (tcp) muscles embedded in silicone elastomer for use in soft robot. *International Journal of Intelligent Robotics and Applications*, 1(3):352–368, 2017.

[8] Yang Yang, Yu Alexander Tse, Yazhan Zhang, Zicheng Kan, and Michael Yu Wang. A low-cost inchworm-inspired soft robot driven by supercoiled polymer artificial muscle. In *2019 2nd IEEE International Conference on Soft Robotics (RoboSoft)*, pages 161–166. IEEE, 2019.

[9] Caterina Lamuta, Honglu He, Kaihao Zhang, Michael Rogalski, Nancy Sottos, and Sameh Tawfick. Digital texture voxels for stretchable morphing skin applications. *Advanced Materials Technologies*, 4(8):1900260, 2019.

[10] Armita Hamidi, Yara Almubarak, Yash Mahendra Rupawat, Jeremy Warren, and Yonas Tadesse. Poly-saora robotic jellyfish: swimming underwater by twisted and coiled polymer actuators. *Smart Materials and Structures*, 29(4):045039, 2020.

[11] Daniela Rus and Michael T Tolley. Design, fabrication and control of soft robots. *Nature*, 521(7553):467, 2015.

[12] Robert F Shepherd, Filip Ilievski, Wonjae Choi, Stephen A Morin, Adam A Stokes, Aaron D Mazzeo, Xin Chen, Michael Wang, and George M Whitesides. Multigait soft robot. *Proceedings of the national academy of sciences*, 108(51):20400–20403, 2011.

[13] Marcello Calisti, Michele Giorelli, Guy Levy, Barbara Mazzolai, B Hochner, Cecilia Laschi, and Paolo Dario. An octopus-bioinspired solution to movement and manipulation for soft robots. *Bioinspiration & biomimetics*, 6(3):036002, 2011.

[14] Nicholas W Bartlett, Michael T Tolley, Johannes TB Overvelde, James C Weaver, Bobak Mosadegh, Katia Bertoldi, George M Whitesides, and Robert J Wood. A 3d-printed, functionally graded soft robot powered by combustion. *Science*, 349(6244):161–165, 2015.

[15] Guo-Ying Gu, Jian Zhu, Li-Min Zhu, and Xiangyang Zhu. A survey on dielectric elastomer actuators for soft robots. *Bioinspiration & biomimetics*, 12(1):011003, 2017.

[16] E Acome, SK Mitchell, TG Morrissey, MB Emmett, C Benjamin, M King, M Radakovitz, and C Keplinger. Hydraulically amplified self-healing electrostatic actuators with muscle-like performance. *Science*, 359(6371):61–65, 2018.

[17] Michael Wehner, Ryan L Truby, Daniel J Fitzgerald, Bobak Mosadegh, George M Whitesides, Jennifer A Lewis, and Robert J Wood. An integrated design and fabrication strategy for entirely soft, autonomous robots. *Nature*, 536(7617):451, 2016.

[18] Aslan Miriyev, Kenneth Stack, and Hod Lipson. Soft material for soft actuators. *Nature communications*, 8(1):596, 2017.

[19] Chengjun Wang, Kyoseung Sim, Jin Chen, Hojin Kim, Zhoulyu Rao, Yuhang Li, Weiqiu Chen, Jizhou Song, Rafael Verduzco, and Cunjiang Yu. Soft ultrathin electronics innervated adaptive fully soft robots. *Advanced Materials*, 30(13):1706695, 2018.

[20] Wei Wang and Sung-Hoon Ahn. Shape memory alloy-based soft gripper with variable stiffness for compliant and effective grasping. *Soft robotics*, 4(4):379–389, 2017.

[21] Xiaonan Huang, Kitty Kumar, Mohammad K Jawed, Amir M Nasab, Zisheng Ye, Wanliang Shan, and Carmel Majidi. Chasing biomimetic locomotion speeds: Creating untethered soft robots with shape memory alloy actuators. *Science Robotics*, 3(25):eaau7557, 2018.

[22] Sameh Tawfick and Yichao Tang. Stronger artificial muscles, with a twist. *Science*, 365(6449):125–126, 2019.

[23] A. Abbas and J. Zhao. Twisted and coiled sensor for shape estimation of soft robots. In *2017 IEEE/RSJ International Conference on Intelligent Robots and Systems (IROS)*, pages 482–487, Sept 2017.

[24] Joost van der Weijde, Heike Vallery, and Robert Babuška. Closed-loop control through self-sensing of a joule-heated twisted and coiled polymer muscle. *Soft robotics*, 6(5):621–630, 2019.

[25] Steven I Rich, Robert J Wood, and Carmel Majidi. Untethered soft robotics. *Nature Electronics*, 1(2):102, 2018.

[26] Xiaonan Huang, Kitty Kumar, Mohammad Khalid Jawed, Zisheng Ye, and Carmel Majidi. Soft electrically actuated quadruped (seaq)—integrating a flex circuit board and elastomeric limbs for versatile mobility. *IEEE Robotics and Automation Letters*, 4(3):2415–2422, 2019.

[27] Benjamin Pawlowski, Jiefeng Sun, Jing Xu, Yingxiang Liu, and Jianguo Zhao. Modeling of soft robots actuated by twisted-and-coiled actuators. *IEEE/ASME Transactions on Mechatronics*, 24(1):5–15, 2018.

[28] J. Sun, B. Pawlowski, and J. Zhao. Embedded and controllable shape morphing with twisted-and-coiled actuators. In *2018 IEEE/RSJ International Conference on Intelligent Robots and Systems (IROS)*, pages 5912–5917, Oct 2018.

[29] Qianxi Yang and Guoqiang Li. A top-down multi-scale modeling for actuation response of polymeric artificial muscles. *Journal of the Mechanics and Physics of Solids*, 92:237–259, 2016.

[30] Kyeong Ho Cho, Min-Geun Song, Hosang Jung, Sang Yul Yang, Hyungpil Moon, Ja Choon Koo, Hyouk Ryeol Choi, et al. Fabrication and modeling of temperature-controllable artificial muscle actuator. In *2016 6th IEEE International Conference on Biomedical Robotics and Biomechatronics (BioRob)*, pages 94–98. IEEE, 2016.

[31] Chihaya Oiwa, Ken Masuya, Kenji Tahara, Toshihira Irisawa, Masatoshi Shioya, Takuma Yamauchi, Eitaro Tanaka, Kinji Asaka, and Kentaro Takagi. Gray-box modeling and control of torsional fishing-line artificial muscle actuators. In *Electroactive Polymer Actuators and Devices (EAPAD) XX*, volume 10594, page 1059428. International Society for Optics and Photonics, 2018.

[32] Tuan Luong, Kihyeon Kim, Sungwon Seo, Jae Hyeong Park, Youngeun Kim, Sang Yul Yang, Kyeong Ho Cho, Ja Choon Koo, Hyouk Ryeol Choi, and Hyungpil Moon. Modeling

and position control of a high performance twisted-coiled polymer actuator. In *2018 15th International Conference on Ubiquitous Robots (UR)*, pages 73–79. IEEE, 2018.

[33] Ken Masuya, Shu Ono, Kentaro Takagi, and Kenji Tahara. Modeling framework for macroscopic dynamics of twisted and coiled polymer actuator driven by joule heating focusing on energy and convective heat transfer. *Sensors and Actuators A: Physical*, 267:443–454, 2017.

[34] Ali Abbas and Jianguo Zhao. A physics based model for twisted and coiled actuator. In *Robotics and Automation (ICRA), 2017 IEEE International Conference on*, pages 6121–6126. IEEE, 2017.

[35] C Lamuta, S Messelot, and S Tawfick. Theory of the tensile actuation of fiber reinforced coiled muscles. *Smart Materials and Structures*, 27(5):055018, 2018.

[36] Chunbing Wu and Wen Zheng. A modeling of twisted and coiled polymer artificial muscles based on elastic rod theory. In *Actuators*, volume 9, page 25. Multidisciplinary Digital Publishing Institute, 2020.

[37] Farzad Karami, Lianjun Wu, and Yonas Tadesse. Modeling of one-ply and two-ply twisted and coiled polymer (tcp) artificial muscles. *IEEE/ASME Transactions on Mechatronics*, pages 300–310, 2020.

[38] Parth Kotak, Thilina Weerakkody, and Caterina Lamuta. Physics-based dynamic model for the electro-thermal actuation of bio-inspired twisted spiral artificial muscles (tsams). *Polymer*, 222:123642, 2021.

[39] Ken Masuya, Shu Ono, Kentaro Takagi, and Kenji Tahara. Nonlinear dynamics of twisted and coiled polymer actuator made of conductive nylon based on the energy balance. In *2017 IEEE International Conference on Advanced Intelligent Mechatronics (AIM)*, pages 779–784. IEEE, 2017.

[40] Farzad Karami and Yonas Tadesse. Modeling of twisted and coiled polymer (tcp) muscle based on phenomenological approach. *Smart Materials and Structures*, 26(12):125010, 2017.

[41] Shazed Aziz and Geoffrey M Spinks. Torsional artificial muscles. *Materials Horizons*, 7(3):667–693, 2020.

[42] Augustus Edward Hough Love. *A treatise on the mathematical theory of elasticity*. Cambridge university press, 1944.

[43] Valentina Giovinco, Parth Kotak, Venanzio Cichella, Carmine Maletta, and Caterina Lamuta. Dynamic model for the tensile actuation of thermally and electro-thermally actuated twisted and coiled artificial muscles (tcams). *Smart Materials and Structures*, 29(2):025004, 2019.

[44] Arthur Munzenmaier Wahl. *Mechanical springs*. Penton Publishing Company, 1944.

[45] III Robert J. Webster and Bryan A. Jones. Design and kinematic modeling of constant curvature continuum robots: A review. *The International Journal of Robotics Research*, 29(13):1661–1683, 2010.

[46] Girish Krishnan, Joshua Bishop-Moser, Charles Kim, and Sridhar Kota. Kinematics of a generalized class of pneumatic artificial muscles. *ASME Journal of Mechanisms and Robotics*, 7(4):041014, 2015.

[47] Joshua Bishop-Moser and Sridhar Kota. Design and modeling of generalized fiber-reinforced pneumatic soft actuators. *IEEE Transactions on Robotics*, 31(3):536–545, 2015.

[48] Andrew D Marchese, Russ Tedrake, and Daniela Rus. Dynamics and trajectory optimization for a soft spatial fluidic elastomer manipulator. *The International Journal of Robotics Research*, 35(8):1000–1019, 2016.

[49] Panagiotis Polygerinos, Zheng Wang, Johannes TB Overvelde, Kevin C Galloway, Robert J Wood, Katia Bertoldi, and Conor J Walsh. Modeling of soft fiber-reinforced bending actuators. *IEEE Transactions on Robotics*, 31(3):778–789, 2015.

[50] Isuru S Godage, Gustavo A Medrano-Cerda, David T Branson, Emanuele Guglielmino, and Darwin G Caldwell. Dynamics for variable length multisection continuum arms. *The International Journal of Robotics Research*, 35(6):695–722, 2016.

[51] William S Rone and Pinhas Ben-Tzvi. Continuum robot dynamics utilizing the principle of virtual power. *IEEE Transactions on Robotics*, 30(1):275–287, 2014.

[52] Philip Moseley, Juan Manuel Florez, Harshal Arun Sonar, Gunjan Agarwal, William Curtin, and Jamie Paik. Modeling, design, and development of soft pneumatic actuators with finite element method. *Advanced engineering materials*, 18(6):978–988, 2016.

[53] Maria Pozzi, Eder Miguel, Raphael Deimel, Monica Malvezzi, Bernd Bickel, Oliver Brock, and Domenico Prattichizzo. Efficient fem-based simulation of soft robots modeled as kinematic chains. In *2018 IEEE International Conference on Robotics and Automation (ICRA)*, pages 4206–4213. IEEE, 2018.

[54] Olivier Goury and Christian Duriez. Fast, generic, and reliable control and simulation of soft robots using model order reduction. *IEEE Transactions on Robotics*, 34(6):1565–1576, 2018.

[55] Thor Morales Bieze, Frederick Largilliere, Alexandre Kruszewski, Zhongkai Zhang, Rochdi Merzouki, and Christian Duriez. Finite element method-based kinematics and closed-loop control of soft, continuum manipulators. *Soft robotics*, 5(3):348–364, 2018.

[56] Yoel Shapiro, Kosa Gabor, and Alon Wolf. Modeling a hyperflexible planar bending actuator as an inextensible euler–bernoulli beam for use in flexible robots. *Soft Robotics*, 2(2):71–79, 2015.

[57] SM Hadi Sadati, Ali Shiva, Ludovic Renson, Caleb Rucker, Kaspar Althoefer, Thrisantha Nanayakkara, Christos Bergeles, Helmut Hauser, and Ian D Walker. Reduced order vs. discretized lumped system models with absolute and relative states for continuum manipulators. *Robotics: Science and Systems, Freiburg, Germany*, page 10, 2019.

[58] Nathaniel N Goldberg, Xiaonan Huang, Carmel Majidi, Alyssa Novelia, Oliver M O'Reilly, Derek A Paley, and William L Scott. On planar discrete elastic rod models for the locomotion of soft robots. *Soft robotics*, 2019.

[59] Oliver M O'Reilly. *Modeling Nonlinear Problems in the Mechanics of Strings and Rods*. Springer, 2017.

[60] SS Antman. *Nonlinear Problems of Elasticity, volume 107 of Applied Mathematical Sciences, 2nd edn*. Springer, 2005.

[61] D Caleb Rucker and Robert J Webster III. Statics and dynamics of continuum robots with general tendon routing and external loading. *IEEE Transactions on Robotics*, 27(6):1033–1044, 2011.

[62] Federico Renda, Frédéric Boyer, Jorge Dias, and Lakmal Seneviratne. Discrete cosserat approach for multisection soft manipulator dynamics. *IEEE Transactions on Robotics*, 34(6):1518–1533, 2018.

[63] John Till, Vincent Aloi, and Caleb Rucker. Real-time dynamics of soft and continuum robots based on cosserat rod models. *The International Journal of Robotics Research*, 38(6):723–746, 2019.

[64] Seyed M Mirvakili and Ian W Hunter. Artificial muscles: Mechanisms, applications, and challenges. *Advanced Materials*, 30(6):1704407, 2018.

[65] Emmanuel Siéfert, Etienne Reyssat, José Bico, and Benoît Roman. Bio-inspired pneumatic shape-morphing elastomers. *Nature materials*, 18(1):24, 2019.

[66] Arda Kotikian, Ryan L Truby, John William Boley, Timothy J White, and Jennifer A Lewis. 3d printing of liquid crystal elastomeric actuators with spatially programed nematic order. *Advanced Materials*, 30(10):1706164, 2018.

[67] Hillel Aharoni, Yu Xia, Xinyue Zhang, Randall D Kamien, and Shu Yang. Universal inverse design of surfaces with thin nematic elastomer sheets. *Proceedings of the National Academy of Sciences*, 115(28):7206–7211, 2018.

[68] Weicheng Huang, Xiaonan Huang, Carmel Majidi, and M Khalid Jawed. Dynamic simulation of articulated soft robots. *Nature communications*, 11(1):1–9, 2020.

[69] Xiaotian Zhang, Fan Kiat Chan, Tejaswin Parthasarathy, and Mattia Gazzola. Modeling and simulation of complex dynamic musculoskeletal architectures. *Nature communications*, 10(1):1–12, 2019.

[70] Te Li, Yongqing Wang, Kuo Liu, Haibo Liu, Jiali Zhang, Xianjun Sheng, and Dongming Guo. Thermal actuation performance modification of coiled artificial muscle by controlling annealing stress. *Journal of Polymer Science Part B: Polymer Physics*, 56(5):383–390, 2018.

[71] Kyeong Ho Cho, Min Geun Song, Hosang Jung, Jungwoo Park, Hyungpil Moon, Ja Choon Koo, Jae-Do Nam, and Hyouk Ryeol Choi. A robotic finger driven by twisted and coiled polymer actuator. In *Electroactive Polymer Actuators and Devices (EAPAD) 2016*, volume 9798, page 97981J. International Society for Optics and Photonics, 2016.

[72] Kihyeon Kim, Kyeong Ho Cho, Ho Sang Jung, Sang Yul Yang, Youngeun Kim, Jae Hyeong Park, Hoyoung Jang, Jae-Do Nam, Ja Choon Koo, Hyungpil Moon, et al. Double helix twisted and coiled soft actuator from spandex and nylon. *Advanced Engineering Materials*, 20(11):1800536, 2018.

[73] Sang Yul Yang, Kyeong Ho Cho, Youngeun Kim, Min-Geun Song, Ho Sang Jung, Ji Wang Yoo, Hyungpil Moon, Ja Choon Koo, Hyouk Ryeol Choi, et al. High performance twisted

and coiled soft actuator with spandex fiber for artificial muscles. *Smart Materials and Structures*, 26(10):105025, 2017.

[74] Soheil Kianzad, Milind Pandit, Addie Bahi, Ali Rafiee, Frank Ko, Geoffrey M Spinks, and John DW Madden. Nylon coil actuator operating temperature range and stiffness. In *Electroactive Polymer Actuators and Devices (EAPAD) 2015*, volume 9430, page 94301X. International Society for Optics and Photonics, 2015.

[75] Xintian Tang, Kai Li, Yingxiang Liu, Dong Zhou, and Jianguo Zhao. A soft crawling robot driven by single twisted and coiled actuator. *Sensors and Actuators A: Physical*, 291:80–86, 2019.

[76] Huai-Ti Lin, Gary G Leisk, and Barry Trimmer. Goqbot: a caterpillar-inspired soft-bodied rolling robot. *Bioinspiration & biomimetics*, 6(2):026007, 2011.

[77] M Musso, Andreas Reyer, and D Bertoldo Menezes. Analysis of the brill transition and reversible brill transition in nylon 6, 6 by raman spectroscopy. *Spectroscopy*, 31(7):44–48, 2016.

[78] Ali Rafie Ravandi. *Characterizing the behavior of nylon actuators and exploring methods for manufacturing them to get the highest amount of output*. PhD thesis, University of British Columbia, 2018.

[79] Antonello Cherubini, Giacomo Moretti, Rocco Vertechy, and Marco Fontana. Experimental characterization of thermally-activated artificial muscles based on coiled nylon fishing lines. *Aip Advances*, 5(6):067158, 2015.

[80] Yi-Wei Huang, Wen-Shin Lee, Yu-Fan Chuang, Wenxin Cao, Fuqian Yang, and Sanboh Lee. Time-dependent deformation of artificial muscles based on nylon 6. *Materials Science and Engineering: C*, 98:445–451, 2019.

[81] Jun Zhang, Anthony Simeonov, and Michael C Yip. Three-dimensional hysteresis compensation enhances accuracy of robotic artificial muscles. *Smart Materials and Structures*, 27(3):035002, 2018.

[82] Revanth Konda and Jun Zhang. The effects of nylon polymer threads on strain-loading hysteresis behavior of supercoiled polymer (scp) artificial muscles. In *Dynamic Systems and Control Conference*, volume 59162, page V003T20A008. American Society of Mechanical Engineers, 2019.

[83] Joost van der Weijde, Bram Smit, Michael Fritschi, Cornelis van de Kamp, and Heike Vallery. Self-sensing of deflection, force, and temperature for joule-heated twisted and coiled polymer muscles via electrical impedance. *IEEE/ASME Transactions on Mechatronics*, 22(3):1268–1275, 2016.

[84] Lianjun Wu and Yonas Tadesse. Modeling of the electrical resistance of tcp muscle. In *ASME 2017 International Mechanical Engineering Congress and Exposition*, pages V04AT05A024–V04AT05A024. American Society of Mechanical Engineers, 2017.

[85] Anthony Simeonov, Taylor Henderson, Zixuan Lan, Guhan Sundar, Adam Factor, Jun Zhang, and Michael Yip. Bundled super-coiled polymer artificial muscles: Design, characterization, and modeling. *IEEE Robotics and Automation Letters*, 3(3):1671–1678, 2018.

[86] Jiefeng Sun, Brandon Tighe, Yingxiang Liu, and Jianguo Zhao. Twisted-and-coiled actuators with free strokes enable soft robots with programmable motions. *Soft robotics*, 8(2):213–225, 2021.

[87] Jiefeng Sun, Ben Pawlowski, and Jianguo Zhao. Soft manipulators with programmable motion using twisted-and-coiled actuators (conference presentation). In *Electroactive Polymer Actuators and Devices (EAPAD) XXI*, volume 10966, page 109660Q. International Society for Optics and Photonics, 2019.

[88] Jiefeng Sun and Jianguo Zhao. Integrated actuation and self-sensing for twisted-and-coiled actuators with applications to innervated soft robots. In *2020 IEEE International Conference on Robotics and Automation (ICRA)*, pages 5912–5917, 2018.

[89] CL Choy, WP Leung, and EL Ong. Thermal expansivity of oriented nylon-6 and nylon-6, 6. *Polymer*, 26(6):884–888, 1985.

[90] Shazed Aziz, Sina Naficy, Javad Foroughi, Hugh R Brown, and Geoffrey M Spinks. Controlled and scalable torsional actuation of twisted nylon 6 fiber. *Journal of Polymer Science Part B: Polymer Physics*, 54(13):1278–1286, 2016.

[91] Federico Renda, Michele Giorelli, Marcello Calisti, Matteo Cianchetti, and Cecilia Laschi. Dynamic model of a multibending soft robot arm driven by cables. *IEEE Transactions on Robotics*, 30(5):1109–1122, 2014.

[92] Ning Pan and David Brookstein. Physical properties of twisted structures. ii. industrial yarns, cords, and ropes. *Journal of applied polymer science*, 83(3):610–630, 2002.

[93] A Demšar, V Bukošek, and A Kljun. Dynamic mechanical analysis of nylon 66 cord yarns. *Fibres & Textiles in Eastern Europe*, Nr 4 (81):29–34, 2010.

[94] Caleb Rucker. Integrating rotations using nonunit quaternions. *IEEE Robotics and Automation Letters*, 3(4):2979–2986, 2018.

[95] Itzhack Y Bar-Itzhack. New method for extracting the quaternion from a rotation matrix. *Journal of guidance, control, and dynamics*, 23(6):1085–1087, 2000.

[96] Jacek Kierzenka and Lawrence F Shampine. A bvp solver that controls residual and error. *JNAIAM J. Numer. Anal. Ind. Appl. Math*, 3(1-2):27–41, 2008.

[97] Harvard Lomax, Thomas H Pulliam, and David W Zingg. *Fundamentals of computational fluid dynamics*. Springer Science & Business Media, 2013.

[98] Piaras Kelly. Solid mechanics part i: An introduction to solid mechanics. *A Creative Commons Attributions, Mountain View, CA*, 94042, 2013.

[99] Revanth Konda and Jun Zhang. Experimental investigation of the lonely stroke behavior in supercoiled polymer artificial muscles. In Yoseph Bar-Cohen, editor, *Electroactive Polymer Actuators and Devices (EAPAD) XXII*, volume 11375, pages 133 – 141. International Society for Optics and Photonics, SPIE, 2020.

[100] Diego R Higueras-Ruiz, Michael W Shafer, and Heidi P Feigenbaum. Cavatappi artificial muscles from drawing, twisting, and coiling polymer tubes. *Science Robotics*, 6(53), 2021.

[101] Geoffrey M Spinks, Nicolas D Martino, Sina Naficy, David J Shepherd, and Javad Foroughi. Dual high-stroke and high–work capacity artificial muscles inspired by dna supercoiling. *Science Robotics*, 6(53), 2021.

[102] M Khalid Jawed, Alyssa Novelia, and Oliver M O'Reilly. *A primer on the kinematics of discrete elastic rods*. Springer, 2018.

[103] Miklós Bergou, Max Wardetzky, Stephen Robinson, Basile Audoly, and Eitan Grinspun. Discrete elastic rods. In *ACM SIGGRAPH 2008 papers*, pages 1–12. ACM New York, NY, USA, 2008.

[104] Jun Zhang, Kaushik Iyer, Anthony Simeonov, and Michael C Yip. Modeling and inverse compensation of hysteresis in supercoiled polymer artificial muscles. *IEEE Robotics and Automation Letters*, 2(2):773–780, 2017.

[105] Clive L Dym. Consistent derivations of spring rates for helical springs. *Journal of Mechanical Design*, 131(7), 2009.

[106] Yu She, Chang Li, Jonathon Cleary, and Hai-Jun Su. Design and fabrication of a soft robotic hand with embedded actuators and sensors. *Journal of Mechanisms and Robotics*, 7(2):021007, 2015.

[107] ZH Zhu and SA Meguid. Elastodynamic analysis of low tension cables using a new curved beam element. *International journal of solids and structures*, 43(6):1490–1504, 2006.

[108] Robert J Webster III and Bryan A Jones. Design and kinematic modeling of constant curvature continuum robots: A review. *The International Journal of Robotics Research*, 29(13):1661–1683, 2010.

[109] Xiaonan Huang, Kitty Kumar, Mohammad K Jawed, Amir Mohammadi Nasab, Zisheng Ye, Wanliang Shan, and Carmel Majidi. Highly dynamic shape memory alloy actuator for fast moving soft robots. *Advanced Materials Technologies*, 4(4):1800540, 2019.

[110] Feng Ni, Daniel Rojas, Kai Tang, Lilong Cai, and Tamim Asfour. A jumping robot using soft pneumatic actuator. In *2015 IEEE International Conference on Robotics and Automation (ICRA)*, pages 3154–3159. IEEE, 2015.

[111] Jakob A Faber, Andres F Arrieta, and André R Studart. Bioinspired spring origami. *Science*, 359(6382):1386–1391, 2018.

[112] Stefano Mintchev, Jun Shintake, and Dario Floreano. Bioinspired dual-stiffness origami. *Science Robotics*, 3(20):eaau0275, 2018.

[113] Zirui Zhai, Yong Wang, and Hanqing Jiang. Origami-inspired, on-demand deployable and collapsible mechanical metamaterials with tunable stiffness. *Proceedings of the National Academy of Sciences*, 115(9):2032–2037, 2018.

[114] Sicong Shan, Sung H Kang, Jordan R Raney, Pai Wang, Lichen Fang, Francisco Candido, Jennifer A Lewis, and Katia Bertoldi. Multistable architected materials for trapping elastic strain energy. *Advanced Materials*, 27(29):4296–4301, 2015.

[115] Philipp Rothemund, Alar Ainla, Lee Belding, Daniel J Preston, Sarah Kurihara, Zhigang Suo, and George M Whitesides. A soft, bistable valve for autonomous control of soft actuators. *Science Robotics*, 3(16):eaar7986, 2018.

[116] Haijie Zhang, Jiefeng Sun, and Jianguo Zhao. Compliant bistable gripper for aerial perching and grasping. In *2019 International Conference on Robotics and Automation (ICRA)*, pages 1248–1253. IEEE, 2019.

[117] Tian Chen, Osama R Bilal, Kristina Shea, and Chiara Daraio. Harnessing bistability for directional propulsion of soft, untethered robots. *Proceedings of the National Academy of Sciences*, 115(22):5698–5702, 2018.

[118] Larry L Howell. *Compliant mechanisms*. John Wiley & Sons, 2001.

[119] Benjamin Pawlowski, Jiefeng Sun, Jing Xu, Yingxiang Liu, and Jianguo Zhao. Modeling of soft robots actuated by twisted-and-coiled actuators. *IEEE/ASME Transactions on Mechatronics*, 24(1):5–15, 2019.

[120] Jianguo Zhao, Jing Xu, Bingtuan Gao, Ning Xi, Fernando J Cintron, Matt W Mutka, and Li Xiao. Msu jumper: A single-motor-actuated miniature steerable jumping robot. *IEEE Transactions on Robotics*, 29(3):602–614, 2013.

[121] Ben Pawlowski, Jiefeng Sun, and Jianguo Zhao. Dynamic modeling of soft manipulators actuated by twisted-and-coiled actuators. In *2018 IEEE Conference on Decision and Control (CDC)*, pages 409–414. IEEE, 2018.

[122] Filip Ilievski, Aaron D Mazzeo, Robert F Shepherd, Xin Chen, and George M Whitesides. Soft robotics for chemists. *Angewandte Chemie*, 123(8):1930–1935, 2011.

[123] Jiefeng Sun and Jianguo Zhao. Physics-based modeling of twisted-and-coiled actuators using cosserat rod theory. *IEEE Transactions on Robotics*, 2021.

[124] Stefano Mintchev and Dario Floreano. Adaptive morphology: A design principle for multimodal and multifunctional robots. *IEEE Robotics & Automation Magazine*, 23(3):42–54, 2016.

[125] Aditya A Paranjape, Soon-Jo Chung, and Joseph Kim. Novel dihedral-based control of flapping-wing aircraft with application to perching. *IEEE Transactions on Robotics*, 29(5):1071–1084, 2013.

[126] Yoo-Seok Kim, Gwang-Pil Jung, Haan Kim, Kyu-Jin Cho, and Chong-Nam Chu. Wheel transformer: A wheel-leg hybrid robot with passive transformable wheels. *IEEE Transactions on Robotics*, 30(6):1487–1498, 2014.

[127] Yu She, Carter J Hurd, and Hai-Jun Su. A transformable wheel robot with a passive leg. In *Intelligent Robots and Systems (IROS), 2015 IEEE/RSJ International Conference on*, pages 4165–4170. IEEE, 2015.

[128] Alì Sadeghi, Lucia Beccai, and Barbara Mazzolai. Innovative soft robots based on electrorheological fluids. In *Intelligent Robots and Systems (IROS), 2012 IEEE/RSJ International Conference on*, pages 4237–4242. IEEE, 2012.

[129] Carmel Majidi and Robert J Wood. Tunable elastic stiffness with microconfined magnetorheological domains at low magnetic field. *Applied Physics Letters*, 97(16):164104, 2010.

[130] Michelle C Yuen, R Adam Bilodeau, and Rebecca K Kramer. Active variable stiffness fibers for multifunctional robotic fabrics. *IEEE Robotics and Automation Letters*, 1(2):708–715, 2016.

[131] Michael McEvoy and Nikolaus Correll. Shape change through programmable stiffness. In *Experimental Robotics*, pages 893–907. Springer, 2016.

[132] T. L. Buckner, E. L. White, M. C. Yuen, R. A. Bilodeau, and R. K. Kramer. A move-and-hold pneumatic actuator enabled by self-softening variable stiffness materials. In *2017 IEEE/RSJ International Conference on Intelligent Robots and Systems (IROS)*, pages 3728–3733, Sept 2017.